

HCN $J=4-3$, HNC $J=1-0$, H¹³CN $J=1-0$, and HC₃N $J=10-9$ Maps of Galactic Center Region I: Spatially-Resolved Measurements of Physical Conditions and Chemical Composition

KUNIHICO TANAKA,¹ MAKOTO NAGAI,² KAZUHISA KAMEGAI,³ TAKAHIRO IINO,⁴ AND TAKESHI SAKAI⁵

¹*Department of Physics, Faculty of Science and Technology, Keio University, 3-14-1 Hiyoshi, Yokohama, Kanagawa 223-8522 Japan*

²*Advanced Technology Center, National Astronomical Observatory Japan, 2-21-1 Osawa, Mitaka, Tokyo 181-8588, Japan*

³*Astronomy Data Center, National Astronomical Observatory Japan, 2-21-1 Osawa, Mitaka, Tokyo 181-8588, Japan*

⁴*Nature and Science Museum, Tokyo University of Agriculture and Technology, 2-24-6 Naka-machi, Koganei, Tokyo 184-8588, Japan*

⁵*Graduate School of Informatics and Engineering, The University of Electro-Communications, 1-5-1 Chofugaoka, Chofu, Tokyo 182-8585, Japan*

(Received; Revised; Accepted)

Submitted to ApJS

ABSTRACT

This *supplement* paper presents the maps of HCN $J=4-3$, HNC $J=1-0$, H¹³CN $J=1-0$, and HC₃N $J=10-9$ for the Galactic central molecular zone (CMZ), which have been obtained using the Atacama Submillimeter Telescope Experiment and Nobeyama Radio Observatory 45-m telescope. Three-dimensional maps (2-D in space and 1-D in velocity) of the gas kinetic temperature (T_{kin}), hydrogen volume density (n_{H_2}), and fractional abundances of eight molecules (HCN, HNC, HC₃N, HCO⁺, H₂CO, SiO, CS, and N₂H⁺) have been constructed from our and archival data. We have developed a method with hierarchical Bayesian inference for this analysis, which has successfully suppressed the artificial correlations among the parameters created by systematic errors due to the deficiency in the simple one-zone excitation analysis and the calibration uncertainty. The typical values of T_{kin} and n_{H_2} are 10^{1.8} K and 10^{4.2} cm⁻³, respectively, and the presence of an additional cold/low-density component is also indicated. The distribution of high-temperature regions is poorly correlated with known active star-forming regions, while a few of them coincide with shocked clouds. Principal component analysis has identified two distinct groups in the eight analyzed molecules: one group with large PC1 and PC2 scores and the other with a large T_{kin} dependence, which could be explained using two regimes of shock chemistry with fast ($\gtrsim 20$ km s⁻¹) and slow ($\lesssim 20$ km s⁻¹) velocity shocks, respectively. This supports the idea that the mechanical sputtering of dust grains and the mechanical heating play primary roles in the chemical and thermal processes in CMZ clouds.

Keywords: Galaxy: center Galactic Center

1. INTRODUCTION

The innermost 200 pc of the Milky Way, or the central molecular zone (CMZ), is the Galactic version of the central molecular condensations observed in many spiral galaxies, which frequently act as molecular gas reservoirs that fuel starbursts and active galactic nuclei. The observation of dense molecular gas is of fundamental importance in studying the Galactic CMZ, where the cold interstellar medium is primarily confined in giant molecular clouds (GMCs) with a volume density $\gtrsim 10^3$ cm⁻³ (Morris & Serabyn 1996; Nagai et al. 2007). The dense gas in the CMZ has been intensively studied in various molecular transitions with high critical densities (n_{crit}) at millimeter (Tsuboi et al. 1999; Jones et al. 2012, 2013) and submillimeter (Oka et al. 2007; Ginsburg et al. 2016) wavelengths. This supplement paper reports the results of the new CMZ surveys in HCN $J=4-3$ at 350 GHz and three high-density tracer lines in the 3-mm band (H¹³CN $J=1-0$, HNC $J=1-0$, and HC₃N $J=10-9$), which were performed using the Atacama Submillimeter Telescope Experiment (ASTE) 10-m telescope and Nobeyama Radio Observatory (NRO) 45-m telescope. The HCN

$J=4-3$ transition, whose nominal n_{crit} is 10^7 cm^{-3} , is the highest-density tracer among those previously used in the CMZ survey, even though the effective n_{crit} can be 1–2 orders of magnitude lower owing to the photon trapping effect.¹

The measurement of the gas kinetic temperature (T_{kin}) and hydrogen volume density (n_{H_2}) is a fundamentally important issue in several fields of interstellar physics and chemistry. In star formation studies, the volume density is a key parameter for understanding the dynamical evolution and the current physical status of molecular clouds. Spatially resolved measurements of the temperature and density may assist in determining the mechanisms that fuel the well-known local starburst in the Sgr B complex and the formation of young massive clusters such as the Quintuplet and Arches clusters (Nagata et al. 1995; Morris & Serabyn 1996; Figer et al. 1999) while suppressing star formation in the remaining vast majority of the clouds (Longmore et al. 2012; Rathborne et al. 2014; Kruijssen et al. 2014). In addition, the CMZ is a unique target for studying molecular chemistry under the extreme environment of the innermost part of galaxies, where molecular clouds are exposed to intense ultraviolet (UV), X-ray, and cosmic-ray (CR) irradiation and placed in strong tidal and magnetic fields. The Galactic CMZ is known for several interesting chemical characteristics such as widespread hot-core-like chemistry (Requena-Torres et al. 2006), a rich abundance of SiO (Martín-Pintado et al. 1997), and an anomalously high atomic-carbon-to-CO abundance ratio (Tanaka et al. 2011). Information about the physical conditions is necessary for converting the molecular line *intensities* into their *abundances* and for investigating the dependence of the molecular abundances on environmental factors.

The immediate aim of this paper is to present 3-D (2-D in space and 1-D in velocity) maps of T_{kin} and n_{H_2} constructed using newly obtained data and published data taken from the literature. There are multiple previous studies on spatially resolved T_{kin} measurements, which use ammonia inversion lines (Nagayama et al. 2007; Ott et al. 2014; Arai et al. 2016), multi- J CO and ^{13}CO lines (Martin et al. 2004; Nagai et al. 2007), and H_2CO lines (Ginsburg et al. 2016) as probes. For the measurement of n_{H_2} , several studies have been conducted on the basis of observations of high-density tracers; however, they are primarily targeted at limited areas, and the large-scale distribution across the entire CMZ remains less studied. The analysis by Nagai et al. (2007) using low- J CO lines is the n_{H_2} measurement with the best spatial resolution and coverage until now, but its scope is limited to the outer low-density part of the clouds because of the selection of tracer lines with $n_{\text{crit}} \leq 10^4 \text{ cm}^{-3}$. The new analysis we present in this paper uses the intensity ratios among multitransition HCN lines as the primary density probe and realizes sufficient parameter coverage to study dense regions of the CMZ. In addition, the molecular line data of several popular species at the millimeter wavelength are incorporated, whereby we measure the spatial variations in their fractional abundances simultaneously with the physical conditions.

Our analysis was conducted using a method that we developed by employing the hierarchical Bayesian (HB) inference technique. In a few cases, the standard maximum likelihood (ML) method is unsuitable for analysis involving a large number of molecular lines because it is susceptible to unmeasurable systematic errors due to the calibration uncertainty and the approximations adopted in the model. The HB analysis realizes more robust parameter inference by introducing a prior probability function that applies stronger constraints on the behavior of the parameters.

The outline of this paper is as follows: In Section 2, we describe the details of the observations performed using the ASTE 10-m telescope and NRO 45-m telescope. The data are presented in Section 3. Section 4 describes the HB model, and its results are presented in Section 5. Section 6 describes the investigation of the mechanisms that govern the distribution of T_{kin} and the molecular abundances. The identification of high-density clumps in the HCN $J=4-3$ maps and the investigation of their star-forming activities will be provided in a separate forthcoming paper.

2. OBSERVATIONS

We observed the HCN $J=4-3$ line using the ASTE 10-m telescope and the H^{13}CN $J=1-0$, HNC $J=1-0$, and HC_3N $J=10-9$ lines with the NRO 45-m telescope. The frequencies, upper state energies (E_u), and critical densities of the target lines are listed in Table 1. The observed regions are shown in Figure 1. The primary parts of the four major GMC complexes in the CMZ, i.e., Sgr A–D, are observed in all four lines, even though the gap region between the Sgr B and D complexes (Galactic longitude of 0.8° to 1.1°) is not included in the ASTE observations. The HCN $J=4-3$ and H^{13}CN $J=1-0$ maps of the Sgr C complex ($-0.6^\circ < l < -0.3^\circ$) have been published in a separated paper (Tanaka et al. 2014).

2.1. ASTE Observations

The ASTE HCN $J=4-3$ observations were performed during the following four periods: the first from August to September 2010, the second from April to May 2011, the third in November 2011, and the last in August 2013. The target regions were mapped using multiple on-the-fly (OTF; Sawada et al. 2008) scans, each covering a subregion of $20'$ square or less. The fields mapped in the four periods are shown in Figure 1. The scans in the X and Y directions

¹ In this paper, we adopt the definition of n_{crit} given in Equation 4 of Shirley (2015); $n_{\text{crit}} \equiv A_{i,j} / \sum_{k \neq i} \gamma_{i,j}$ for the $i \rightarrow j$ level transition, where A and γ are the Einstein A coefficient and collisional excitation rate, respectively.

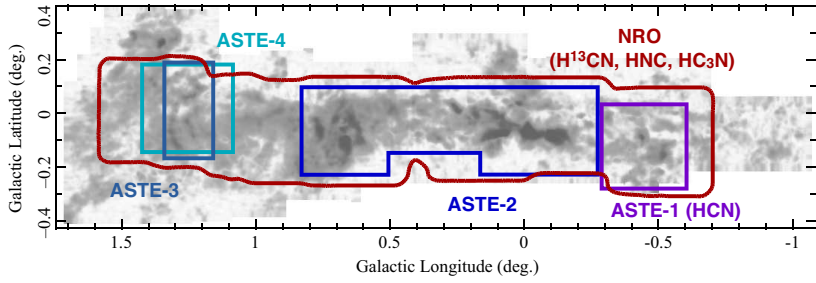


Figure 1. Mapping regions of the ASTE HCN $J=4-3$ observations and the NRO HNC, $H^{13}CN$, and HC_3N observations superposed on the grayscale map of the CS $J=1-0$ peak intensity (Tsuboi et al. 1999). The mapping regions for the four ASTE observation periods are indicated with different colors.

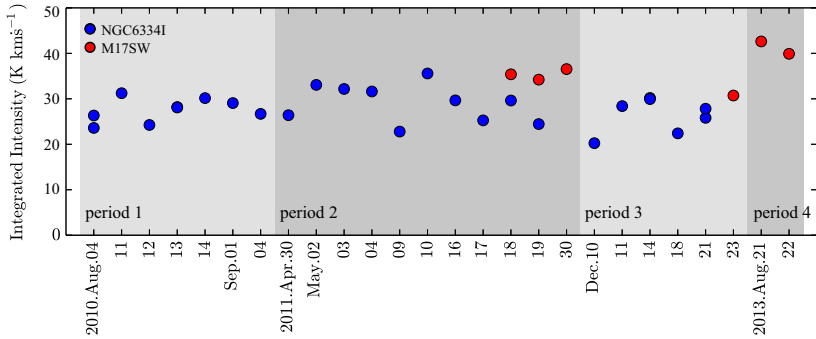


Figure 2. Velocity-integrated HCN $J=4-3$ intensities of the calibrators in the scale of the chopper-wheel calibrated intensity, measured at different dates during observation periods 1–4. The blue and red points denote NGC6334 and M17SW, respectively.

(i.e., in the directions of Galactic longitude and latitude, respectively) were obtained for each subregion to mitigate the scanning effect. The off position was taken at $(l, b) = (0^\circ, -1^\circ)$, where we confirmed the absence of significant HCN $J=4-3$ emission during the observations. The total observation time over the four periods was 76 hours including the integration time for off-position integration and intensity calibration, and the dead-time for antenna acceleration and the transient time between scan rows. A sideband-separation-type receiver CATS345 was used as the receiver frontend. The telescope beamsize at 350 GHz was $22''$. The backend was a 1024-channel auto-correlator system with a channel separation of 500 kHz, which provided a velocity separation of 0.44 km s^{-1} and a spectral coverage of 400 km s^{-1} per sideband at 350 GHz. We observed the CO $J=3-2$ line toward V1427 Aql or RAFGL5379 approximately every 1 hour to maintain the pointing accuracy within $< 3''$ during observation runs. The antenna temperatures were calibrated using the standard chopper wheel method.

We utilized the NOSTAR package developed by the NRO, for flagging bad data with unstable spectral baselines, the subtraction of spectral baselines, and the reduction of the data into $l-b-v_{\text{LSR}}$ data cubes. A third-degree polynomial fitting was applied to spectral baseline subtraction to remove standing noise. Spectral data were spatially convolved using a Gaussian-tapered Bessel function and resampled onto an $8.5'' \times 8.5'' \times 2 \text{ km s}^{-1}$ grid. The final effective spatial resolution was $24''$. The X- and Y-scan maps were combined into one map by employing the *PLAIT* algorithm to remove scanning noise (Emerson & Gräve 1988). The typical noise per voxel is 0.14 K in the T_{MB} scale.

The calibrator sources NGC6334I and M17SW were observed more than once in each observation period to measure the correction factor for the main-beam efficiency and image rejection ratio (IRR) and its instrumental variability among the four observation periods. Figure 2 shows the measured chopper-wheel-calibrated HCN $J=4-3$ intensities of the calibrators. As compared to the first two periods, there is a significant decline in the NGC6334I intensity in period 3; the averaged intensities are $4.15 \pm 0.10 \text{ K}$, $4.25 \pm 0.15 \text{ K}$, and $3.63 \pm 0.25 \text{ K}$ for periods 1, 2, and 3, respectively. Hence, we multiplied the data by a factor of 1.16 during period 3 to correct this variation. On the contrary, the M17SW intensity rises in period 4 as compared to the first three periods; the averaged intensity for periods 2 and 3 after applying the above-mentioned correction is $5.86 \pm 0.12 \text{ K}$, while that for period 4 is $6.49 \pm 0.28 \text{ K}$. We applied a correction factor of 0.90 for period 4. After these corrections, we obtain the averaged intensities of NGC6334I and M17SW as $4.12 \pm 0.10 \text{ K}$ and $5.86 \pm 0.09 \text{ K}$, respectively, with a relative daily variation of 10%. By comparing the M17SW intensity measured using the Caltech Submillimeter Observatory ($9.8 \pm 0.3 \text{ K}$; Wang et al. 1994), we estimate the scaling factor for the main-beam efficiency and IRR to be 1.67 ± 0.06 . The total systematic calibration errors

are approximately estimated to be 0.1 from the daily variation in the calibrator intensities and the uncertainty in the scaling factor.

2.2. NRO 45-m Observations

The H^{13}CN $J=1-0$, HNC $J=1-0$, and HC_3N $J=10-9$ lines were observed in January 2010 using the 25-beam array receiver system BEARS (Sunada et al. 2000) installed on the NRO 45-m telescope. The three lines were simultaneously observed in the double sideband (DSB) mode: H^{13}CN in the lower sideband and HNC and HC_3N in the upper sideband.

We operated the digital backend in the wide-band mode with a channel separation of 0.5 MHz and a total bandwidth of 512 MHz, which correspond to a velocity channel separation of 1.7 km s^{-1} and a velocity coverage of 1748 km s^{-1} at 90 GHz. Velocity ranges from -200 km s^{-1} to $+200 \text{ km s}^{-1}$ were covered by the spectrometer for the H^{13}CN and HNC lines; however, the velocities lower than -150 km s^{-1} in the HC_3N line were outside the correlator bandwidth. The observation region was covered by performing multiple OTF scans for subregions whose sizes were $20'$ square or less. The scans were performed in a manner such that each of the 25 beams of the BEARS multibeam receiver conducts full Nyquist sampling over the target region; then the resultant 25 maps were integrated into one map after the variations in the IRR and sensitivity among the beams were corrected. X and Y scans were obtained for each subregion. The antenna pointing accuracy was maintained within $5''$ by observing the SiO $J=1-0$, $v = 1, 2$ maser lines toward VX-Sgr.

The data were converted into $l-b-v_{\text{LSR}}$ data cubes with a $10.275'' \times 10.275'' \times 2 \text{ km s}^{-1}$ grid using the same procedure as that for the ASTE data reduction, except for an additional correction for the variations in the sideband ratios among the 25 receiver units. The relative correction factors were obtained by performing self-calibration for each sideband; we measured the ratios of the chopper-wheel-calibrated intensities among the 25 maps created for individual receiver channels. The absolute values of the DSB correction factors were obtained by comparing the intensity toward Sgr B2 with the intensity measured using the S100 receiver. The value of η_{MB} of the S100 receiver at 86 GHz is measured to be 0.45 by the observatory. The effective beam size of the final maps was $\sim 20''$ after convolution is applied in the imaging process. The typical values of the noise per voxel are 0.19 K, 0.21 K, and 0.17 K for the H^{13}CN , HNC , and HC_3N maps, respectively, in the T_{MB} scale. The voxels in peripheral regions with RMS noise levels of the H^{13}CN spectra above 0.4 K in the T_{MB} scale were removed from the maps.

3. DATA

Figure 3 shows the peak intensity maps of the observed lines smoothed with Gaussian kernels having an FWHM of 10 km s^{-1} . Note that low saturation levels are applied in the HCN and HC_3N maps to soften the image contrast due to the extremely bright emission from the Sgr B2 cluster-forming region. The $1-\sigma$ noise maps calculated from the emission-free spectral channels are shown in Figure 4. The velocity channel maps in bins with widths of 20 km s^{-1} and the longitude–velocity diagrams in latitude bins of $1.5'$ are presented in Figures 5 and 6, respectively, which are attached at the end of the paper.

The overall spatial extension of molecular gas is best traced by the HNC $J=1-0$ map, where both intense emission from the central regions of the GMC complexes and low-level emission surrounding them are visible owing to the relatively low n_{crit} and E_u compared with the other lines. The H^{13}CN map is similar to the HNC map, except that the low-level emission is less clear owing to the low S/N ratio. The HCN $J=4-3$ and HC_3N maps are more dominated by compact features compared with the other two maps; their bright emissions are limited to the narrow areas close to the centers of the GMC complexes of the Sgr A, Sgr B, and M0.11–0.08 regions and several compact clumps such as the brick cloud (G0.253+0.016), CO–0.40, and CO–0.30 (Tanaka et al. 2014). Low-level emissions primarily have a clumpy or filamentary shape, and diffuse extended emissions are absent or considerably weak except for the envelopes of the Sgr B and Sgr A complexes. The most conspicuous feature in the HCN $J=4-3$ and HC_3N maps is the bright compact emission from the Sgr B2 cluster-forming region, which is observed as absorption holes in the HNC and H^{13}CN maps against a strong continuum that is subtracted in the data reduction process.

Considering that the upper state energies of HCN $J=4-3$ and HC_3N are relatively high and their critical densities differ by two orders of magnitude, their morphological similarity to each other and difference from the other two lines suggest that the ratios between the intensities of different lines primarily reflect the temperature variation. Therefore, the conventional assumption of constant T_{kin} cannot be used for measuring n_{H_2} through the excitation analysis; the distributions of T_{kin} and n_{H_2} must be determined simultaneously.

4. PHYSICAL CONDITIONS AND MOLECULAR ABUNDANCES: METHODS

The purpose of this study is to construct 3-D maps (2-D in space and 1-D in velocity) of the physical conditions and molecular abundances from our molecular line maps. This section (§4) is devoted to a description of the non local thermodynamical equilibrium (non-LTE) method and the HB inference used for the analysis. The first subsection (§4.1) describes the parameters calculated with the non-LTE method. We overview the framework for the parameter inference using the HB method in Subsection 4.2. Full details of the probability density functions (PDFs) used in the

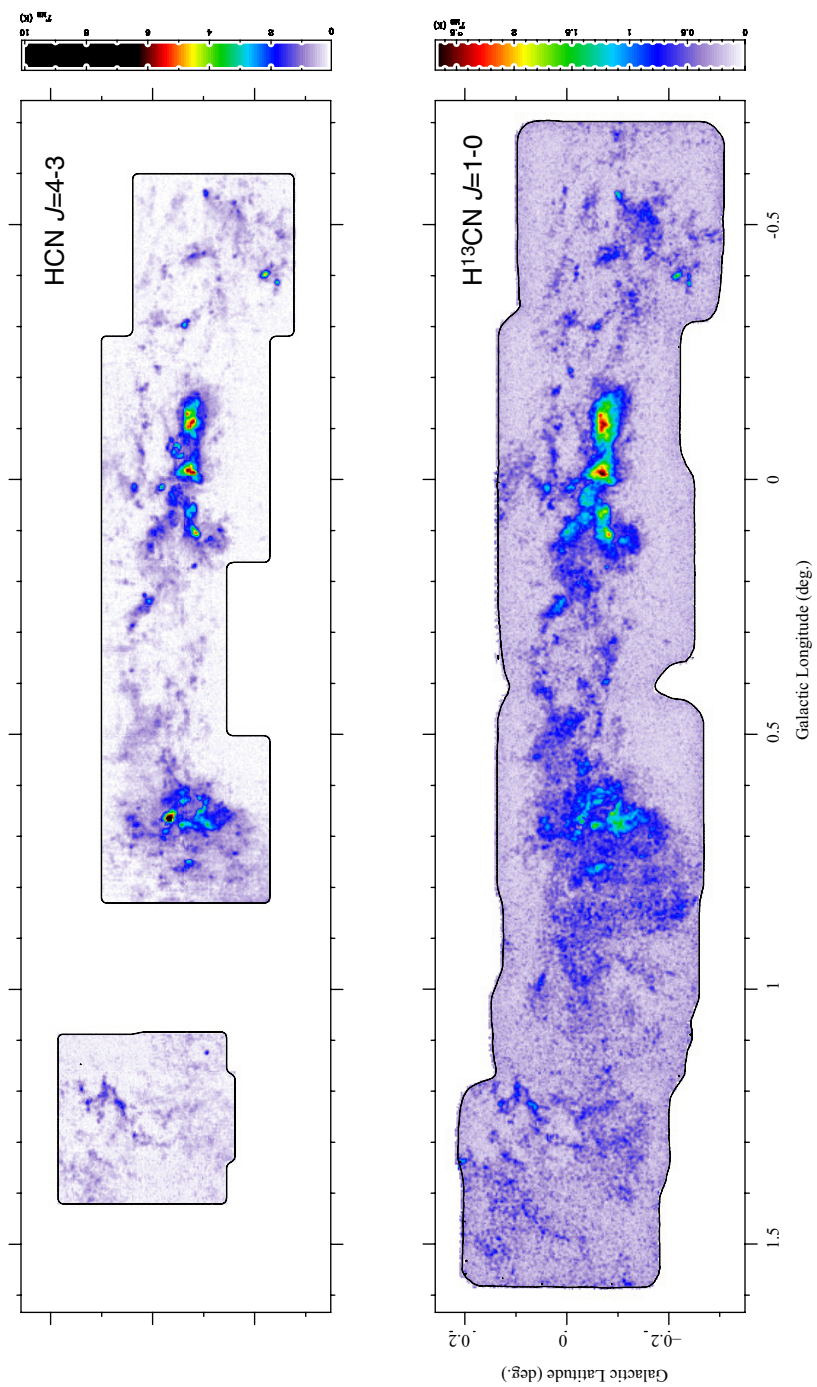


Figure 3. Peak intensity maps of the observed lines, calculated after smoothing along the velocity axis with 10-km s^{-1} FWHM kernels.

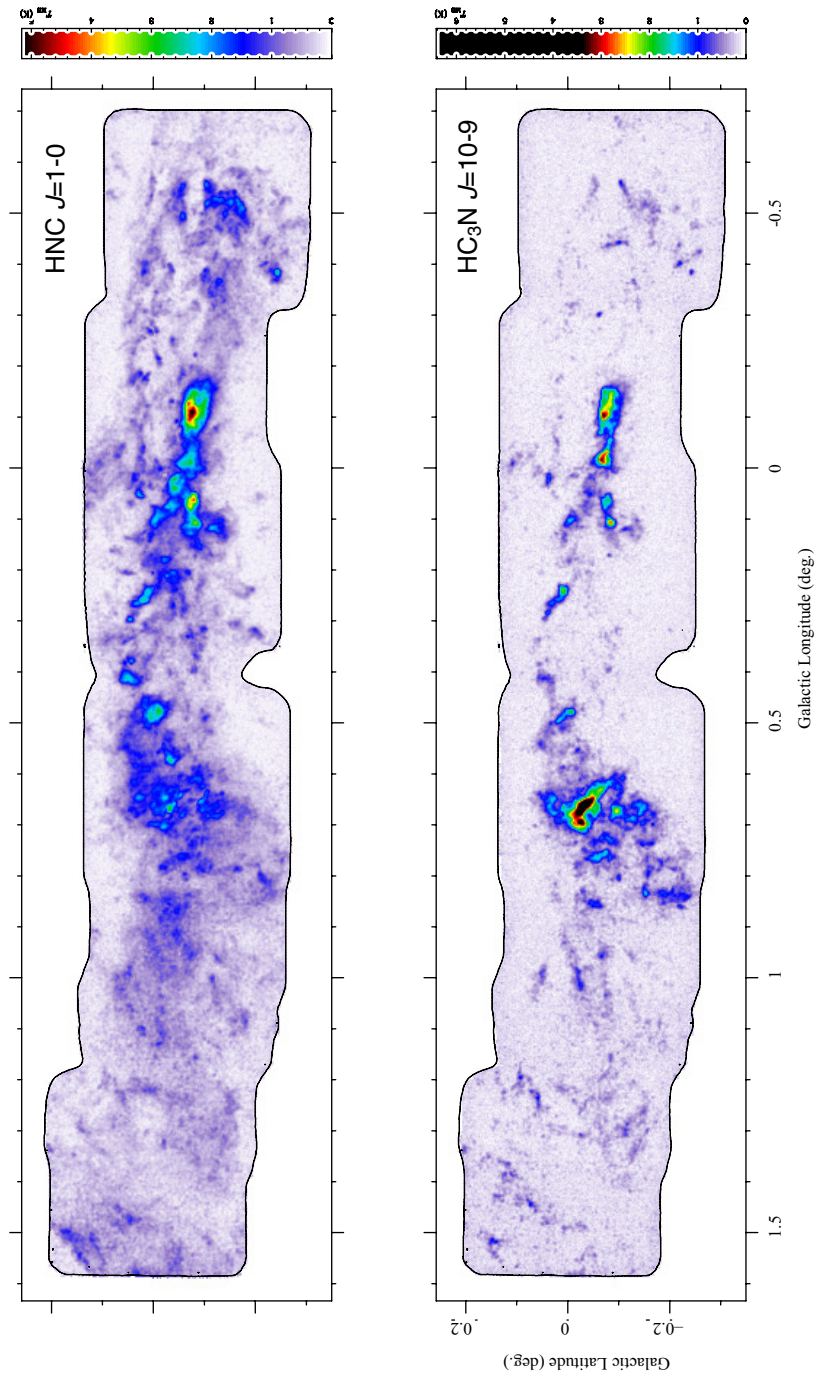


Figure 3 (Continued). Peak intensity maps of the observed lines, calculated after smoothing along the velocity axis with 10-km s^{-1} FWHM kernels.

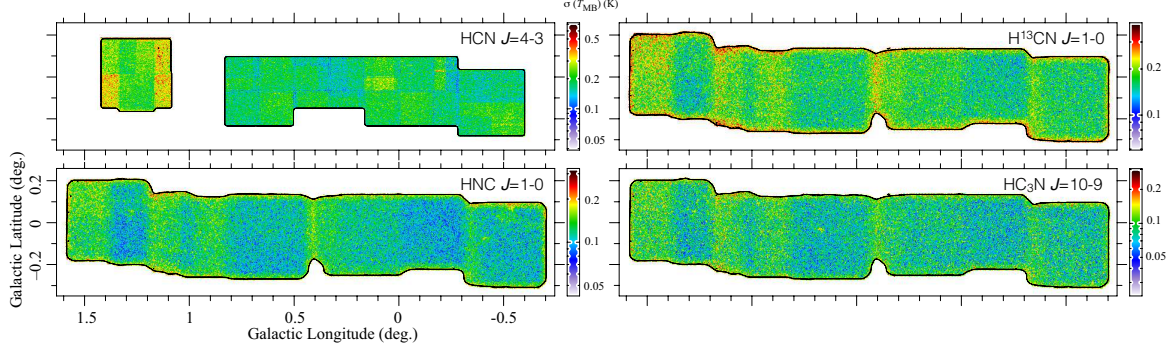


Figure 4. Maps of the $1\text{-}\sigma$ noise levels of the observed lines in logarithmic color scales.

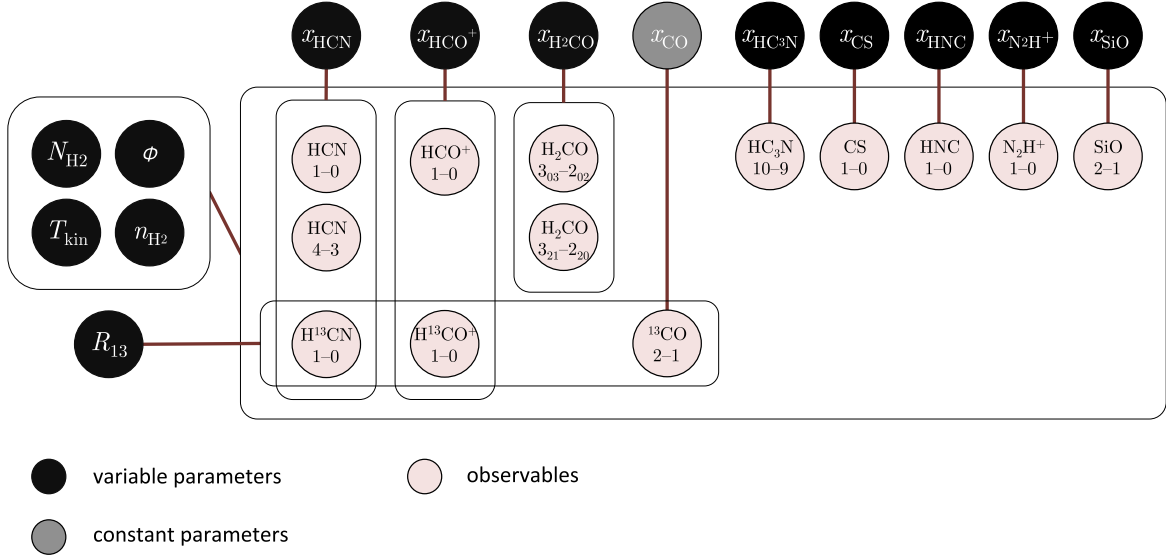


Figure 7. Schematic diagram showing the dependencies of the observed line intensities on the model parameters. Four parameters, N_{H_2} , T_{kin} , n_{H_2} , and Φ affect all line intensities. These parameters and molecular abundances x_{mol} determine the individual line intensities. The ^{13}C isotopologue lines (H^{13}CN $J=1-0$, H^{13}CO^+ $J=1-0$, and ^{13}CO $J=2-1$) have additional dependencies on R_{13} .

HB method are given in Subsection 4.3. We also present the numerical method to calculate the posterior distribution (§4.5), a comparison with a simple nonhierarchical method (§4.6), and the details of the input data (§4.7). The results of the analysis are presented in the next section (§5).

4.1. Parameters

This analysis requires a larger dataset including other transitions of the molecules we observed, as the number of the observed lines (four) is less than the minimum number of parameters to be determined, i.e., six (the gas kinetic temperature T_{kin} , the hydrogen volume density n_{H_2} , the hydrogen column density per unit velocity width N_{H_2} , the ratios between the fractional abundances x_{mol} of the three molecules, and the beam filling factor Φ). We use the additional data of the nine lines listed in Table 1, which are taken from the literature (Tsuboi et al. 1999; Jones et al. 2012; Tsuboi et al. 2015; Ginsburg et al. 2016), and determine 13 values, i.e., T_{kin} , n_{H_2} , N_{H_2} , Φ , the $\text{C}/^{13}\text{C}$ isotopic ratio (R_{13}), and x_{mol} of eight molecules (HCN, HCO^+ , N_2H^+ , HNC, CS, SiO, HC_3N , and $p\text{-H}_2\text{CO}$).

The model parameters are described in Table 2. We use the logarithms of the parameters to constrain their values to be positive. We introduce the parameter ϕ , which defines the beam filling factor as $\Phi = 1 - e^{-\phi}$, instead of directly including Φ in the model parameter set; this formulation limits Φ within a finite range of $[0, 1]$, whereby we can assume infinite variable ranges for all model parameters. We fix the ^{12}C fractional abundance at 10^{-4} and use the molecule as a proxy for H_2 . The ^{13}C isotopic abundance is assumed to be common for all C-bearing species.

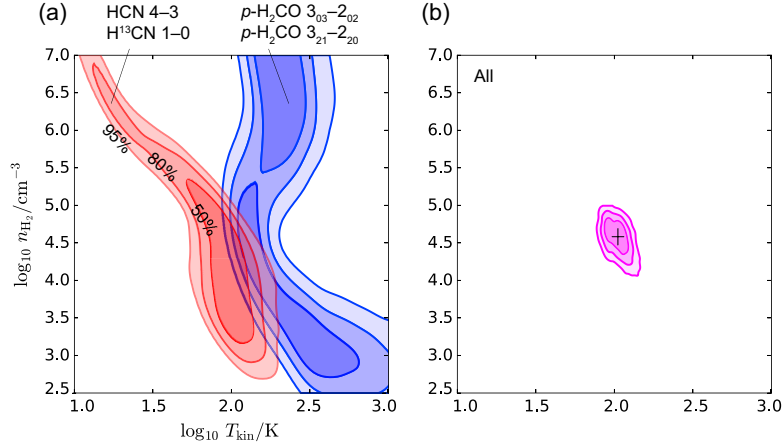


Figure 8. (a) $T_{\text{kin}}-n_{\text{H}_2}$ ranges calculated for the center position of the 50-km s $^{-1}$ cloud using the LVG analysis, where $\Phi=0.25$ and $R_{13}=25$ are assumed. The red contours are for the simultaneous credible intervals calculated from the HCN $J=4-3$ and $\text{H}^{13}\text{CN } J=1-0$ intensities, and the blue contours are those for the two H_2CO lines ($3_{21-2_{20}}$ and $3_{22-2_{21}}$). The credible intervals are calculated using the nonhierarchical Bayesian analysis with a flat prior function. (b) The credible intervals calculated using the four lines simultaneously. The cross mark denotes the median of the simultaneous probability.

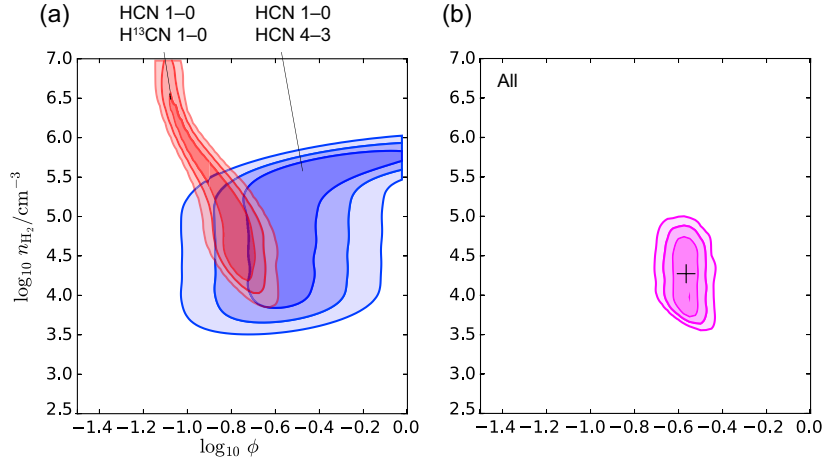


Figure 9. (a) $\phi-n_{\text{H}_2}$ ranges calculated for the center position of the 50-km s $^{-1}$ cloud using the LVG analysis, where $T_{\text{kin}}=10^2$ and $R_{13}=25$ are assumed. The red contours are for the simultaneous credible intervals calculated from the HCN $J=1-0$ and $\text{H}^{13}\text{CN } J=1-0$ intensities, and the blue contours are those for the HCN $J=1-0$ and $J=4-3$ lines. The credible intervals are calculated using the nonhierarchical Bayesian analysis with a flat prior function. (b) The credible intervals calculated using the three lines simultaneously. The cross mark denotes the median of the simultaneous probability.

Figure 7 shows a schematic diagram of the dependencies of the molecular line intensities on the model parameters. In the non-LTE scheme the line intensities are a function of three parameters: the column density per unit velocity width ($N_X = x_{\text{mol}}(X) \cdot N_{\text{H}_2}$), n_{H_2} , and T_{kin} . The column density of ^{13}C isotopologues is given as a product of R_{13} and the column density of the main ^{12}C isotopologues. Intensities multiplied by a beam filling factor Φ are the intensities that are actually observed with telescopes. Hence, as $x_{\text{mol}}(\text{CO})$ is constant in our model, $(N_{\text{mol}} + 4)$ parameters are necessary to calculate the observed line intensity, where N_{mol} is the number of molecular species not including ^{13}C isotopologues.

The emissivity per unit N_{H_2} is dependent on the population distribution among the internal energy levels in the molecule, which is determined by the equilibrium between radiative transitions, excitation by photon trapping, and excitation/de-excitation through collisions with molecular hydrogens. The rates of these processes depend on the transition dipole moments and the collisional cross sections; hence, different lines have different dependencies on T_{kin} and n_{H_2} . Figure 8a shows the $T_{\text{kin}}-n_{\text{H}_2}$ parameter range calculated using the large velocity gradient (LVG)

analysis (Goldreich & Kwan 1974) from the HCN $J=4-3$ and H^{13}CN $J=1-0$ intensities toward the 50-km s^{-1} cloud on the assumption that $R_{13}=25$ and $\Phi=0.25$. The rectangular-prior Bayesian analysis (§4.6) is used for parameter inference. The highest probability parameter set is not uniquely determined since the number of input data (two) is less than the number of the free parameters (three; note that $x_{\text{mol}}(\text{HCN})$ and N_{H_2} degenerate in the parameter space). Figure 8a also shows the parameter range calculated using the two $p\text{-H}_2\text{CO}$ lines; their intensity ratio is a good probe of T_{kin} as it is insensitive to n_{H_2} (Mangum & Wootten 1993; Ginsburg et al. 2016). Thus the unique solution ($T_{\text{kin}}, n_{\text{H}_2} = (10^2 \text{ K}, 10^{4.5} \text{ cm}^{-3})$) is obtained by combining the HCN and H_2CO results when R_{13} and Φ are given.

The parameters N_X and Φ degenerate in optically thin lines, but as the optical depth increases the intensity depends nonlinearly on N_X ; hence, the optically thick lines, HCN $J=1-0$ and HCN $J=4-3$ in our dataset, contain information on Φ . Figure 9 shows the $\Phi\text{-}n_{\text{H}_2}$ parameter ranges calculated from the three HCN lines toward the 50-km s^{-1} cloud, assuming $T_{\text{kin}} = 10^2 \text{ K}$ and $R_{13} = 25$. Φ is determined well as $\log_{10} \Phi = -0.56 \pm 0.06$ in this example. R_{13} is mainly measured from the intensity ratio of the $\text{HCO}^+ J=1-0$ line to its ^{13}C isotopologue line, as they are generally not too optically thick in the CMZ (Riquelme et al. 2013). Therefore, the seven lines from HCN, H_2CO , and HCO^+ and their ^{13}C isotopologues are sufficient to determine the physical condition parameters.

The HNC, N_2H^+ , HNC, CS, SiO, and HC_3N data are primarily used to estimate their abundances; since multitransition data of these species are not included in our dataset, they do not contain significant information of the physical condition parameters. The molecular abundances are measured in the unit of fractional abundance to N_{H_2} , whose column density is obtained from the ^{13}CO data.

4.2. Hierarchical Bayesian Analysis

We determine the optimal parameter distribution, $\mathbf{p} = \{\mathbf{p}_i\}$, from the observed line intensities $\mathbf{I} = \{\mathbf{I}_i\}$ using the above non-LTE framework. The subscript index i ($\in \{1, 2, \dots, N\}$) specifies a voxel in the 3-D space. The individual line intensities and parameters at the i^{th} voxel are represented by the vector components $I_{i,j}$ ($j \in \{1, 2, \dots, N_l\}$) and $p_{i,k}$ ($k \in \{1, 2, \dots, N_p\}$), respectively, where N_p and N_l are the numbers of parameters and lines, respectively, both of which are 13 in our analysis.

The ML method is commonly used for parameter optimization problems; it is designed to define \mathbf{p} that maximizes the likelihood function

$$P(\mathbf{I}|\mathbf{p}) = \prod_{i,j} \frac{1}{\delta_{i,j}} \exp \left[-\frac{1}{2} w_j \left(\frac{I_{i,j} - F(\mathbf{p}_i)_j}{\delta_{i,j}} \right)^2 \right], \quad (1)$$

where $F(\mathbf{p}_i)$ denotes the model intensities calculated with the non-LTE analysis. The factor w_j is the weight of the j^{th} line in the fitting. The notation $P(\mathbf{x}|\mathbf{a})$ represents a conditional probability density function (PDF) for the variable \mathbf{x} when the parameter \mathbf{a} is given. A normal error distribution with a standard deviation of $\delta_{i,j}$ is assumed for each $I_{i,j}$. Here and henceforth, we omit the normalization constants in the expressions of PDFs wherever possible. The rectangular-prior Bayesian analysis used in the previous subsection is essentially equivalent to the ML method, as we will show in a later section (§4.6).

The ML method frequently does not provide a satisfactory solution for the excitation analysis due to insufficient information about the errors present in the observations and models. In addition to random noise δ , which explicitly appears in Equation 1, the input data may contain systematic errors due to calibration errors and uncertainty in spectral baseline subtraction, which are difficult to measure. Moreover, systematic errors could be also introduced by the simplifications used in the model, such as the assumption of spatial uniformity along the line of sight and within the beam and the LVG approximation; in general, different lines could probe different depths of molecular clouds according to their upper state energies and critical densities, and this discrepancy from the ideal one-zone situation is regarded as a systematic error. Furthermore, the lack of resolution for separating multiphase gas is non-negligible; interferometric observations have shown that cold quiescent clumps and warm turbulent filaments with a size of $\sim 0.1 \text{ pc}$ ($\sim 1''.5$) are frequently entangled in typical single-dish beam sizes ($10''\text{--}20''$). Another potential source of systematic errors in our analysis is the omission of the isotopic fractionation in C-bearing species. These systematic errors can seriously affect the results of the excitation analysis. As we will show in Subsection 5.3, nonhierarchical Bayesian analysis that is equivalent to the ML method creates an anticorrelation between n_{H_2} and N_{H_2} , which is likely to be unphysical since the column and volume densities should be positively correlated in realistic clouds. This nonphysical anticorrelation is caused by the degeneracy of n_{H_2} and N_{H_2} in the LVG model; the standard ML method fails to resolve the degeneracy owing to the insufficient information about the systematic errors. A severe degeneracy also exists between N_{H_2} and Φ , as both parameters scale the line intensities in the model.

We adopt a Bayesian inference method similar to that used for the spectral energy distribution (SED) fittings of thermal dust emission (Kelly et al. 2012). The basic idea of the Bayesian analysis is to apply additional constraints on the parameters by introducing the prior probability, thereby making it possible to assume reasonable values of the

systematic errors and to forbid the parameters from exhibiting unphysical behaviors. First, we modify the likelihood function (Equation 1) to a form that includes a factor that represents the systematic errors, $\epsilon = \{\epsilon_{i,j}\}$:

$$P(\mathbf{I}|\mathbf{p}, \epsilon) = \prod_{i,j} \frac{1}{\delta_{i,j}} \exp \left[-\frac{1}{2} w_j \left(\frac{I_{i,j} - \epsilon_{i,j} \cdot F(\mathbf{p}_i)_j}{\delta_{i,j}} \right)^2 \right]. \quad (2)$$

The systematic errors are assumed to be multiplicative because we consider calibration errors and the deviation from the one-zone LVG model for error sources, which are likely to affect the intensities in multiplicative manners. The ML method cannot determine the unique optimal parameters for this modified likelihood function because the degree of freedom is less than zero. Instead, the Bayesian method evaluates the posterior probability given by Bayes' theorem:

$$P(\mathbf{p}, \epsilon|\mathbf{I}) = \frac{P(\mathbf{I}|\mathbf{p}, \epsilon) \cdot P(\mathbf{p}, \epsilon)}{P(\mathbf{I})}. \quad (3)$$

The posterior probability $P(\mathbf{p}, \epsilon|\mathbf{I})$ is the conditional PDF of the explanatory parameters (\mathbf{p}, ϵ) where the observable \mathbf{I} is given. $P(\mathbf{p}, \epsilon)$ is the prior function, which is the simultaneous PDF for \mathbf{p} and ϵ given *a priori* by assumptions and information other than \mathbf{I} . The denominator, $P(\mathbf{I}) = \int P(\mathbf{I}|\mathbf{p}, \epsilon) \cdot P(\mathbf{p}, \epsilon) \cdot d\mathbf{p} \cdot d\epsilon$, is the normalization constant of the posterior, which can be omitted in the analysis.

The specific form of the prior is usually determined using statistical or physical modeling, as prior functions are not directly measurable. One approach to model the prior probability is to use a function that explicitly limits the parameter variation within physically allowed ranges, such as rectangular or logistic functions (e.g. Kamenetzky et al. 2012). In this paper, we adopt another approach using the HB modeling, which uses a prior that is further parameterized by the hyperparameter θ :

$$P(\mathbf{p}, \epsilon, \theta|\mathbf{I}) = \frac{P(\mathbf{I}|\mathbf{p}, \epsilon) \cdot P(\mathbf{p}, \epsilon|\theta) \cdot P(\theta)}{P(\mathbf{I})}, \quad (4)$$

where $P(\theta)$ is the hyperprior function, which defines the prior distribution on θ . In this analysis we adopt log-normal and multivariate Student functions for ϵ and \mathbf{p} , respectively, whose mean values and scale factors are treated as hyperparameters; namely, we assume that the *a priori* probability of the parameters has a unimodal distribution with unknown means and widths. This is one of the simplest ways to model a prior distribution that is more realistic than a flat or rectangular distribution; for example, n_{H_2} and N_{H_2} are known to have log-normal PDFs in turbulent-dominated molecular gas from theories and observations (e.g. Nordlund & Padoan 1999; Pineda et al. 2010). The usage of unimodal priors ensures that the posterior distribution has at least one peak even when the likelihood function does not have a unique maximum value.

In this analysis we basically use a flat hyperprior distribution for θ , but use logistic functions for a few hyperparameter elements whose variable ranges have to be explicitly controlled. We summarize the hierarchical structure of the variables and PDFs in the HB analysis in the schematic diagram in Figure 10. The specific functional forms of the prior and hyperprior are given in the next subsection (§4.3). Examples of the function shapes used as the prior and hyperprior functions, the multivariate Student function, the log-normal function, and the logistic function, are presented in 2-D or 1-D space in Figure 11.

Note that the explanatory parameter \mathbf{p} is a probability variable in the posterior function, whereas the ML method treats it as a constant parameter that defines the likelihood function. Hence, the goal of the analysis is to calculate the numerical values of the posterior probability, and the determination of the parameter for the maximum probability is not a necessary step. The probability distribution of an individual parameter is given by the marginal posterior PDF, which are obtained by integrating the posterior $P(\mathbf{p}, \epsilon, \theta|\mathbf{I})$ with the parameters that are not of interest. The marginal posterior of an arbitrary value X is

$$P(X|\mathbf{I}) \equiv \int \delta(X - y(\mathbf{p}, \epsilon)) \cdot P(\mathbf{p}, \epsilon, \theta|\mathbf{I}) \cdot d\mathbf{p} \cdot d\epsilon \cdot d\theta, \quad (5)$$

where $y(\mathbf{p}, \epsilon)$ is the function that relates the variable X and the model parameters. We use the median \tilde{X} and the 25th–75th-percentile interval Δ_X of $P(X|\mathbf{I})$ as the representative value and the uncertainty in the inferred parameter, respectively.

4.3. Priors and Hyperpriors

4.3.1. Systematic Errors

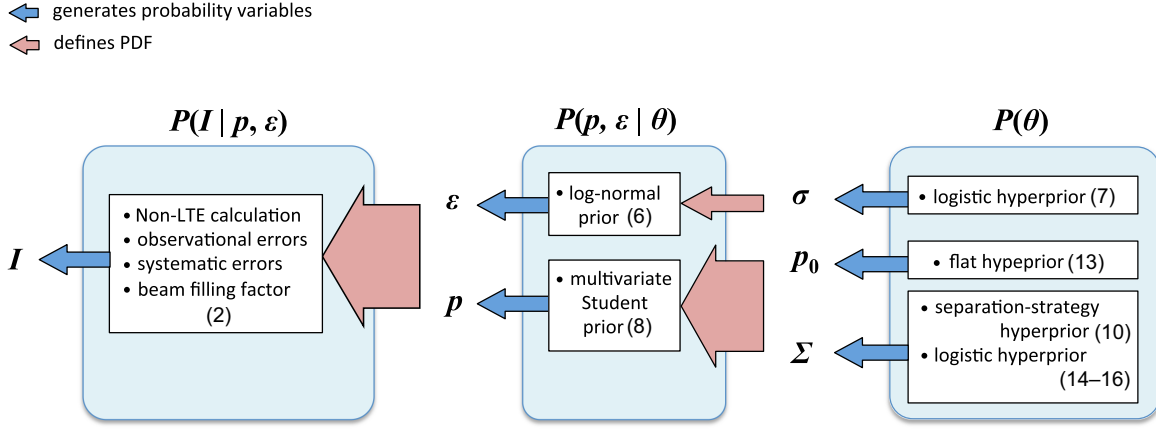


Figure 10. Schematic diagram showing the hierarchical structure of the variables and probability functions in the HB analysis. The numbers in parentheses are the equation numbers where the functions are defined in the text. In the first level (rightmost in the figure), the hyperparameter $\theta = (\mathbf{p}_0, \mathbf{\Sigma}, \sigma)$ is a probability variable generated according to the probability given by the hyperprior function, $P(\theta)$. In the next level of the hierarchy, θ is an input parameter of the prior function $P(\mathbf{p}, \epsilon | \theta)$ that defines the PDF for the parameter \mathbf{p} and systematic errors ϵ . The likelihood function $P(\mathbf{I} | \mathbf{p}, \epsilon)$ defined by \mathbf{p} and ϵ gives the PDF for the observables. Note that the prior and hyperprior limit the statistical properties of the parameters, and the observational constraints from the physical processes are first considered in the likelihood function.

The hyperparameter θ consists of three independent variables, i.e., σ , \mathbf{p}_0 , and $\mathbf{\Sigma}$. The parameter σ defines the prior for systematic errors, ϵ , for which we assume a log-normal form (Figure 11a) as follows:

$$P(\epsilon | \sigma) = \prod_{i,j} \frac{1}{\sigma_j \cdot \epsilon_{i,j}} \cdot \exp \left[-\frac{1}{2} \left(\frac{\ln \epsilon_{i,j}}{\sigma_j} \right)^2 \right]. \quad (6)$$

By adopting this formulation, which omits the cross terms of $\epsilon_{i,j}$, we implicitly assume that they are not correlated. $P(\epsilon | \sigma)$ is maximum at $\ln \epsilon_{i,j} = 0$ for all i and j ; therefore, the HB analysis will choose solutions with $\epsilon_{i,j}$ closer to unity if the other conditions are equal.

A logistic hyperprior is assumed for σ :

$$P(\sigma) = \prod_j \frac{1}{1 + \exp[-a \cdot (\sigma_j - \sigma_{\min,j})]}, \quad (7)$$

which gives 0 for $\sigma_j < \sigma_{\min,j}$ and 1 otherwise for sufficiently large positive a values (Figure 11c). We find $a = 1000$ works for our problem. The lower limit values σ_{\min} are manually given parameters, which approximately correspond to the calibration uncertainties in the observations. We fix $\sigma_{\min,j} = 0.1$ for all j .

4.3.2. Physical Conditions and Molecular Abundances

The other two hyperparameters, \mathbf{p}_0 and $\mathbf{\Sigma}$, define the prior for \mathbf{p} . We adopt a multivariate Student prior (Figure 11b), which is one of the simplest ways to model a unimodal PDF for parameters that are potentially correlated with each other:

$$P(\mathbf{p} | \mathbf{p}_0, \mathbf{\Sigma}) = |\mathbf{\Sigma}|^{-\frac{N}{2}} \cdot \prod_i \left[1 + \frac{1}{\nu} (\mathbf{p}_i - \mathbf{p}_0)^T \cdot \mathbf{\Sigma}^{-1} \cdot (\mathbf{p}_i - \mathbf{p}_0) \right]^{-\frac{\nu + N_p}{2}}, \quad (8)$$

where $\mathbf{\Sigma}$ and \mathbf{p}_0 denote the scale matrix and central value vector, respectively. We fix the shape parameter ν as 2. It is theoretically and observationally known that the PDFs of N_{H_2} and n_{H_2} are log-normal-shaped in turbulence-dominated gas, frequently with a power-law tail to the high-density end in self-gravitating clouds. We aim to emulate multicomponent turbulence and self-gravitating portions using the Student prior with a small ν , as it allows more outliers than the normal prior with the same scale matrix. The hyperparameter $\mathbf{\Sigma}$ defines the *prior* distribution of \mathbf{p} , which is not equal to the *posterior* variance–covariance matrix calculated using ${}^t\mathbf{p} \cdot \mathbf{p}$.

Table 1. Input Data

molecule	transition	frequency ^a (GHz)	E_u/k_B^a (K)	$\log_{10} n_{\text{crit}}^{a,b}$ (cm^{-3})	δ^c (mK)	reference
HCN	$J=4-3$	354.505	42.5	7.3	20	this work
H ¹³ CN	$J=1-0$	86.340	4.1	6.5	27	
HNC	$J=1-0$	90.664	4.4	5.6	33	
HC ₃ N	$J=10-9$	90.979	24.0	5.2	26	
HCN	$J=1-0$	88.632	4.3	6.4	50	Jones et al. (2012)
HCO ⁺	$J=1-0$	89.189	4.3	5.3	76	
N ₂ H ⁺	$J=1-0$	93.174	4.5	5.3	37	
H ¹³ CO ⁺	$J=1-0$	86.754	4.2	5.3	24	Tsuboi et al. (2015)
SiO	$J=2-1$	86.847	6.3	5.4	24	
¹³ CO	$J=2-1$	220.399	15.9	3.8	93	Ginsburg et al. (2016)
p -H ₂ CO	$3_{03}-2_{02}$	218.222	21.0	6.1	9	
	$3_{21}-2_{20}$	218.760	68.1	5.6	13	
CS	$J=1-0$	48.991	7.1	5.3	42	Tsuboi et al. (1999)

^a Taken from the from the Leiden Molecular and Atomic Database (Schöier et al. 2005).

^b Values at $T = 50$ K, calculated as $n_{\text{crit}} = A_{i,i-1} / \sum_{j<i} C_{i,j}$, where A and C denote the Einstein A coefficient and collision rate coefficient, respectively.

^c RMS noise level, measured in the data cube smoothed to a $60'' \times 60'' \times 10 \text{ km s}^{-1}$ resolution.

As the scale matrix Σ is a symmetric non-negative definite matrix by definition, we cannot apply flat priors independently for its elements. We adopt the separation strategy proposed by [Barnard et al. \(2000\)](#), which decomposes Σ into the product of the prior correlation coefficient matrix $R = \{R_{i,j}\}$ and scaling diagonal matrix $S = \{S_i \cdot \delta_{i,j}\}$:

$$\Sigma = \begin{pmatrix} S_1 & & & 0 \\ & S_2 & & \\ & & \ddots & \\ 0 & & & S_{N_p} \end{pmatrix} \cdot \begin{pmatrix} 1 & R_{1,2} & \dots & R_{1,N_p} \\ R_{1,2} & 1 & \dots & R_{2,N_p} \\ \vdots & \vdots & \ddots & \vdots \\ R_{1,N_p} & R_{2,N_p} & \dots & 1 \end{pmatrix} \cdot \begin{pmatrix} S_1 & & & 0 \\ & S_2 & & \\ & & \ddots & \\ 0 & & & S_{N_p} \end{pmatrix}. \quad (9)$$

Independent hyperpriors are assumed for R and S :

$$P(\Sigma) = |S|^{-N_p} \cdot P(S) \cdot P(R), \quad (10)$$

where

$$P(R) = \begin{cases} |R|^{-(N_p+1)} \cdot \prod_k^{N_p} \left[(R^{-1}_{k,k})^{-\frac{N}{2}} \right] & (\text{for } |R| > 0) \\ 0 & (\text{otherwise}) \end{cases} \quad (11)$$

$$P(S) = 1. \quad (12)$$

$R^{-1}_{k,k}$ denotes the diagonal elements of the inverse matrix of R . The factor $|S|^{-N_p}$ in Equation (10) originates from the Jacobian for variable conversion (Equation 9); this factor does not appear if we adopt R and S as hyperparameters instead of Σ . This PDF provides a flat distribution for each element of S_k and R_{k_1,k_2} over infinite and $[-1, 1]$ ranges, respectively.

A flat hyperprior is assumed for the central value vector \mathbf{p}_0 :

$$P(\mathbf{p}_0) = 1. \quad (13)$$

4.4. Additional Hyperpriors

In addition to the hyperpriors described in the above subsections (Equations 7 and 10–13), we introduce additional hyperpriors for a few individual elements of R and S to explicitly prohibit unphysical behavior of the parameter \mathbf{p} .

Table 2. Model Parameters

name	description
Local Parameters	
\mathbf{p}_i	logarithms of the parameters at the i^{th} voxel
$\log_{10} \frac{dN_{\text{H}_2}}{dv} / \text{cm}^{-2} (\text{km s}^{-1})^{-1}$	hydrogen column density per unit velocity
$\log_{10} n_{\text{H}_2} / \text{cm}^{-3}$	hydrogen volume density
$\log_{10} T_{\text{kin}} / \text{K}$	gas kinetic temperature
$\log_{10} R_{13}$	¹² C/ ¹³ C isotopic abundance
$\log_{10} \phi$	parameter defining the beam filling factor Φ ($\Phi \equiv 1 - e^{-\phi}$)
$\log_{10} x_{\text{mol}}(\text{HCN})$	fractional abundances
$\log_{10} x_{\text{mol}}(\text{HCO}^+)$	
$\log_{10} x_{\text{mol}}(\text{HNC})$	
$\log_{10} x_{\text{mol}}(\text{HC}_3\text{N})$	
$\log_{10} x_{\text{mol}}(\text{p-H}_2\text{CO})$	
$\log_{10} x_{\text{mol}}(\text{CS})$	
$\log_{10} x_{\text{mol}}(\text{SiO})$	
$\log_{10} x_{\text{mol}}(\text{N}_2\text{H}^+)$	
$\epsilon_{i,j}$	multiplicative error of the j^{th} line at the i^{th} voxel
Hyper-parameters	
\mathbf{p}_0	central value of the multivariate Student prior for \mathbf{p}
Σ	scale matrix of the multivariate Student prior for \mathbf{p}
σ_j	standard deviation of the log-lormal prior $\epsilon_{i,j}$
Constants	
$\nu = 2$	scale parameter of the Student prior for \mathbf{p}
$x_{\text{mol}}(^{12}\text{CO}) = 10^{-4}$	fractional abundance of ¹² CO
$\sigma_{\text{min}} = 0.1$	minimum σ
$S_{\text{max},R_{13}} = 0.03$	maximum $S_{R_{13}}$
$w_j = \begin{cases} 1 \\ 0.1 \end{cases}$	weight of HCN, HCO ⁺ , H ₂ CO, and ¹³ C isotopomeric lines weight of the other lines

Prior Correlation Coefficient between N_{H_2} and n_{H_2} —As mentioned in Subsection 4.2, the degeneracy between N_{H_2} and n_{H_2} in the non-LTE excitation equations often creates an unphysical anticorrelation. To prevent this artifact, we introduce a logistic hyperprior for $R_{N_{\text{H}_2}, n_{\text{H}_2}}$:

$$P(R_{N_{\text{H}_2}, n_{\text{H}_2}}) = \frac{1}{1 + \exp(-a \cdot R_{N_{\text{H}_2}, n_{\text{H}_2}})}, \quad (14)$$

which constrains $R_{N_{\text{H}_2}, n_{\text{H}_2}}$ to be non-negative.

Prior Correlation Coefficient between N_{H_2} and ϕ —Similarly, the severe degeneracy between N_{H_2} and ϕ may create an artificial anticorrelation between them, although it is reasonably assumed that voxels containing high-density regions are more likely to have higher volume filling factors, and hence higher beam-filling factors. Therefore, we impose a logistic hyperprior on $R_{N_{\text{H}_2}, \phi}$:

$$P(R_{N_{\text{H}_2}, \phi}) = \frac{1}{1 + \exp(-a \cdot R_{N_{\text{H}_2}, \phi})}. \quad (15)$$

Prior Scaling Factor for R_{13} —Riquelme et al. (2013) measured that the variation of R_{13} in the inner 100-pc region is relatively small, approximately within a factor of 2. Therefore, we limit the variable range of R_{13} by imposing a logistic hyperprior on $S_{R_{13}}$:

$$P(S_{R_{13}}) = \frac{1}{1 + \exp[a \cdot (S_{R_{13}} - S_{\text{max},R_{13}})]}. \quad (16)$$

We fix the upper limit value $S_{\max, R_{13}} = 0.03$ for this analysis; this corresponds to a relative variation of 30% (5th–95th percentile) from the central value for the Student function with $\nu = 2$. By limiting the variation of R_{13} to this reasonably small value, we are able to prevent the variation of R_{13} from creating an artificial correlation among R_{13} , $x_{\text{mol}}(\text{HCN})$, and $x_{\text{mol}}(\text{HCO}^+)$; as these abundances are determined primarily by the intensities of the ^{13}C isotopologue lines, they are scaled by R_{13} .

In total, the final prior $P(\mathbf{p}, \boldsymbol{\epsilon} | \boldsymbol{\theta})$ and hyperprior $P(\boldsymbol{\theta})$ are given by the product of the functions for the individual parameters and hyperparameters:

$$P(\mathbf{p}, \boldsymbol{\epsilon} | \boldsymbol{\theta}) = P(\mathbf{p} | \mathbf{p}_0, \boldsymbol{\Sigma}) \cdot P(\boldsymbol{\epsilon} | \boldsymbol{\sigma}) \quad (17)$$

$$P(\boldsymbol{\theta}) = P(\mathbf{p}_0) \cdot P(\boldsymbol{\Sigma}) \cdot P(\boldsymbol{\sigma}) \cdot P(R_{N_{\text{H}_2}, n_{\text{H}_2}}) \cdot P(R_{N_{\text{H}_2}, \phi}) \cdot P(S_{R_{13}}). \quad (18)$$

Then, the posterior function $P(\mathbf{p}, \boldsymbol{\epsilon}, \boldsymbol{\theta} | \mathbf{I})$ is obtained by multiplying Equations 2, 6–8, 10, and 13–16.

4.5. Numerical Solution Using the Markov-chain Monte Carlo Method

The posterior function $P(\mathbf{p}, \boldsymbol{\epsilon}, \boldsymbol{\theta} | \mathbf{I})$ is numerically calculated using the Markov-chain Monte Carlo (MCMC) method. For the parameter vectors \mathbf{p} and $\boldsymbol{\epsilon}$, the hybrid Monte Carlo (HM) method (Duane et al. 1987) is employed to simultaneously sample all of their elements at each voxel. The HM method is used also for the hyperparameter \mathbf{p}_0 . The random-walk Metropolis–Hastings (MH) algorithm is adopted for the R component of the hyperparameter $\boldsymbol{\Sigma}$, where the Wishart proposal function is used to draw the proposal value, $\boldsymbol{\Sigma}^{(K+1)}$, from the current value of $\boldsymbol{\Sigma}^{(k)}$ at the K^{th} step:

$$P(\boldsymbol{\Sigma}^{(K+1)} | \boldsymbol{\Sigma}^{(K)}) = |\boldsymbol{\Sigma}^{(K+1)}|^{\frac{b-N_p-1}{2}} \cdot |\boldsymbol{\Sigma}|^{-\frac{N_p}{2}} \cdot \exp \left[-\text{tr} \left(\frac{\boldsymbol{\Sigma}^{(K)-1} \cdot \boldsymbol{\Sigma}^{(K+1)}}{2} \right) \right], \quad (19)$$

so that $\boldsymbol{\Sigma}$ performs a random walk while remaining symmetric positive definite. The shape parameter b is manually adjusted so that the acceptance rate is not too high or low. The S component of $\boldsymbol{\Sigma}$ is sampled using the HM method. The random-walk MH algorithm with the Gaussian proposal function is used for the hyperparameter $\boldsymbol{\sigma}$.

The model intensities, $F(\mathbf{p})$, are calculated by solving the equilibrium between radiative transitions and the collisional excitation and de-excitation by molecular hydrogen. The photon-trapping effect and cosmic microwave background are considered using the LVG approximation. The transition rates are taken from the Leiden Atomic and Molecular Database (LAMDA; Schöier et al. 2005). We neglect the radiative excitation and infrared pumping by local continuum sources for simplicity, as they are insignificant compared with collisional excitation for most of our data. The exceptions are positions near the cluster-forming regions in the Sgr A and Sgr B2 complexes, for which our estimates are likely to include large errors.

We ignore the hyperfine splitting of the HCN $J=1-0$ and N_2H^+ $J=1-0$ transitions since the absorption among the hyperfine components cannot be precisely treated with the scheme of the LVG approximation for the CMZ, where the intrinsic line width is greater than the width of the hyperfine splitting. This simplification may introduce a large uncertainty in the HCN $J=1-0$ transition, which is generally optically thick.

4.6. Nonhierarchical Analysis

We perform another Bayesian analysis using a simpler nonhierarchical prior function for the purpose of comparison with the HB analysis. In this analysis, the original form of the likelihood function (Equation 1) without $\boldsymbol{\epsilon}$ is adopted. A rectangular prior PDF is assumed to constrain \mathbf{p} within reasonable ranges:

$$P(\mathbf{p}) = \prod_{i,j} H(p_{i,j} - p_{\min,j}) \cdot H(p_{\max,j} - p_{i,j}) \quad (20)$$

using the step function $H(x)$. The parameter ranges, $p_{\min, \max}$, are fixed at the values given in Table 3. The final nonhierarchical posterior function is given as

$$P(\mathbf{p} | \mathbf{I}) = \frac{P(\mathbf{I} | \mathbf{p}) \cdot P(\mathbf{p})}{P(\mathbf{I})}. \quad (21)$$

This nonhierarchical analysis is equivalent to the ML method with a finite parameter range, as the expression of the posterior function $P(\mathbf{p} | \mathbf{I})$ is identical to the likelihood function $P(\mathbf{I} | \mathbf{p})$, except for the normalization constant, as long as \mathbf{p} remains within the range defined by the prior function.

Table 3. Parameter Ranges Applied in the Nonhierarchical Method

parameter	p_{\min}	p_{\max}
$\log_{10} \frac{dN_{\text{H}_2}}{dv} / \text{cm}^{-2}(\text{km s}^{-1})^{-1}$	20	24
$\log_{10} n_{\text{H}_2}/\text{cm}^{-3}$	2	5
$\log_{10} T_{\text{kin}}/\text{K}$	1	3
$\log_{10} R_{13}$	1.2	1.6
$\log_{10} \phi$	-2	1
$\log_{10} x_{\text{mol}}(\cdot)$	-9	-6

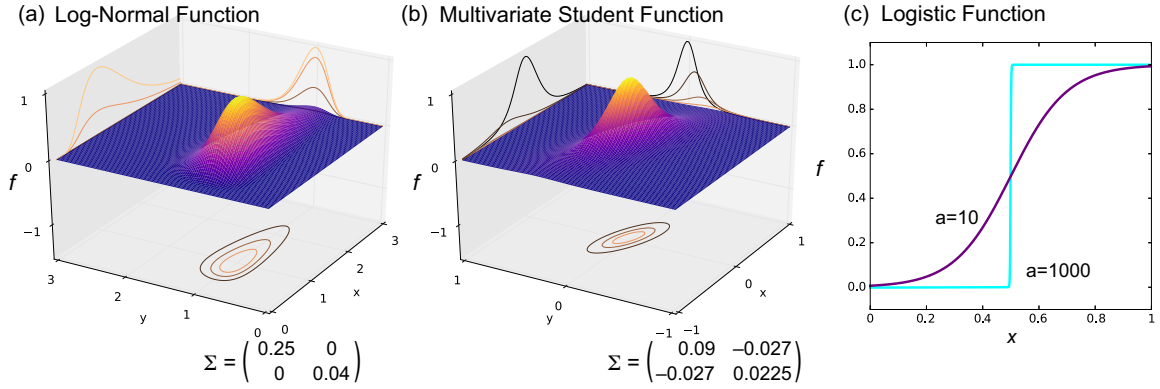


Figure 11. Examples of the functions used for the prior and hyperprior PDFs: (a) Two-dimensional log-normal function $f(x, y) = \exp[-\frac{1}{2} \cdot {}^t \mathbf{x} \cdot \Sigma^{-1} \cdot \mathbf{x}]$, (b) multivariate two-dimensional Student function $f(x, y) = [1 + \frac{1}{\nu} \cdot {}^t \mathbf{x} \cdot \Sigma^{-1} \cdot \mathbf{x}]^{-\frac{\nu+2}{2}}$ with $\nu = 2$, and (c) logistic function $f(x) = \frac{1}{1 + \exp[-a \cdot (x - x_0)]}$ with $x_0 = 0.5$. Contours are drawn at every 0.25.

4.7. Input Data and Weights

The data from the 3-mm-band Mopra 22-m telescope survey are given in the scale of T_{A}^* the in the literature (Jones et al. 2012). We applied a scale factor of 2.65 for the Mopra data so that the HNC, HC_3N and H^{13}CN intensities included in the Mopra survey data become consistent with T_{MB} of the same lines in our NRO 45-m data; the factor of 2.65 is consistent with the main-beam efficiency of the Mopra 22-m telescope, 0.4–0.5 (Ladd et al. 2005; Jones et al. 2012). The differences between the spatial resolutions in the data obtained from five different instruments are corrected by resampling the images to a grid spacing of $30'' \times 30'' \times 10 \text{ km s}^{-1}$ with a resolution of $60'' \times 60'' \times 10 \text{ km s}^{-1}$. The $60''$ angular size translates into a linear size of 2.4 pc at the distance of the Galactic Center. The Sgr D region ($l > 1^\circ$) is not used owing to the lack of H^{13}CO^+ data in this region. The velocity ranges for the foreground spiral arm regions are manually filtered to prevent deep self-absorption dips in the HCN, HCO^+ , and HNC lines in the arms. We approximate the RMS noise levels, δ , to be spatially uniform and measure them using the emission-less regions of the smoothed maps. The measured values of δ are given in Table 1.

The input data are classified into two categories; the first comprises the lines from the molecules that have multiple transitions in our dataset (HCN, HCO^+ , $p\text{-H}_2\text{CO}$, and their ^{13}C isotopologues), which are necessary to determine the physical conditions, R_{13} , and ϕ , while the second comprises molecules with single transitions, which are required only for calculating x_{mol} . We apply a $3\text{-}\sigma$ threshold for the first group lines; as a result of this filtering, almost the entire part of the CND and 180-pc ring are excluded from the analysis. We apply different weights (w_j in Equations 1 and 2) for these two groups; $w_j = 1$ for the first group, and $w_j = 0.1$ for the second group. This ensures that the physical condition parameters are determined primarily by the intensity ratios among the first group lines. The effect of these weights on the final results are discussed in a later section (§6.1).

As mentioned earlier, the ^{13}CO $J=2-1$ data (Ginsburg et al. 2016) are used to trace the hydrogen column densities by assuming a constant fractional abundance of 10^{-4} for ^{12}CO . The assumption of constant ^{12}CO abundance may not be true, particularly for the Sgr A complex where a considerably high atomic carbon (C^0)-to- ^{12}CO abundance ratio of ~ 1 is reported (Tanaka et al. 2011). In addition, the low critical density of the line ($6 \times 10^3 \text{ cm}^{-3}$) may violate the

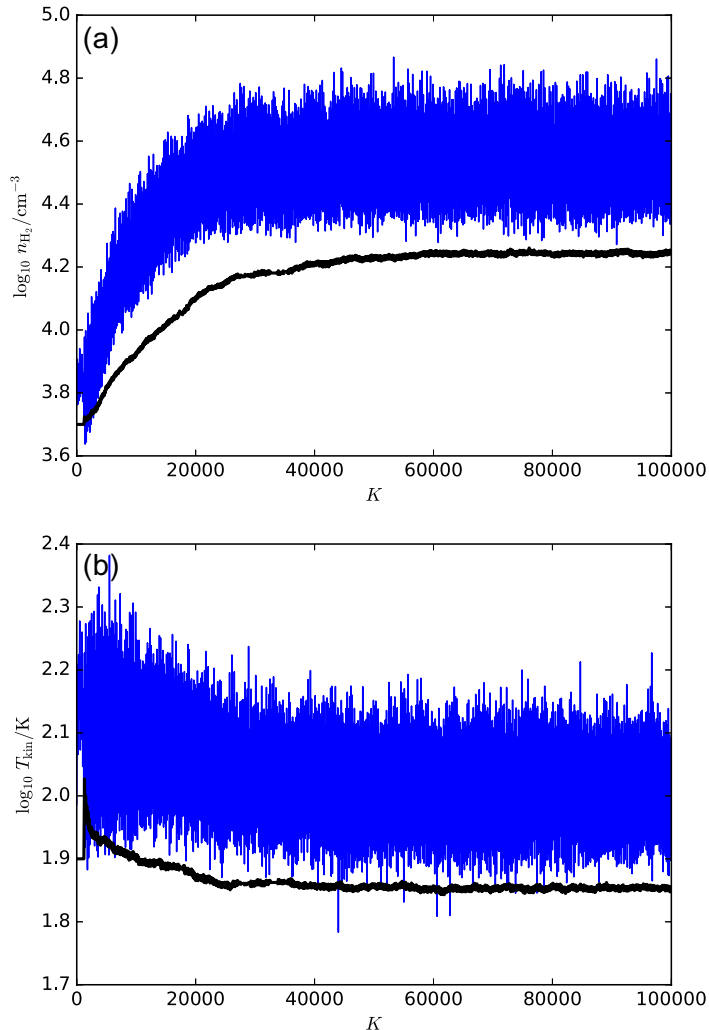


Figure 12. Trace plots of n_{H_2} and T_{kin} in the HB analysis (panels a and b, respectively) against the MCMC step K . The blue and black lines denote the plots for the local parameter \mathbf{p} at the center position of the 50-km s^{-1} cloud and for the hyperparameter \mathbf{p}_0 , respectively. We kept \mathbf{p}_0 constant and the step sizes small until $K=1000$ in this MCMC run.

one-zone assumption, which states that all lines originate from the same volume. This effect is not negligible, as we will show in Subsection 6.2. Nevertheless, the impact of this effect on our analysis is limited, as these uncertainties only affect the ^{12}CO fractional abundance; changes in the ^{13}CO $J=2-1$ intensity or $x_{\text{mol}}(^{12}\text{CO})$ would systematically increase or decrease the fractional abundances of the other molecules, but T_{kin} , n_{H_2} , and the relative abundances among the molecules except for ^{12}CO are almost unaffected.

5. PHYSICAL CONDITIONS AND MOLECULAR ABUNDANCES: RESULTS

5.1. Raw MCMC Results

For the HB analysis, we repeated several MCMC runs starting from different sets of initial parameters. Figure 12 shows the trace plot of the hyperparameters $p_{0,T_{\text{kin}}}$ and $p_{0,n_{\text{H}_2}}$, along with that of the local parameters T_{kin} and n_{H_2} at the center position of the 50-km s^{-1} cloud, for one MCMC run. For both of the hyperparameters and the local parameters, n_{H_2} and T_{kin} exhibit steady increasing and decreasing trends, respectively, until convergence has been reached at $K \sim 60000$; these burn-in steps will be discarded when calculating the posterior and marginal posterior distributions. We confirmed that the converged values of the hyperparameters and local parameters were consistent among the different MCMC runs.

Figure 13a shows the trace plot of the local parameters in the $n_{\text{H}_2}-T_{\text{kin}}$ plane. The steps $K = 70000-71000$ are highlighted in the figure (red lines) to exemplify that the autocorrelation and correlation among the parameters are insignificant so that the parameter space is sampled sufficiently randomly. Frequency histograms of the parameters

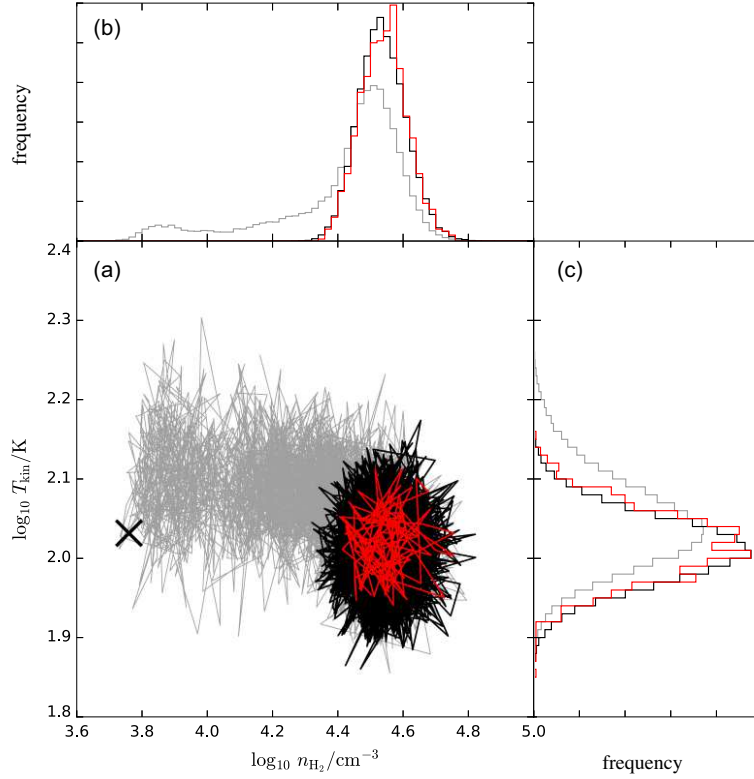


Figure 13. (a) Trace plot of $(n_{\text{H}_2}, T_{\text{kin}})$ at the center position of the 50-km s⁻¹ cloud for the HB analysis on the two-dimensional plane at every 10 MCMC steps. The gray and black lines are for the burn-in steps ($K < 60000$) and the steps after convergence ($K > 60000$), respectively. The initial parameter is indicated by the cross mark. The plot points for $K = 70000-71000$ are highlighted in red, showing that the parameter space is sampled sufficiently randomly within this short interval. (b) and (c) Frequency histograms of n_{H_2} and T_{kin} , respectively. The gray, black, and red lines correspond to the plot points with the respective colors in panel (a).

are shown in panels b and c. The partial frequency distributions for $K = 70000-71000$ are consistent with the entire distributions for $K > 60000$; this confirms that the MCMC run converged after $K = 60000$ and that the parameter space is fully covered by this MCMC run.

5.2. Maps

After discarding the early burn-in steps before reaching convergence, the marginal posterior is calculated for each parameter at each voxel:

$$P(p_{i,j}|\mathbf{I}) = \int P(\mathbf{p}, \boldsymbol{\epsilon}, \boldsymbol{\theta}|\mathbf{I}) \cdot \left(\prod_{k \neq i, l \neq j} dp_{k,l} \right) \cdot d\boldsymbol{\epsilon} \cdot d\boldsymbol{\theta} \quad (22)$$

from the frequency distribution of the parameter of interest in the MCMC-sampled variables. The 3-D maps of the i^{th} parameter and its uncertainty are constructed from the median, $p_{i,j}$ and 25th–75th-percentile interval, $\Delta(p_{i,j})$, of their marginal posteriors. For each parameter, the voxels with uncertainties greater than 0.2 are discarded from the final map; as the parameter \mathbf{p} is defined as a base-10 logarithm, the uncertainty of 0.2 translates into to a $\pm 29\%$ relative uncertainty in the linear scale.

Figure 14 shows the frequency histograms for the PDF-median values of N_{H_2} (per 10-km s⁻¹ velocity interval), n_{H_2} , T_{kin} , R_{13} , and $\Phi = 1 - e^{-\phi}$, which are obtained using the HB and nonhierarchical analyses. In addition to them, the histogram of the beam-averaged column density $\langle N_{\text{H}_2} \rangle \equiv \Phi \cdot N_{\text{H}_2}$ is also presented. Through the HB analysis, T_{kin} was derived to be 10^{1.5} K to 10^{2.5} K, with the most frequent value being 10^{1.8} K. This result is consistent with the non-LTE analysis of the same p -H₂CO data assuming constant n_{H_2} (Ginsburg et al. 2016), as expected from the weak n_{H_2} dependence of their intensity ratio. The values of n_{H_2} are in a range of 10^{3.5}–10⁵ cm⁻³ with the highest frequency at 10^{4.2} cm⁻³, which is consistent with the previous non-LTE analysis performed using tracers of a similar

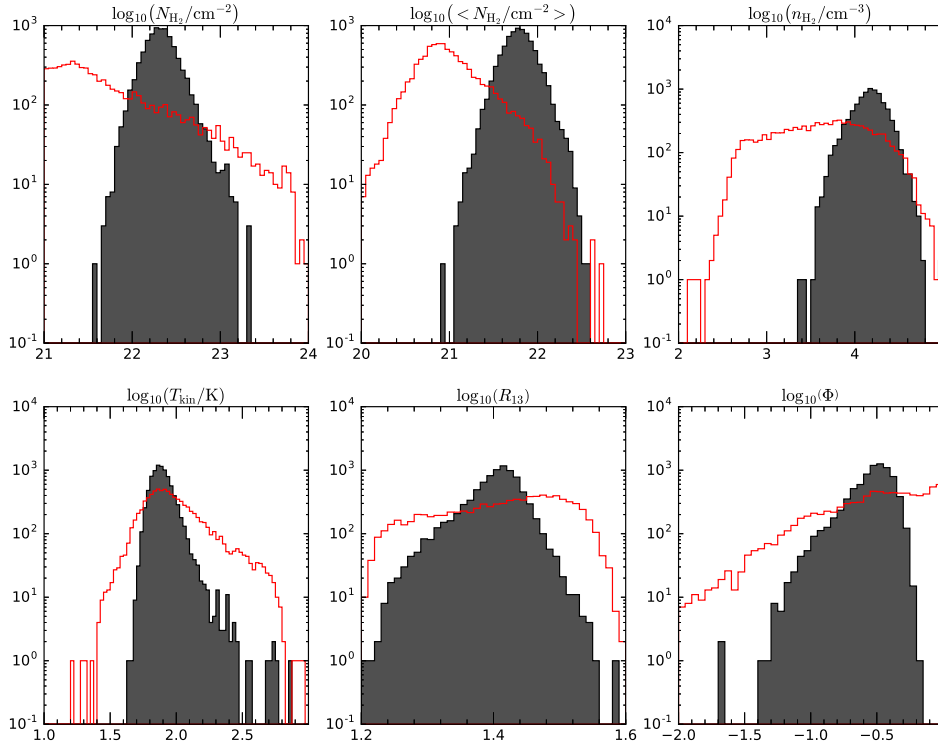


Figure 14. Frequency histograms of the median values of the hydrogen column density (N_{H_2}), beam-averaged N_{H_2} ($\langle N_{\text{H}_2} \rangle$), hydrogen volume density (n_{H_2}), gas kinetic temperature (T_{kin}), C/ ^{13}C isotopic abundance ratio (R_{13}), and beam filling factor (Φ) for the HB analysis (gray filled histograms) and the nonhierarchical analysis (red open histograms).

n_{crit} range ($\sim 10^5 \text{ cm}^{-3}$; Tsuboi & Tadaki 2011; Tsuboi et al. 2015), while being approximately an order of magnitude higher than the analysis by Nagai et al. (2007) using low- J CO transitions. The median R_{13} is 25, which is in a good agreement with the canonical value for the CMZ, i.e., 24, measured through $^{12}\text{C}^{18}\text{O}$ and $^{13}\text{C}^{18}\text{O}$ observations (Lis & Goldsmith 1989, 1990).

Figure 15a shows the scatter plots and 2-D frequency histograms of n_{H_2} versus N_{H_2} (per 10-km s^{-1} bin), T_{kin} , and R_{13} . The posterior correlation coefficients, $r_{i_1, i_2} = \frac{t_{\mathbf{p}_{i_1}, t_{\mathbf{p}_{i_2}}}}{|\mathbf{p}_{i_1}| \cdot |\mathbf{p}_{i_2}|}$, are shown in the figure. Through the HB analysis, a small but significant positive correlation was obtained between n_{H_2} and N_{H_2} , whose correlation coefficient is 0.11 ± 0.01 . The correlation coefficient is slightly negative for the $n_{\text{H}_2} - T_{\text{kin}}$ plot, but this is mostly due to the outlying points with $T_{\text{kin}} > 10^{2.5} \text{ K}$ and $n_{\text{H}_2} < 10^4 \text{ cm}^{-3}$, which correspond to the Sgr B2 cluster-forming region. No noticeable correlation is present in the main component.

5.3. Comparison with the Nonhierarchical Method

A comparison of the results obtained with the nonhierarchical and HB methods is shown in Figures 14 and 15. Figure 14b shows that the histograms for the nonhierarchical analysis have broader profiles than those for the HB analysis for all of the six parameters displayed in the figure. The difference from the HB analysis is most remarkable for N_{H_2} and Φ ; their frequency distributions for the nonhierarchical analyses are spread over almost the full variable ranges and truncated at the boundary values imposed by the rectangular priors. In particular, the histogram of Φ has a frequency peak at the upper limit value, i.e., 1. This indicates that the nonhierarchical analysis failed to determine the optimal parameter set that maximizes $P(\mathbf{I}|\mathbf{p})$ in a physically reasonable range for considerable fractions of the voxels. Meanwhile, the frequency profile of T_{kin} does not differ greatly between the HB and nonhierarchical analysis, except that the width of the histogram in the latter is approximately twice that in the former. This reflects that T_{kin} is primarily determined by the intensity ratio between the two H_2CO lines and is relatively insensitive to other conditions.

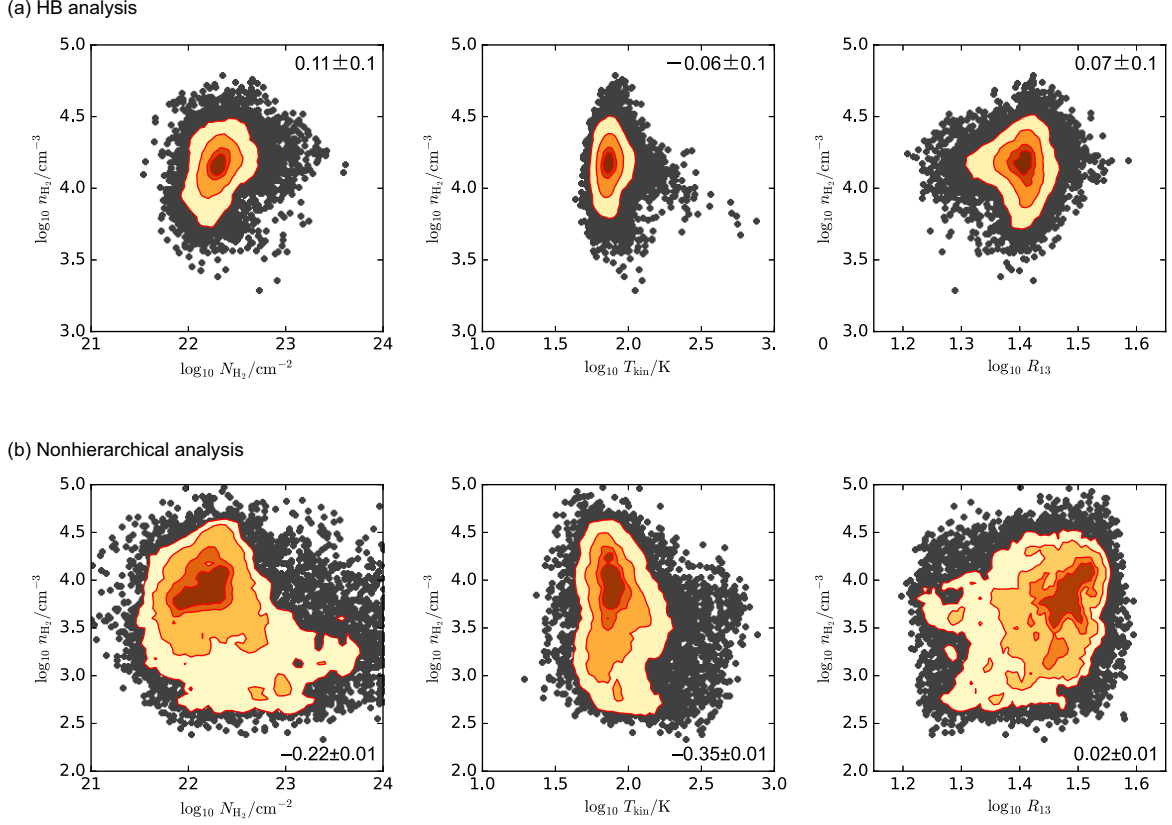


Figure 15. (a) Scatter plots of n_{H_2} versus N_{H_2} per 10-km s⁻¹ velocity bin, T_{kin} , and R_{13} from left to right for the results of the HB analysis. The overlaid colored contours show the 2-D frequency histograms drawn at the 10th–90th, 25th–75th, 40th–60th, and 45th–55th-percentile intervals. The medians and the 50th-percentile credible intervals of the correlation coefficients are shown on the panels. (b) Same as (a) but for the nonhierarchical analysis.

Figure 15b shows scatter plots and 2-D histograms of n_{H_2} versus N_{H_2} (per 10-km s⁻¹ bin), T_{kin} , and R_{13} for the nonhierarchical analysis. The N_{H_2} – n_{H_2} plot exhibits a weak anticorrelation, whose correlation coefficient is $r_{N_{\text{H}_2}, n_{\text{H}_2}} = -0.22 \pm 0.01$; as mentioned earlier (§4.2), this anticorrelation is likely to be unphysical. The plot also indicates that the data points within the 40th–60th-percentile interval of the 2-D histogram show a positive correlation, and their parameter range is approximately consistent with the result of the HB analysis. The unphysical anticorrelation is created by the tail extending to the high- N_{H_2} and low- n_{H_2} region in the 2-D histogram.

On the basis of the above comparison, we conclude that the results of the nonhierarchical analysis are less reliable than those of the HB analysis; although the nonhierarchical analysis was successful in measuring T_{kin} and n_{H_2} in high-density regions, approximately 80% of the total number of voxels are severely affected by the artificial correlation created through the analysis. Conversely, the HB analysis successfully suppressed these unphysical behaviors of the physical condition parameters without introducing complicated physical modeling.

5.4. Validity of the HB Analysis

The posterior distribution of ϵ , which represents the multiplicative systematic errors in the measured line intensities, is determined simultaneously with that for \mathbf{p} . The parameter ϵ provides a measure of the discrepancy in the calculated line intensities from the observed intensities; thus, they can be used for checking the validity of the HB analysis. Table 4 summarizes the medians and the 25th–75th-percentile intervals of the voxel values of ϵ . The HB analysis could be judged to be successful as a whole; the errors are less than $\sim 20\%$ for all of the lines, which would be sufficiently small to be interpreted as calibration errors or minor deviations from the ideal model. The relatively large dispersions in ϵ for HCN $J=1-0$ and HCO⁺ $J=1-0$ are presumably because these lines are closely related to the inference of the parameter R_{13} (see Figure 7) and hence are strongly affected by the hyperprior $P(S_{R_{13}})$ that suppresses the variation in R_{13} . In conclusion, the HB analysis was able to determine the parameters that consistently explain the observed line intensities without introducing large systematic errors in addition to the measured random noise.

Table 4. Systematic Multiplicative Errors

molecule	transition	ϵ
HCN	$J=1-0$	$0.97^{+0.11}_{-0.11}$
	$J=4-3$	$1.00^{+0.06}_{-0.07}$
H^{13}CN	$J=1-0$	$1.01^{+0.04}_{-0.04}$
HCO^+	$J=1-0$	$1.13^{+0.22}_{-0.23}$
H^{13}CO^+	$J=1-0$	$0.98^{+0.05}_{-0.05}$
$p\text{-H}_2\text{CO}$	$3_{03}-2_{02}$	$1.00^{+0.06}_{-0.07}$
	$3_{21}-2_{20}$	$1.00^{+0.02}_{-0.02}$
^{13}CO	$J=2-1$	$1.00^{+0.03}_{-0.03}$
HNC	$J=1-0$	$1.00^{+0.03}_{-0.04}$
HC_3N	$J=10-9$	$1.00^{+0.02}_{-0.02}$
SiO	$J=2-1$	$1.00^{+0.02}_{-0.02}$
N_2H^+	$J=1-0$	$1.00^{+0.02}_{-0.03}$
CS	$J=1-0$	$1.00^{+0.03}_{-0.02}$

We note that the median values of ϵ close to unity do not indicate that the intensity calibration is accurate, but instead they are simply the immediate consequences of the log-normal prior distribution assumed for ϵ (Equation 6), in which the mean value is fixed at 1. Therefore, our analysis is not specifically designed to measure the calibration accuracy; ϵ is a nuisance parameter introduced for convenience of calculation, which is to be integrated out in the final step of the analysis. The prior for ϵ is given so that $\epsilon = 1$ if a parameter set that simultaneously reproduces all of the observed intensities exists, even when I systematically includes large calibration errors. This explains the reason for the small dispersions in ϵ for the lines of HNC, HC_3N , SiO, N_2H^+ , and CS (the second group lines defined in §4.7); as these molecules have only one transition in the dataset, their intensities can be always fitted by modifying the abundances regardless of the other parameters. The inclusion of new parameters or hyperparameters might enable us to measure the systematic calibration offsets among different observations, but such an analysis would require an extended dataset.

5.5. Spatial Variations in the Physical Condition Parameters and ^{13}C Isotopic Abundance

Figure 16 presents the 2-D distributions of $\langle N_{\text{H}_2} \rangle$, T_{kin} , n_{H_2} , and R_{13} projected onto the l - b plane. The $\langle N_{\text{H}_2} \rangle$ map shows the velocity-integrated values, and the others show the averages weighted by $\langle N_{\text{H}_2} \rangle$ along the v_{LSR} axis. Their l - v_{LSR} diagrams are shown in Figure 17. The averages along the b axis are shown for $\langle N_{\text{H}_2} \rangle$, and the highest values along the b axis at each l - v_{LSR} coordinate are plotted for the other three parameters.

The n_{H_2} map shows the physically natural outward decreasing gradients for the majority of the molecular clouds. The high n_{H_2} regions are evenly distributed across the CMZ, and no systematic difference in n_{H_2} is observed between the regions that host active SF regions or young massive clusters (Sgr A, Sgr B, and M0.11–0.08) and other inactive clouds; the peak n_{H_2} values in the active SF regions are $10^{4.6}$ – $10^{4.8}$ cm^{-3} , which is not particularly high compared with the peak densities of quiescent dense gas clumps such as the Brick cloud and cloud d in the dust-ridge region.

The spatial variation in T_{kin} approximately follows the intensity variation in the HCN $J=4-3$ and HC_3N $J=10-9$ lines. It has a clear peak toward the Sgr B2 cluster-forming region, though the value of $10^{2.8}$ K is unreliable because the intense continuum is not considered in our model. Similarly, the increase in T_{kin} toward the Galactic Center ($l \sim -0^\circ.08$) and the center of the 50- km s^{-1} cloud (M–0.02–0.07; $l \sim -0^\circ.02$) are considered to be a result of UV heating by the central cluster and H II region G–0.02–0.07, respectively. However, the correlation between the high-temperature regions and SF regions is weak almost everywhere else in the maps. The high-temperature spots in the Brick cloud, the N3 clump, the polar arc, CO.02, CO–0.30, and the southeastern extension of the Sgr B2 complex lack known corresponding UV-heating sources, which would support the idea of mechanical heating by dissipating shocks (Ao et al. 2013; Ginsburg et al. 2016).

A few of the temperature peaks without UV sources are associated with broad-velocity features or expanding shells. Two clumps, i.e., CO.02 and CO–0.30, are high-velocity(-width) compact clouds with atypical broad velocity widths of $\gtrsim 50$ km s^{-1} at full width zero intensity (Oka et al. 2012; Tanaka et al. 2015). The temperatures of both clumps are significantly higher than that of their surroundings. Tanaka et al. (2015) detected spots of high-excitation thermal methanol lines with $E_{\text{u}}/k_{\text{B}} \gtrsim 100$ K inside CO–0.30 through interferometric observations, which is consistent with

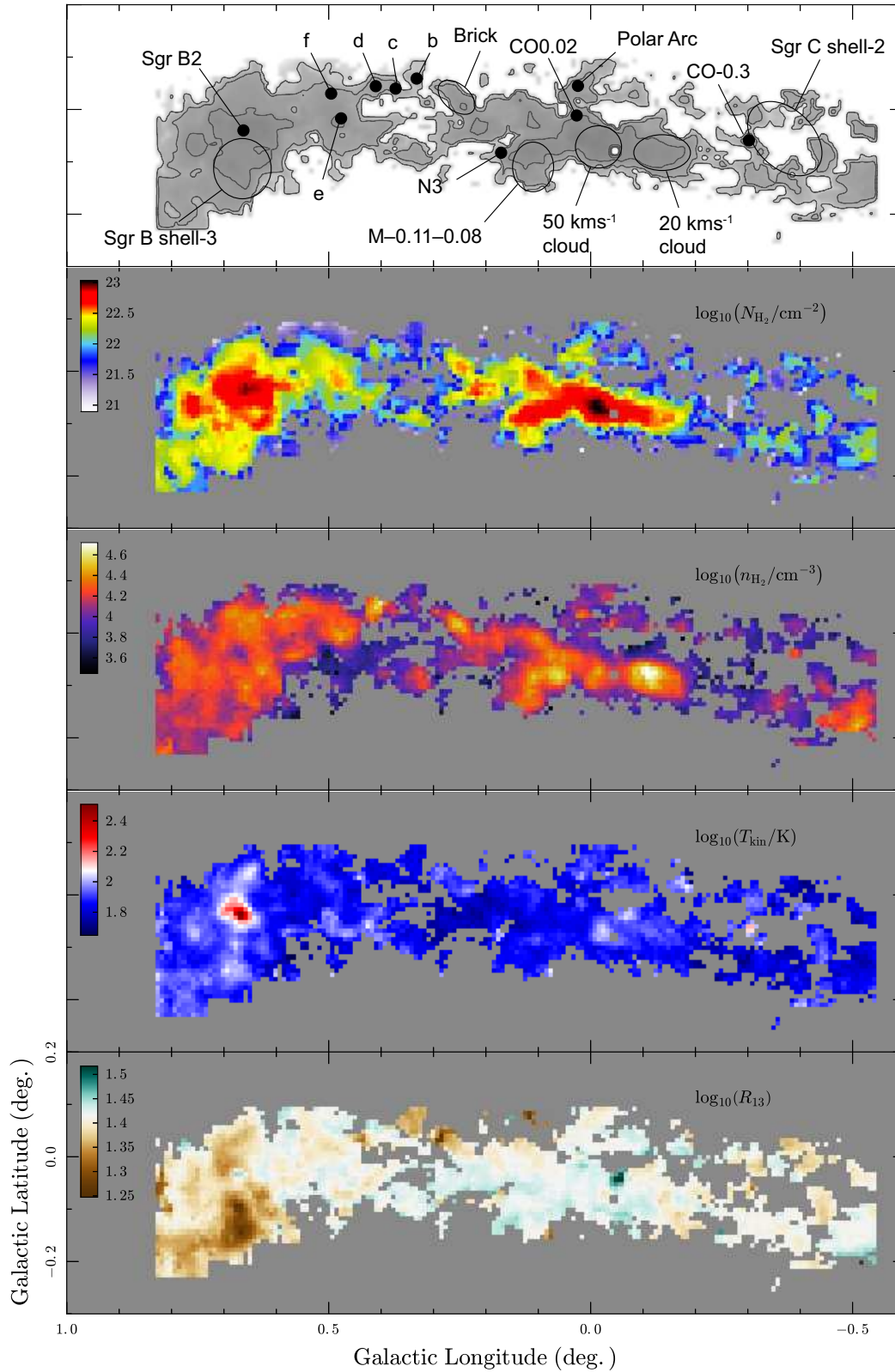


Figure 16. Results of the HB analysis for the beam-averaged hydrogen column density ($\langle N_{\text{H}_2} \rangle$), hydrogen volume density (n_{H_2}), gas kinetic temperature (T_{kin}), and $^{12}\text{C}/^{13}\text{C}$ isotopic ratio (R_{13}) in the projection onto the l - b plane. The $\langle N_{\text{H}_2} \rangle$ map shows the velocity-integrated values, and the others show the average weighted by $\langle N_{\text{H}_2} \rangle$ along the v_{LSR} axis.

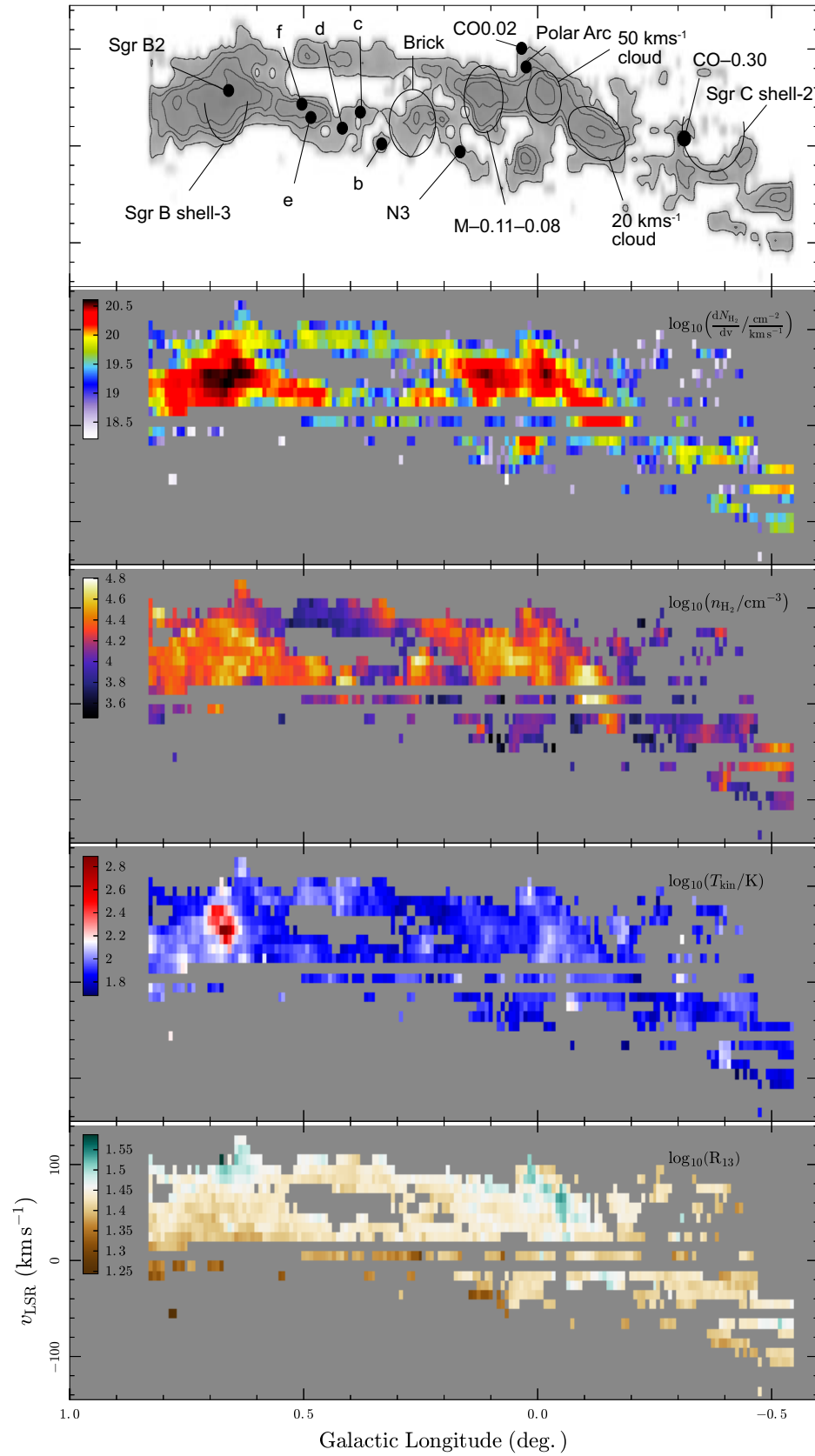


Figure 17. Same as Figure 16 but in the projection onto the l - v_{LSR} plane. The $\langle N_{\text{H}_2} \rangle$ map shows the averages in the b direction, and the others show the highest value along the b axis at each l - v_{LSR} coordinate.

the high temperature measured in our analysis. Two molecular shells, i.e., Sgr C shell 2 (Tanaka et al. 2014) and Sgr B shell 3 (Tsuboi et al. 2015) exhibit T_{kin} higher than 100 K in our map.

The variation in R_{13} is small compared with the variations in n_{H_2} or T_{kin} ; it is almost constant across the region with a slight increasing gradient toward the Galactic Center. This is due to the hyperprior $P(S_{R_{13}})$ that explicitly imposes an upper limit on the dispersion of R_{13} . The 180-pc ring region, for which high values of R_{13} are reported by Riquelme et al. (2013), is not included in our analysis. There is a subtle local spatial correlation between R_{13} and N_{H_2} in the Sgr A and Sgr B2 complexes, although the global correlation coefficient is slightly negative, -0.1 . If the local positive correlation between N_{H_2} and R_{13} is real, it is consistent with selective photodissociation, which predicts that ^{12}CO is more stable against photodissociation than ^{13}CO in high-column-density regions. However, the significance of the correlation would require further careful investigation; it could be an artifact introduced by an insufficient correction for the opacity effect for the main HCO^+ isotopologue line.

The $l-v_{\text{LSR}}$ plot for R_{13} presented in Figure 17 indicates the effect of contamination by the spiral arms on the analysis. The velocity channels at $v_{\text{LSR}} = -30 \text{ km s}^{-1}$, -10 km s^{-1} , and 10 km s^{-1} have larger fractions of low R_{13} values than the other channels. This can be explained by the self-absorption of HCN $J=1-0$ and HCO^+ $J=1-0$ by the foreground low-density material; as their ^{13}C isotopologue lines are less affected by self-absorption, R_{13} is underestimated when contamination by the spiral arms is significant. Although the obvious absorption dips at the velocities of the spiral arms have been removed in the initial filtering (§4.7), these results indicate that the velocity channels contiguous to the arms are also affected by self-absorption. Therefore, we exclude these velocity channels from the analysis in the following sections.

5.6. Molecular Abundances

Figure 18 shows the molecular abundance maps projected onto the $l-b$ plane, where projection is performed by taking $\langle N_{\text{H}_2} \rangle$ -weighted averages of the parameters. A trend common to several molecular species can be identified; that is, the abundances of SiO , HC_3N , H_2CO , CS , and N_2H^+ are enhanced over a wide area of the Sgr B2 complex. This enhancement is not limited to the Sgr B2 cluster-forming region but also extends to the southeast extension, where active star formation is absent. The other three species, i.e., HCN , HNC , and HCO^+ , do not exhibit enhancement in the Sgr B2 region; in particular, the latter two species have almost flat spatial distributions over the entire map.

Figure 19 shows the posterior correlation coefficient matrix for the logarithms of T_{kin} , n_{H_2} , and the molecular abundances. The species that have high abundances in the Sgr B2 complex have large positive correlation coefficients with each other. In addition, HC_3N and H_2CO exhibit strong positive correlations with T_{kin} . The correlation coefficients with n_{H_2} are negative or zero for all molecules except for N_2H^+ , which may imply that our analysis is affected by the degeneracy between n_{H_2} and $x_{\text{mol}}(\cdot)$ despite the use of the HB method. Nevertheless, it is not likely that the negative correlation coefficients between the molecular abundances and n_{H_2} are purely artificial, as the strength of the (anti-)correlation is not correlated with n_{crit} of the transitions used in the analysis. For example, HCO^+ and HCN have the largest and the second largest negative correlations with n_{H_2} , respectively, but these species have the highest and lowest critical densities in our dataset. The critical density of HCO^+ $J=1-0$ is similar to that of N_2H^+ $J=1-0$, which is the only species with a positive correlation with n_{H_2} .

5.7. X -factor and $X/\frac{dv}{dr}$

It is useful to obtain good gas mass tracer lines that are insensitive to the physical and chemical environments and to define their luminosity-to-mass conversion factors (X -factors). In addition to the evident good tracer, i.e., ^{13}CO , we calculate the conversion factors for HCO^+ , H^{13}CO^+ , and HNC , whose abundances show small spatial variations and weak dependencies on the physical conditions. Figure 20a shows the voxel-by-voxel scatter plots of the observed HCO^+ , H^{13}CO^+ , and HNC intensities against the values of $\langle N_{\text{H}_2} \rangle$ calculated using the HB analysis, with colors according to the ranges of n_{H_2} . The overlaid lines represent the medians and 2.5th–97.5th-percentile intervals of the X -factors weighted by the intensities. The X -factors are consistent across the CMZ within an order of magnitude for all four analyzed lines. The systematic variation over different n_{H_2} ranges is approximately a factor of 4 from the lowest-density range ($\sim 10^3 \text{ cm}^{-3}$) to the highest-density range ($\sim 10^{4.4} \text{ cm}^{-3}$) for H^{13}CO^+ and HNC . HCO^+ is less dependent on n_{H_2} because the n_{H_2} dependencies of abundance and emissivity cancel each other.

We repeat the same analysis with the dust-based column densities instead of using the values of $\langle N_{\text{H}_2} \rangle$ from the HB analysis results for the purpose of checking consistency. These dust-based X -factors are equivalent to the intensity-to-dense-gas-mass conversion factors derived by Mills & Battersby (2017). We calculate the column density from the *Herschel* 500- μm data (Molinari et al. 2011) smoothed with a $60''$ Gaussian kernel assuming a constant dust temperature of 20 K. For the dust emissivity per unit gas mass, the formula in Pierce-Price et al. (2000), $\kappa_\nu = 2.5 \times 10^{-4} \left(\frac{\lambda}{1 \text{ mm}}\right)^{-\beta} \text{ cm}^2 \text{ g}^{-1}$, is adopted. The dust emissivity index β is assumed to be 2. Figure 20b shows the scatter plots of the dust-based column densities against the velocity-integrated line intensities. Linearity with the

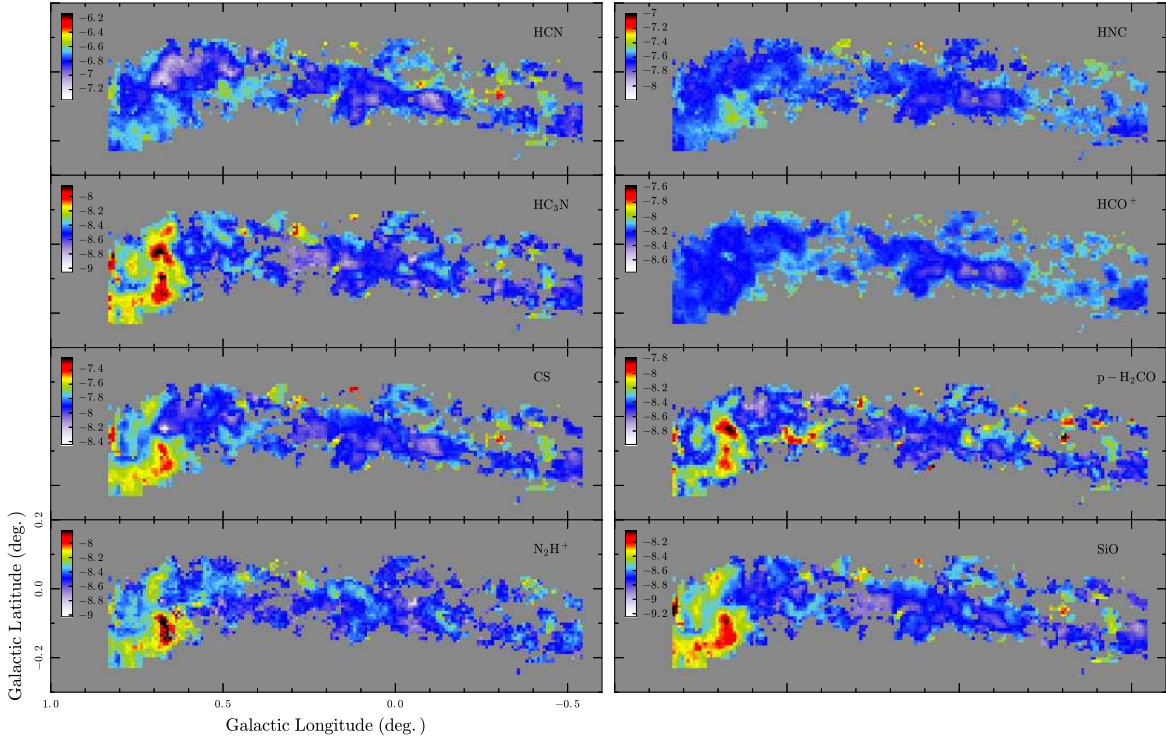


Figure 18. Maps of the molecular fractional abundances calculated using the HB analysis. The abundances are averaged over the full velocity range and weighted with $\langle N_{\text{H}_2} \rangle$ for each line-of-sight.

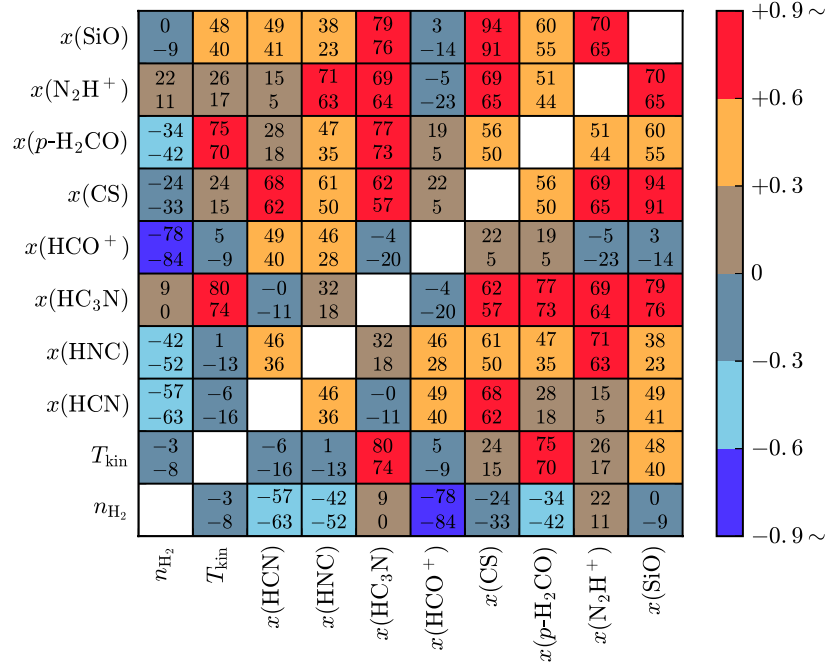


Figure 19. Posterior correlation coefficient matrix of the logarithms of the physical condition parameters and molecular abundances. The numbers in each cell show the 25th–75th-percentile intervals multiplied by 100. The cells are colored according to the medians.

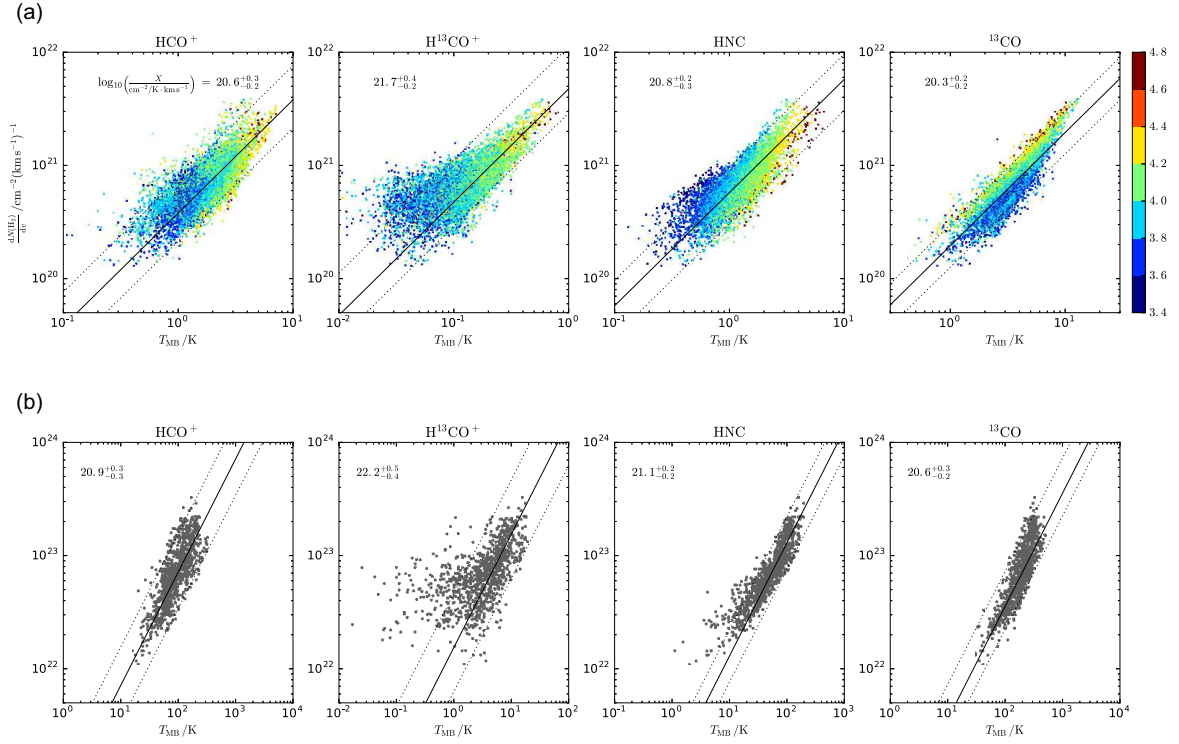


Figure 20. (a) Voxel-by-voxel scatter plots of the column densities (per unit velocity), which are calculated using the HB analysis, against the brightness temperatures of HCO^+ $J=1-0$, $H^{13}CO^+$ $J=1-0$, HNC $J=1-0$, and ^{13}CO $J=2-1$, with colors according to the density at each voxel. (b) Same as (a) but with velocity-integrated column densities estimated from the 500- μm dust flux and the line integrated intensities.

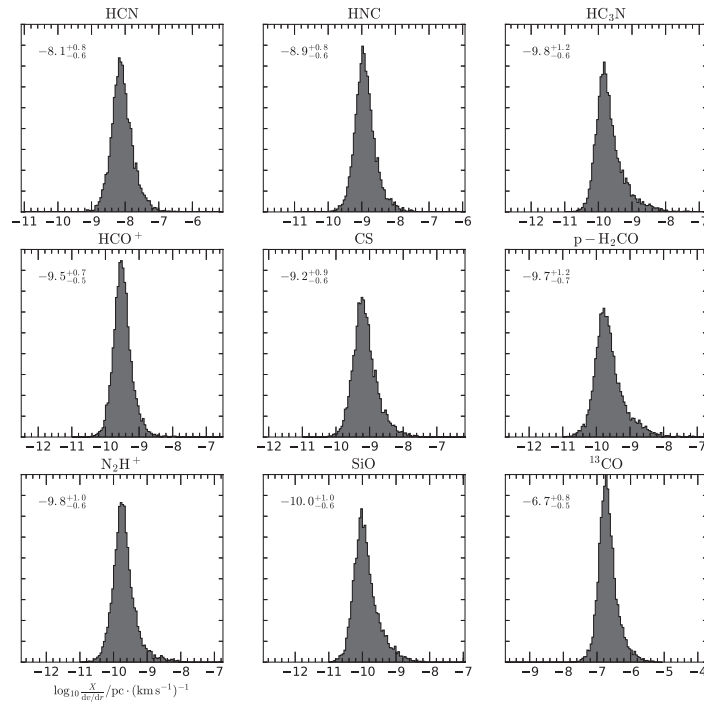


Figure 21. Frequency histograms of the $X/\frac{dV}{d\tau}$ values for various molecules. The frequencies are weighted by $\langle N_{H_2} \rangle$. The median and 2.5th-97.5th-percentile interval are displayed on each panel.

dust-based column densities holds for the HCO⁺, HNC, and ¹³CO data, while H¹³CO⁺ appears more susceptible to instrumental noise owing to its weak intensities. The dust-based scaling factors are systematically higher by a factor of 10^{0.3}–10^{0.5} than those determined using the HB analysis. This difference is reasonable, considering the crudeness of the assumption for the dust temperature and emissivity and the omission of the contribution from low-density gas in the HB analysis (see Subsection 6.2).

We evaluate the $X/\frac{dv}{dr}$ parameter, i.e., the scaling factor that relates n_{H_2} to the column densities per unit velocity. Figure 21 shows the frequency histograms of $X/\frac{dv}{dr} \equiv x_{\text{mol}}(\cdot) \frac{dN_{\text{H}_2}}{dv}/n_{\text{H}_2}$ weighted by $\langle N_{\text{H}_2} \rangle$, which are calculated from the results of the HB analysis. The 2.5th–97.5th -percentile intervals of the parameter are less than two orders of magnitude for all analyzed molecules. HNC, HCO⁺, and HCN exhibit the smallest dispersions in the values of $X/\frac{dv}{dr}$ among the analyzed molecules (except for ¹³CO), which indicates their efficacy as physical condition probes.

6. DISCUSSION

6.1. Limitations of the HB Analysis

The HB analysis successfully suppressed the artificial features that appeared in the results of the ML analysis and provided a more feasible 3-D distribution of the physical/chemical parameters. In this section, we summarize the limitations of our analysis, which potentially affect the validity of the results.

Prior and Hyperprior Functions—First, the HB analysis is clearly dependent on the arbitrarily selected prior functions for the parameters and the systematic errors. We selected neutral priors, i.e., multivariate log-Student and log-normal functions, but the assumption of unimodal prior PDFs does not have observational or theoretical grounds except for n_{H_2} and N_{H_2} . Considering the chemical and physical diversity among CMZ clouds, multimodal PDFs might be more realistic, even though they could materially complicate the model. In addition, the observation field selected for the analysis could alter the results; if we extract images of a certain region from the full CMZ map, the statistical properties of this subset could be different from those of the full dataset, which may lead to different values for the prior probability.

Different Source Sizes and Velocity Widths for Different Lines—Although our analysis assumes the same source sizes (or beam filling factors) and velocity widths for all lines, this assumption is generally not true; optically thin lines that trace high-temperature/density regions (such as the H¹³CN and H₂CO lines) are likely to have compact spatial distributions and narrow spectral profiles compared with other lines and hence are likely to occupy a smaller volume in the position–position–velocity (PPV) space. In other words, the grid size of our analysis (2.4 pc × 2.4 pc × 10 km s^{−1}) may not be sufficiently small to allow the one-zone approximation within PPV volume elements. This breakdown in the one-zone approximation can significantly affect the physical condition measurements. An example of this situation might be observed for cloud CO−0.30, in which interferometric observations identified a few warm methanol spots inside a dense clump of HCN $J=3-2$ of approximately 1 pc in diameter (Tanaka et al. 2015). If the H₂CO lines originate from the warm methanol spots, T_{kin} probed by the H₂CO lines overestimates the temperature from the representative value for the volume element. The overestimation of T_{kin} leads to underestimation of n_{H_2} , as shown in Figure 8. Indeed, our analysis gives an unlikely low n_{H_2} of $\sim 10^{3.5}$ cm^{−3} at the voxels of CO−0.30, which does not agree with the presence of the intense N₂H⁺ $J=3-2$ emission (Tanaka et al. 2015), whose n_{crit} is $> 10^6$ cm^{−3}. This underestimation of n_{H_2} might not be an exceptional case, considering the numerous class-I methanol sources found in the CMZ (Yusef-Zadeh et al. 2013).

H¹³CN Depletion—Another important factor that is neglected in our ideal model is the isotopic fractionation in C-bearing species; even though we assume a common value of R_{13} for HCN and HCO⁺, theoretical works show that the [HCN]/[H¹³CN] abundance ratio is significantly higher than the [C]/[¹³C] isotopic ratio in the chemical steady state, while the [H¹³CO⁺]/[HCO⁺] ratio is only slightly lower than it (Roueff et al. 2015). If isotopic fractionation is considered, it should affect the estimates of T_{kin} and n_{H_2} , on which the HCN $J=4-3$ /H¹³CN $J=1-0$ and HCN $J=1-0$ /H¹³CN $J=1-0$ ratios are dependent. By performing tests with the manually given H¹³CN depletion factor, we find that a depletion factor of 5 for H¹³CN causes a decrease of ~ 0.2 and an ~ 0.1 increase in $\log_{10} n_{\text{H}_2}$ and $\log_{10} T$, respectively, in the HB analysis results.

Weights on the Observational Data—In the likelihood function (Equations 1 and 2), we assumed different statistical weights for the molecules having multiple transitions in the dataset and for those that do not (i.e., the first and second groups in §4.7, respectively), in addition to the weights given by the RMS noise. These additional weights were introduced for a purely computational purpose; without them, the latter group lines introduce a large amount of “noise” into the measurement of n_{H_2} since they effectively decrease the weight of the HCN $J=4-3$ data, which are the most reliable probe of n_{H_2} in our dataset. As an example, we show the n_{H_2} map obtained with the HB analysis assuming $w_j = 1$ for all lines in Figure 22. In this map, n_{H_2} exhibits an irregular distribution that is not correlated

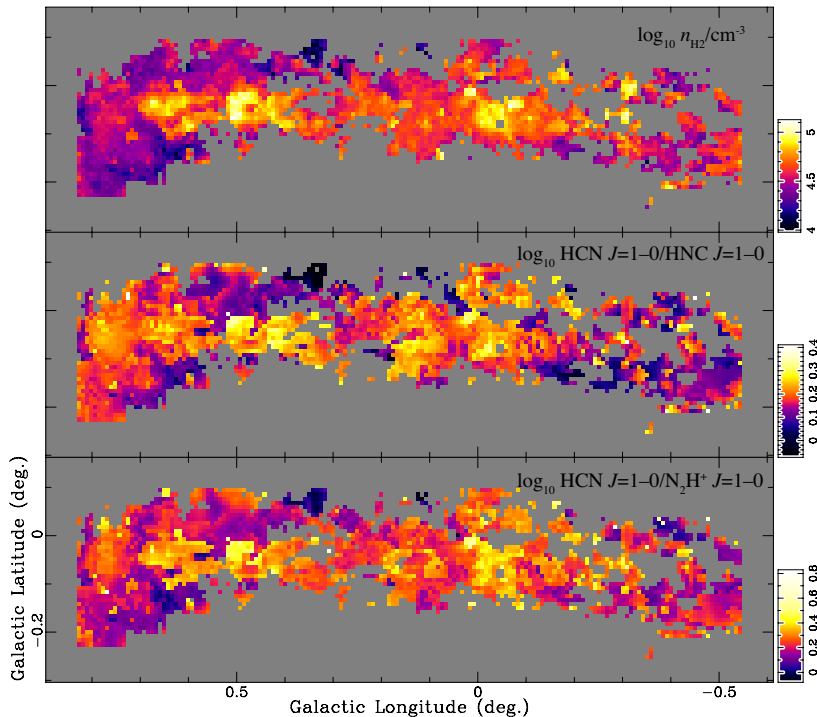


Figure 22. (top panel) Volume density (n_{H_2}) map obtained with the HB analysis where the weights of the input data w_j are assumed to be 1 for all lines. The highest values along the velocity axis are plotted on the l - b plane. Regions with irregularly high n_{H_2} are present along $l \sim 0.5^\circ$, -0.2° , and -0.3° . The correlation coefficient between n_{H_2} and N_{H_2} is -0.1 . (bottom and middle panels) The HCN $J=1-0$ /HNC $J=1-0$ and HCN $J=1-0$ / N_2H^+ $J=1-0$ maps, respectively. Their similarity to the n_{H_2} map indicates that n_{H_2} is determined primarily by these intensity ratios in this analysis.

with the N_{H_2} distribution, where n_{H_2} is determined primarily by the intensity ratios of HCN $J=1-0$ to HNC $J=1-0$ and N_2H^+ $J=1-0$. In the main analysis, we assumed that $w_j = 0.1$ for the lines that are not necessary for measuring the physical conditions; thus, we were able to suppress this unphysical behavior. However, this also means that our present HB framework failed to determine the appropriate values for the systematic errors ϵ that give a physically realistic solution without manually modifying the weights of the input data. This can introduce arbitrariness in the analysis since we do not have a precise method to determine the appropriate weights prior to obtaining the results of the analysis.

Multiphase Gas—Finally, a significant bias could be introduced by the high critical densities of the line used in our analysis if multiple density/temperature gas exists in the same beam. This issue is discussed in more detail in Subsection 6.2.

Among these issues, the arbitrariness of the choice of the prior function is the largest problem with our HB analysis. However, we consider that the prior used in the HB analysis is at least more plausible than the flat prior used in the nonhierarchical analysis (and hence than the standard ML analysis) since the anticorrelation between N_{H_2} and n_{H_2} in the latter analysis is unreasonable from a physical point of view. This indicates that the errors due to the deficiencies of the simple one-zone non-LTE calculation have to be considered in the parameter inference; however, the standard method is not able to handle this problem, as discussed in Subsection 4.2. An HB analysis with a log-normal or student prior is a method commonly used to solve such problems where the available information is limited without introducing too large biases.

6.2. Multiphase Gas in the CMZ

Our analysis assumes a single temperature and density component for individual voxels, and the deviation from the one-zone model is regarded as systematic errors that are included in the ϵ parameters. However, the presence of a multitemperature gas in the CMZ has been shown in several previous studies on the basis of the direct detection of the multicomponent ammonia rotation temperature (Huttemeister et al. 1993; Arai et al. 2016) and indirectly from the inconsistency among temperatures measured using different probes (e.g., Nagayama et al. 2007; Martin et al. 2004;

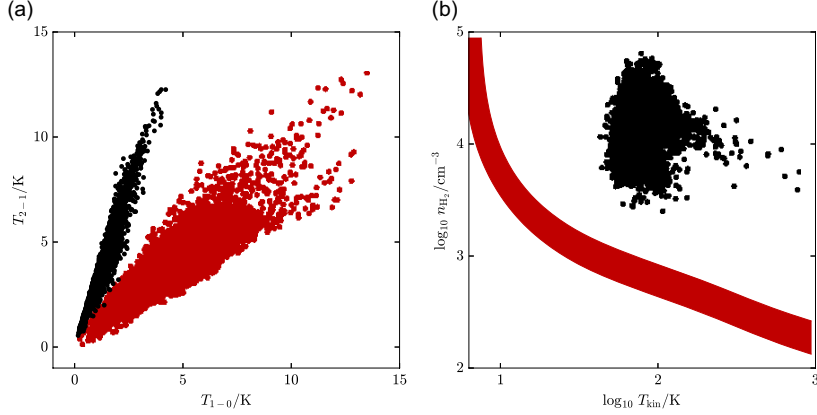


Figure 23. (a) Voxel-by-voxel $^{13}\text{CO } J=1-0 - J=2-1$ scatter plots from observations (red; Oka et al. 1999; Ginsburg et al. 2016) and for the values calculated using the parameters obtained through the HB analysis (black). (b) $T_{\text{kin}} - n_{\text{H}_2}$ scatter plot for the HB results (black points). The hatched region represents the parameter range corresponding to the 25th–75th-percentile interval of the observed $^{13}\text{CO } J=2-1/J=1-0$ intensity ratio.

Table 5. Cold-to-Warm Ratios for the Line Intensities and the Column Density

		$T_{\text{cold}}=40 \text{ K}$	20 K	10 K
		$n_{\text{cold}} = 10^{3.0} \text{ cm}^{-3}$	$10^{3.2} \text{ cm}^{-3}$	$10^{3.7} \text{ cm}^{-3}$
HCN	$J=1-0$	0.09	0.11	0.20
	$J=4-3$	0.01	0.006	0.003
H^{13}CN	$J=1-0$	0.05	0.05	0.10
HCO^+	$J=1-0$	0.09	0.10	0.21
H^{13}CO^+	$J=1-0$	0.09	0.07	0.18
$p\text{-H}_2\text{CO}$	$3_{03}-2_{02}$	0.06	0.07	0.18
	$3_{21}-2_{20}$	0.04	0.05	0.07
^{13}CO	$J=2-1$	0.52	0.51	0.50
HNC	$J=1-0$	0.08	0.10	0.24
HC_3N	$J=10-9$	0.02	0.02	0.02
SiO	$J=2-1$	0.04	0.05	0.14
N_2H^+	$J=1-0$	0.07	0.09	0.20
CS	$J=1-0$	0.11	0.13	0.31
N_{H_2}		0.84	0.88	1.2

Nagai et al. 2007; Ott et al. 2014; Ginsburg et al. 2016). The recent observations of multi- J ammonia inversion lines by Arai et al. (2016) show that the ammonia rotation diagrams at a few representative voxels in the CMZ maps have a significant excess at the (1,1) level from the curve with a rotation temperature of $\sim 100\text{--}200 \text{ K}$, which otherwise fits the transitions up to $J=6$. They estimate the typical temperature for the cold component to be 20 K and the column density to be comparable to that of the warm component.

The results of the HB analysis also indicate the presence of multicomponent gas; they are inconsistent with the observations of the $^{13}\text{CO } J=1-0$ line, which is not included in our dataset. Figure 23a compares the $^{13}\text{CO } J=1-0$ intensity calculated using the parameters derived through the HB analysis with the data taken using the NRO 45-m telescope (Oka et al. 1999). The calculated luminosity accounts for only $\sim 30\%$ of the total observed luminosity. Figure 23b shows the $T_{\text{kin}} - n_{\text{H}_2}$ parameter range calculated from the observed $^{13}\text{CO } J=2-1/J=1-0$ intensity ratio (0.88 ± 0.18) on the assumption of optically thin conditions. These values of T_{kin} and n_{H_2} differ from those obtained through the HB analysis by approximately an order of magnitude when one of these parameters is fixed. If the $^{13}\text{CO } J=1-0$ and $J=2-1$ emissions originate from the same cold gas with a temperature of 20 K that causes the (1,1) excess in the ammonia emissions (Arai et al. 2016), the best-fit value of n_{H_2} is obtained to be $10^{3.2} \text{ cm}^{-3}$. This is qualitatively consistent

with the simultaneous T_{kin} and n_{H_2} measurements performed by Nagai et al. (2007), who derived a combination of a low T_{kin} of ~ 40 K and a low n_{H_2} of $\sim 10^{3.5} \text{ cm}^{-3}$ from the $J=1-0$ and $J=3-2$ transitions of CO and ¹³CO. The actual density of the cold gas could be lower than $10^{3.2} \text{ cm}^{-3}$, considering the contribution from the warm gas to the ¹³CO $J=2-1$ luminosity. Thus, this cold gas component is likely to have a lower temperature and density than the values derived using the HB analysis.

We obtain an approximate estimate of the effect of the cold gas on our analysis using the above estimates. Table 5 summarizes the cold-to-warm ratios of the line intensities, defined as the ratios of the intensities calculated for the cold component to those for the warm component, i.e., the gas visible in the tracers used in our analysis. The intensities of the cold component are calculated on the bases of three assumptions for T_{kin} and n_{H_2} (T_{cold} , and n_{cold}), where the molecular fractional abundances are assumed to be the same as those obtained from the HB analysis. The intensities of the warm component are calculated directly from the median parameter values obtained using the HB analysis. The column density of the cold component is adjusted so that the cold-to-warm ratio of ¹³CO $J=1-0$ is 2 for each parameter set of T_{cold} and n_{cold} . The calculated cold-to-warm ratios of N_{H_2} are also presented in Table 5. The intensity ratios are $\lesssim 0.1$ for most of the lines when $T_{\text{cold}} > 20$ K, except for ¹³CO $J=2-1$. The ratios may even decrease if the positive correlations between T_{kin} and $x_{\text{mol}}(\cdot)$ determined using the HB analysis hold for the two temperature components. Therefore, it could be tentatively concluded that the effect of the multitemperature gas on the HB analysis is negligible in our HB analysis, and our results are safely biased to the warm-temperature component.

The multiphase gas could be more accurately modeled by using a multimodal prior instead of the unimodal prior used in this analysis. However, multiphase gas modeling would require correspondingly large datasets for the results to be significant; at least three transitions are necessary for each molecule, and their upper state energies and critical densities should cover a sufficiently wide range of physical conditions, i.e., typically $T_{\text{kin}} = 10-100$ K and $n_{\text{H}_2} = 10^{3-6} \text{ cm}^{-3}$. Such large datasets are not available yet but may be provided by future wide-field and broadband observations using ALMA and other instruments.

6.3. Principal Component Analysis

We apply principal component analysis (PCA) to the 3-D data of T_{kin} , n_{H} , and the molecular fractional abundances with a minor modification; we treat T_{kin} and n_{H_2} preferentially and subtract their covariant components from the molecular abundances in advance, thereby making the results easier to interpret than those of the analysis involving the full parameter space.

The parameters to be analyzed are represented by the matrix $Q \equiv (\mathbf{q}_T, \mathbf{q}_n, \mathbf{q}_{x_1}, \mathbf{q}_{x_2}, \dots, \mathbf{q}_{x_{N_{\text{mol}}}})$. The parameter vectors \mathbf{q}_i are defined as $\mathbf{p}_i - \langle p_{i,j} \rangle_j$, where the notation $\langle \cdot \rangle_j$ denotes the average for j , i.e., the spatial average. The subscripts T , n , and x_k are for T_{kin} , n_{H_2} , and the fractional abundances of the k^{th} species ($k=1,2, \dots, N_{\text{mol}}$), respectively.

First, we decompose Q into two components that are covariant and noncovariant with T_{kin} and n_{H_2} (Q_c and Q_{nc} , respectively):

$$Q = Q_c + Q_{\text{nc}}. \quad (23)$$

The condition ${}^t(\mathbf{q}_T, \mathbf{q}_n) \cdot Q_{\text{nc}} = 0$ gives that $Q_c = Q_{T,n} \cdot ({}^tQ_{T,n} \cdot Q_{T,n})^{-1} \cdot {}^tQ_{T,n} \cdot Q$, where $Q_{T,n} \equiv (\mathbf{q}_T, \mathbf{q}_n)$.

The component $Q_{\text{nc}} (= Q - Q_c)$ is further decomposed into the principal components \mathbf{w}_i :

$$Q_{\text{nc}} = (\mathbf{w}_1, \mathbf{w}_2, \dots, \mathbf{w}_{N_{\text{mol}}}) \cdot {}^tV, \quad (24)$$

where V is a matrix of the nonzero eigenvectors of ${}^tQ_{\text{nc}} \cdot Q_{\text{nc}}$, and $(\mathbf{w}_1, \mathbf{w}_2, \dots, \mathbf{w}_{N_{\text{mol}}}) \equiv Q_{\text{nc}} \cdot V$.

Thus, the parameter space has been decomposed into linear combinations of \mathbf{q}_T , \mathbf{q}_n , \mathbf{w}_1 , $\mathbf{w}_2, \dots, \mathbf{w}_{N_p}$. The original parameters are expressed using the coefficient vectors in the new basis ($x_T(X) \equiv {}^t\mathbf{q}_X \cdot \frac{\mathbf{q}_T}{|\mathbf{q}_T|}$ and so on). The total variance of all parameters, $\Lambda \equiv \text{tr}({}^tQ \cdot Q)$, is decomposed as

$$\begin{aligned} \Lambda &= \text{tr}({}^tQ_c \cdot Q_c) + \text{tr}({}^tQ_{\text{nc}} \cdot Q_{\text{nc}}) \\ &= \text{tr}({}^tQ_c \cdot Q_c) + \sum_{i=1,2,\dots,N_{\text{mol}}} \lambda_i, \end{aligned} \quad (25)$$

where λ_i denotes the non-zero eigenvalues of S corresponding to the i^{th} principal component (PC i) of Q_{nc} . The first term in Equation 25 is the contribution from Q_c , and the second is the sum of the variances of the PCs. The former cannot be decomposed further owing to the non-zero correlation between T_{kin} and n_{H} . We define the contribution

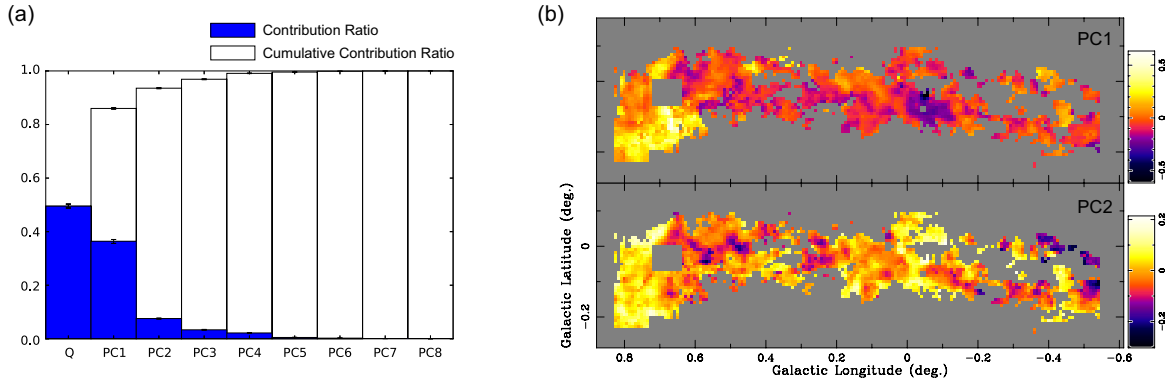


Figure 24. Results of the PCA with the molecular abundances. (a) Contribution ratios and cumulative contribution ratios with error bars for the 25th–75th-percentile intervals. (b) N_{H_2} -weighted average of the median values of PC1 and PC2 projected on the l - b plane. The $5' \times 5'$ square region toward the Sgr B2 cluster-forming region, the $30'' \times 30''$ region toward SgrA*, and the velocity channels of the spiral arms are not used for the PCA analysis, as the HB analysis is inaccurate for those regions owing to the omission of continuum emission in the excitation equations and self-absorption.

ratios as the ratios of each term to the total variance, i.e., $\text{tr}({}^tQ_c \cdot Q_c) / \Lambda$ for the Q_c component and λ_i / Λ for $\text{PC}i$, by extending the definition in the standard PCA.

The marginal posterior PDFs of the PCs and their contribution ratios are calculated by repeating the analysis for values at every MCMC step. The $5' \times 5'$ square region toward the Sgr B2 cluster-forming region, the $30'' \times 30''$ region toward SgrA*, and the velocity channels of the spiral arms are not used for the calculations since these regions show obvious artificial features in the maps of R_{13} and several molecular abundances, presumably due to the omission of the continuum in the excitation analysis and self-absorption (Subsections 5.5 and 5.6). The individual and cumulative contribution ratios are shown in Figure 24a. Q_c and the first PC explain more than 80% of the total variance, and the contribution ratio of PC1 is more than twice the sum over the remaining PCs. The cumulative contribution ratio up to PC2 is 93%. Thus, we are able to reduce the original 10 variables into the 4-D space defined by T_{kin} , n_{H_2} , PC1, and PC2 without losing important information.

Figure 24b shows the 2-D maps of PC1 and PC2 averaged along the velocity axis, weighted by N_{H_2} . Both PC1 and PC2 represent the enhancement in multiple molecules in the Sgr B2 complex (Figure 18). These two PCs also show large positive values in the southwestern rim of Sgr C shell-1 ($l \sim -0.45^\circ$). The difference between the two PCs appears most clearly in the 50-km s⁻¹ cloud ($l \sim 0^\circ$), where PC1 is negative but PC2 is positive. In addition to these regions, PC2 has relatively large positive values in the polar arc and M0.11–0.08.

The coefficient vector representations of the molecules in the x_T - x_n - x_1 - x_2 space are shown in Figure 25. On the x_T - x_n plane, we observe approximately the same trend as that found in the correlation coefficient matrix (Figure 19); HC_3N and H_2CO are distinguished by their large positive x_T , and N_2H^+ is the only molecule that has a significantly positive x_n . The difference among the molecules becomes evident in their behaviors on the x_T - x_1 and x_T - x_2 planes. Two groups are identified in the x_T - x_1 plot, i.e., species with both large x_T and x_1 (CS , SiO , HC_3N , H_2CO , and N_2H^+) and those with both small x_T and x_1 (HCN , HNC , and HCO^+); they correspond to the groups classified according to whether they are enhanced in the Sgr B2 complex or not, which are immediately identified in the molecular abundance maps (Figure 18). The latter group is further classified into two subgroups according to the x_2 values; SiO and CS have both large positive x_1 and x_2 , whereas HC_3N , H_2CO , and N_2H^+ have zero or negative x_2 values.

6.3.1. PC1 and PC2: Regions with Fast Shocks

SiO and CS are distinguished from other species by their large positive x_1 and x_2 values. PC1 and PC2 constitute approximately 80% of the total variance of their abundance. As SiO is a well-proven tracer of fast shocks, PC1 and PC2 are likely to be related to regions with shock velocities $\gtrsim 20$ km s⁻¹, where the sputtering of dust silicate cores occurs. High CS abundances are also observed in the fast-velocity regions in molecular outflow sources (Jorgensen et al. 2004; Tafalla et al. 2010). In addition, the large x_T values for SiO and CS corroborate the interpretation that they represent shocked regions.

However, the interpretation of PC1 is somewhat ambiguous since a large value of x_1 is also measured for N_2H^+ . The molecule is an established tracer of cold quiescent gas, as it is destroyed in shocked gas via the reaction with molecules desorbed from dust. Hence, the apparent spatial correlation between N_2H^+ and SiO in our data is unlikely to indicate the similarity between their chemical characteristics; it is more likely that our analysis is not sufficiently precise to

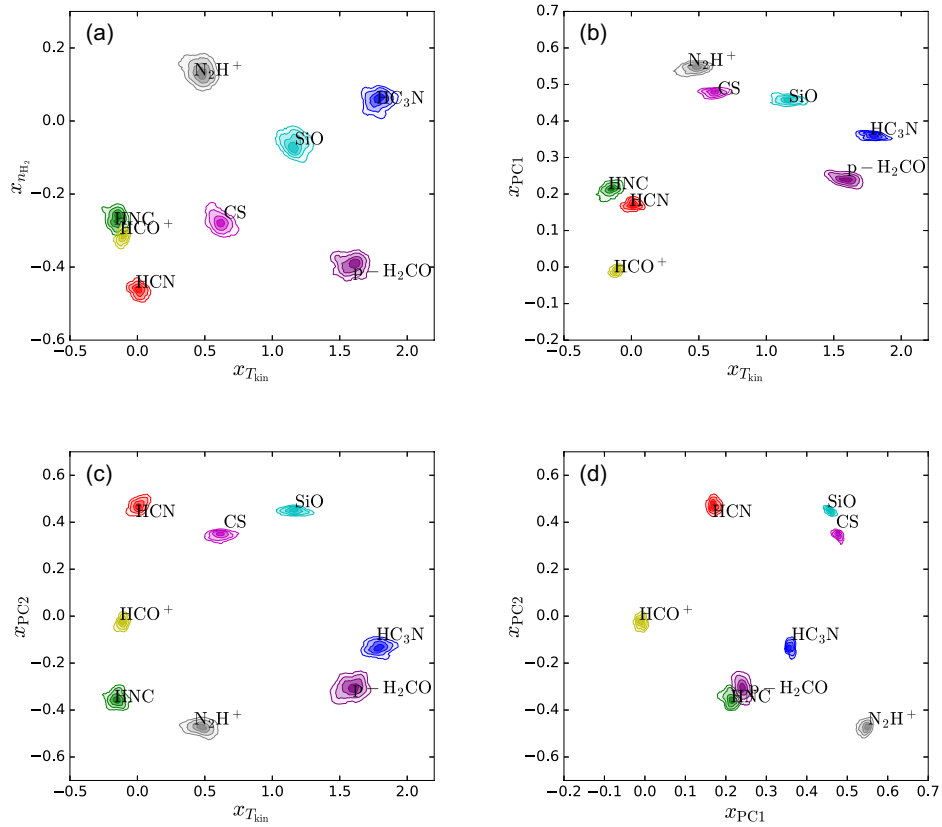


Figure 25. Coefficient vector representation of the molecular abundances on the $x_{T_{\text{kin}}}-x_{n_{\text{H}_2}}$ (panel a), $x_{T_{\text{kin}}}-x_{\text{PC1}}$ (panel b), $x_{T_{\text{kin}}}-x_{\text{PC2}}$ (panel c), and $x_{\text{PC1}}-x_{\text{PC2}}$ (panel d) planes. Contours are drawn at the 2.5th-97.5th-, 10th-80th-, 25th-75th-, 40th-50th-percentile intervals of the marginal posterior distribution of each parameter pair.

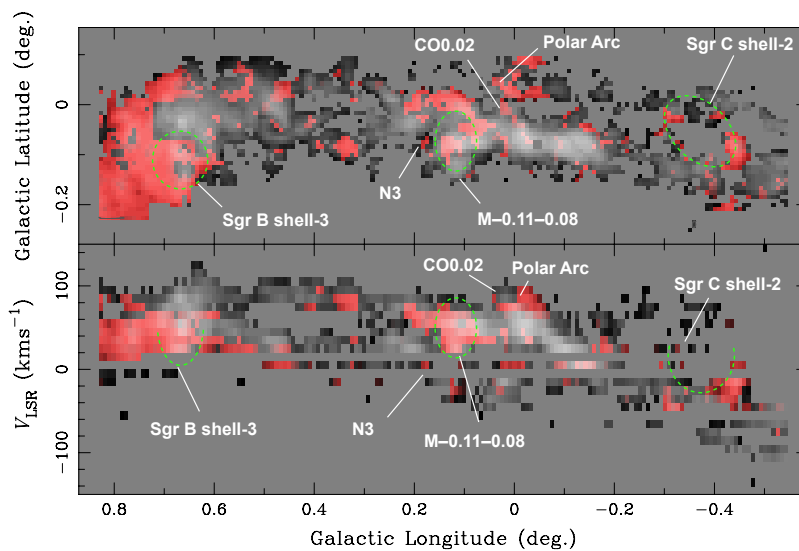


Figure 26. $\langle N_{\text{H}_2} \rangle$ map projected on the $l-b$ and $l-v_{\text{LSR}}$ planes (top and bottom panels, respectively), where the highest values along the projection axes are plotted. The regions with positive PC1 and PC2 are highlighted in red.

separate the N_2H^+ -rich preshock gas from the post-shock turbulent gas, which frequently coexist in single-dish beams (e.g., Tanaka et al. 2015). Moreover, PC1 may contain an artificial correlation created by the uncertainty in N_{H_2} due to the neglect of the spatial variation in x_{mol} (CO) and the contribution from the low-density component discussed in Subsection 6.2.

Therefore, PC2 may better represent the fast-shock regions than PC1; the molecules with large positive x_2 (HCN, CS, and SiO) and those with large negative x_2 (N_2H^+ and HNC) correspond well with the species enhanced in fast-shock regions and those abundant in cold quiescent gas, respectively (Hirota et al. 1998; Tafalla et al. 2010). Therefore, we could translate the combination of positive PC1 and PC2 values as a signature of fast-shock chemistry. Figure 26 presents the l - b and l - v_{LSR} distributions of $\langle N_{H_2} \rangle$, with the regions with positive PC1 and PC2 highlighted in red. In addition to the southeast extension of Sgr B2, some other smaller regions such as Sgr C shell-2, Polar Arc, CO-0.2, M-0.11-0.08, and the clump N2 exhibit this signature of fast-shock regions.

6.3.2. Large Molecules: Regions with Slow Shocks

The coefficient vector diagram has another distinctive group constituted by two relatively large molecules, i.e., HC_3N and p - H_2CO , which are characterized by large x_T , moderate x_1 , and negative x_2 values. These molecules could be classified as species enhanced in hot cores in the sense that their formation paths include dust-grain chemistry. The strong T_{kin} dependence of their abundance may indicate that their origin is thermal desorption from heated dust; however, this hot-core explanation does not conform with the observed decoupling of the gas and dust temperatures. The *dust* temperature is uniformly low (~ 20 K) throughout the CMZ, and it is not correlated with the *gas* temperature (Pierce-Price et al. 2000).

The correlation of their abundances with T_{kin} is better explained by the impacts of low-velocity shocks with velocities $\lesssim 20$ km s $^{-1}$. The gas-phase abundances of large organic molecules can be enhanced by the mechanical sputtering of the icy grain mantle (Requena-Torres et al. 2006; Harada et al. 2015), as observed in molecular outflow sources in SF regions (Jorgensen et al. 2004; Tafalla et al. 2010). In addition, mechanical heating by decaying shocks is considered to be a dominant mechanism of gas heating in the CMZ (e.g., Rodríguez-Fernández et al. 2000; Tanaka et al. 2009; Ao et al. 2013; Ginsburg et al. 2016). The positive correlation between T_{kin} and the HC_3N and H_2CO abundances lends observational support for the theory of hot-core chemistry without hot cores induced by low-velocity shocks (Requena-Torres et al. 2006).

6.3.3. Two Regimes of Shock Chemistry

It is noteworthy that the above-mentioned two categories, which are distinguished by x_T , x_1 , and x_2 , correspond well to two regimes of shock chemistry commonly observed in two well-studied molecular outflow sources, L1448-mm and IRAS 04166+2706 (Tafalla et al. 2010). The SiO and CS abundances increase in the fast-wing regime with velocities $\gtrsim 20$ km s $^{-1}$ where sputtering of the grain core is significant. The slow-wing regime is characterized by high abundances of H_2CO and CH_3OH , which are caused by dust mantle sputtering, while these large molecules decrease in the fast-wind regime. Although HC_3N is ambiguous in the classification by Tafalla et al. (2010), the morphological similarity of its $J=5-4$ line to the low-excitation CH_3OH line in the Mopra 7-mm survey of the CMZ data (Jones et al. 2013) would justify classifying them in the same category, at least in the CMZ.

Thus, the spatial variations in SiO, CS, HC_3N , H_2CO , and T_{kin} in the CMZ could be consistently explained by a single parameter, i.e., the strength of the shock. The correlation of T_{kin} with the slow-wing species is better than that with the fast-wing species; this could be because slow shocks are simply more common than fast shocks. Even though our analysis does not include the CND, our classification partly overlaps with that proposed for the CND by Takekawa et al. (2014); the GMC-type species in the CND include HC_3N and other hot-core-type species, while the CND-type and hybrid-type consist of small molecules including SiO and CS, which may indicate the significance of fast-shock chemistry in the CND (Harada et al. 2015).

Several regions with high T_{kin} values or those with both high T_{kin} and a rich abundance of fast-shock tracers (i.e., high PC1 and PC2 values) exhibit kinematics that are indicative of the interaction with shocks, such as the expanding shells in Sgr B2 and Sgr C (Tsuboi et al. 2015; Tanaka et al. 2014), the extremely broad emissions of CO0.02 and CO-0.30 (Oka et al. 2011; Tanaka et al. 2014, 2015), and the polar arc, which are argued to be a part of the molecular outflow driven by a past activity of SgrA* (Hsieh et al. 2016). On the contrary, the region with high PC1 and PC2 but low T_{kin} , such as GMC complex M0.11-0.08, might require another explanation. Amo-Baladrón et al. (2009) proposed the hypothesis of nonthermal sputtering of small dust grains by hard X-ray photons for SiO enrichment in the region and obtained a spatial correlation between the SiO abundance and the 6.4 keV fluorescent Fe line. Their hypothesis has an advantage over the explanation with shock chemistry, as it is consistent with the absence of the temperature rise in M0.11-0.08 in the results of the HB analysis.

6.3.4. Effect of Cosmic Rays

The intense CR field in the CMZ may induce hot-core-like chemistry through the CR-induced UV photodesorption of grain mantle species (Yusef-Zadeh et al. 2013). In addition, it can be a significant gas-heating mechanism when the CR ionization rate (ζ) is higher than $\sim 10^{-14} \text{ s}^{-1}$ (Ao et al. 2013). Therefore, the same arguments as those used for shock heating and shock chemistry could apply to CR heating and CR-induced chemistry if the primary source of the CR acceleration is SNR–MC interactions.

We may be able to separate the effect of CRs from shocks by investigating the spatial variation in HCO⁺, as $x_{\text{mol}}(\text{HCO}^+)$ is expected to be scaled by $\zeta_{\text{CR}} \cdot n_{\text{H}_2}^{-1}$ (Papadopoulos 2007). The observed strong negative correlation between $x_{\text{mol}}(\text{HCO}^+)$ and n_{H_2} is consistent with this regime, whereas this could be alternatively understood as a decreasing inward gradient due to UV photodissociation. However, further positive evidence for effects of CRs on chemistry and thermal processes is not obtained with our data; $x_{\text{mol}}(\text{HCO}^+)$ exhibits a considerably flat spatial variation except for the n_{H_2} dependence, and no significant correlation with T_{kin} is observed.

6.3.5. HCN and HNC

The HCN $J=1-0$ line is frequently used to estimate the mass of dense gas (typically with $n_{\text{H}_2} \gtrsim 10^4 \text{ cm}^{-3}$), which is supposed to be directly linked to star formation activities (e.g. Lada et al. 2012). Our analysis shows that the spatial variation in the HCN abundance is approximately correlated with that of the conversion factor from the HCN $J=1-0$ luminosity to dense gas mass that is found by Mills & Battersby (2017); the abundance is relatively high for the clouds with over-luminous HCN emission (the 50-km s⁻¹ cloud) compared with the clouds with regions with under-luminous HCN emission (the Sgr B2 cluster-forming region and the 20-km s⁻¹ cloud). This supports the argument in Mills & Battersby (2017) that the large spatial variation in the HCN-to-dense-gas conversion factor is created primarily by the variation in the HCN abundance, though the opacity effect significantly masks the abundance variation. One possible cause of the variation in the HCN abundance is shock chemistry, as this abundance is observed to increase in fast-shock regions in molecular outflow sources (Tafalla et al. 2010; Mills & Battersby 2017); in fact, the position of HCN in the x_T – x_2 vector component diagram (Figure 25c) is close to those of other fast-shock tracers such as SiO and CS.

The [HCN]/[HNC] isomer ratio increases sharply with T_{kin} according to the systematic survey by Hirota et al. (1998), who found that the ratio is ~ 1 for dark clouds with $T_{\text{kin}} \sim 10 \text{ K}$, while it increases to ~ 10 for a high-mass SF region with $T_{\text{kin}} \gtrsim 20 \text{ K}$. The mean [HCN]/[HNC] ratio for the CMZ is 10, which is close to the values for the latter regime; the CMZ is hot-core-like in terms of the [HNC]/[HCN] isomer ratio. T_{kin} dependence of the isomer ratio is absent within our data.

7. SUMMARY

We have presented the maps of HCN $J=4-3$, H¹³CN $J=1-0$, HNC $J=1-0$, and HC₃N $J=10-9$ covering the major part of the CMZ with spatial and velocity resolutions of $\sim 20'' \times 2 \text{ km s}^{-1}$, which we obtained using the ASTE 10-m telescope and NRO 45-m telescope. Spatially resolved measurements of T_{kin} , n_{H_2} , and the fractional abundances of eight molecules have been conducted using our data and survey data taken from the literature by combining the LVG calculation with HB inference. The primary results obtained from the analysis are summarized below.

1. The HCN $J=4-3$ and HC₃N $J=10-9$ maps exhibit similar spatial distributions, whose intense emissions are limited to high-temperature regions, while HCN $J=1-0$ and HNC $J=1-0$ trace the mass distribution of dense gas.
2. The 3-D (2-D in space and 1-D in velocity) distributions of N_{H_2} , T_{kin} , n_{H_2} , the beam filling factor, the [¹²C]/[¹³C] isotopic abundance ratio, and the fractional abundances of HCN, HCO⁺, HNC, HC₃N, p -H₂CO, SiO, N₂H⁺, and CS are calculated by employing the HB analysis. The model includes parameters for systematic errors that represent the unmeasurable uncertainties from calibration errors and deviations from the ideal model, such as the one-zone LVG approximation. A multivariate log-Student prior and log-normal prior are assumed for the primary parameters and errors, respectively.
3. The HB analysis is successful in suppressing strong artificial correlations among the parameters, while these artifacts strongly affect the results of the nonhierarchical method that is equivalent to the standard maximum likelihood analysis. All line intensities are fitted with the HB analysis without assuming large systematic errors.
4. The measured values of n_{H_2} are distributed in the range of $10^{3.4}$ – $10^{4.8} \text{ cm}^{-3}$ with the highest frequency at $10^{4.2} \text{ cm}^{-3}$. These results are consistent with previous measurements conducted using molecular lines with similar critical densities to those used by us. No systematic difference is observed between n_{H_2} for highly active cluster-forming regions (such as Sgr B2 and G–0.02–0.07) and quiescent massive clumps (such as the brick cloud).

5. The typical value of T_{kin} is $\sim 10^{1.8}$ K, which is consistent with the previous LTE analysis performed using the same H_2CO data. The distribution of the high-temperature gas is not correlated with the star-forming regions, except for two high-temperature spots toward the Sgr B2 cluster-forming region and G-0.02-0.07. A few of the high-temperature regions without UV-heating sources are associated with broad-velocity features or clouds with the kinematics of expanding shells, such as CO0.02, CO-0.30, Sgr C shell 2, and Sgr B shell 3.
6. The fractional abundances of SiO, CS, HC_3N , N_2H^+ , and H_2CO exhibit considerable enhancement in the Sgr B2 complex. The HCN, HCO^+ , and HNC abundances show small variations across the CMZ, except for a significant negative correlation of the former with n_{H_2} , making them good probes of the gas mass and physical conditions.
7. The ^{13}CO $J=1-0$ intensity estimated from our analysis explains only $\sim 30\%$ of the observed luminosity; this suggests the presence of a second component with a lower temperature and density, which is not observable in the high-density tracers used in the analysis.
8. The spatial variations in T_{kin} , n_{H_2} , and the fractional abundances of the eight species can be reduced into four primary components, i.e., the covariant components with T_{kin} and n_{H_2} and the first and second principal components (PC1 and PC2) of the remaining variances, whose sum accounts for approximately 93% of the total variance in the parameter space. Two distinct molecular species are identified according to their coefficients for the four components (x_T , x_n , x_1 , and x_2): one category with large x_1 , large x_2 , and moderate-to-large x_T (SiO and CS) and the other with large x_T , smaller x_1 than the first group, and negative x_2 (HC_3N and H_2CO). The former and latter groups approximately correspond to the molecules enhanced in the fast and slow shocks, respectively. This indicates that the strength of the mechanical sputtering of dust grains is one of the primary determinants of molecular chemistry in CMZ clouds. This is corroborated by their positive dependence on T_{kin} .
9. The HCO^+ abundance is anticorrelated with n_{H_2} . This is consistent with CR ionization or photodissociation theories, even though further evidence for the effect of the CRs on gas heating is not obtained. The high $[\text{HCN}]/[\text{HNC}]$ isomer ratio of 10 is close to the value for high-mass SF regions.

The authors are grateful to the staff of the National Astronomical Observatory Japan for their generous support during the observations. We also thank the anonymous referee and Dr. Feigelson, whose comments helped refine the analysis. This work was supported by JSPS KAKENHI Grant Numbers 26800105 and 16K17666. The data cubes and the source code of the analysis software presented in this paper will be available on the NRO website².

REFERENCES

- Amo-Baladr3n, M. a., Mart3n-Pintado, J., Morris, M. R., Muno, M. P., & Rodr3guez-Fern3ndez, N. J. 2009, *ApJ*, 694, 943
- Ao, Y., Henkel, C., Menten, K. M., et al. 2013, *A&A*, 550, A135
- Arai, H., Nagai, M., Fujita, S., et al. 2016, *PASJ*, 68, 2
- Barnard, J., McCulloch, R., & Meng, X.-L. 2000, *Statistica Sinica*, 10, 1281
- Duane, S., Kennedy, A. D., Pendleton, B. J., & Roweth, D. 1987, *Physics Letters B*, 195, 216
- Emerson, D. T., & Gr3ve, R. 1988, *A&A*, 190, 353
- Figer, D. F., Morris, M. R., Geballe, T. R., et al. 1999, *ApJ*, 10, 759
- Ginsburg, A., Henkel, C., Ao, Y., et al. 2016, *A&A*, 50, 1
- Goldreich, P., & Kwan, J. 1974, *ApJ*, 190, 27
- Harada, N., Riquelme, D., Viti, S., et al. 2015, *arXiv*, 1
- Hirota, T., Yamamoto, S., Mikami, H., & Ohishi, M. 1998, *ApJ*, 503, 717
- Hsieh, P.-Y., Ho, P. T. P., Hwang, C.-Y., et al. 2016, *ApJ*, 831, 38
- Huttemeister, S., Wilson, T. L., Bania, T. M., & Mart3n-Pintado, J. 1993, *A&A*, 280, 255
- Jones, P. A., Burton, M. G., Cunningham, M. R., Tohill, N. F. H., & Walsh, A. J. 2013, *MNRAS*, 433, 221
- Jones, P. A., Burton, M. G., Cunningham, M. R., et al. 2012, *MNRAS*, 419, 2961
- Jorgensen, J. K., Hogerheijde, M. R., van Dishoeck, E. F., Blake, G. A., & Schoier, F. L. 2004, *A&A*, 413, 993
- Kamenetzky, J., Glenn, J., Rangwala, N., et al. 2012, *ApJ*, 753, 70
- Kelly, B. C., Shetty, R., Stutz, A. M., et al. 2012, *ApJ*, 752, 55
- Kruijssen, J. M. D., Longmore, S. N., Elmegreen, B. G., et al. 2014, *MNRAS*, 440, 3370

² <http://www.nro.nao.ac.jp/~nro45mrt/html/results/data.html>

- Lada, C. J., Forbrich, J., Lombardi, M., & Alves, J. F. 2012, *ApJ*, 745, 190
- Ladd, N., Purcell, C., Wong, T., & Robertson, S. 2005, *Publications of the Astronomical Society of Australia*, 22, 62
- Lis, D. C., & Goldsmith, P. F. 1989, *ApJ*, 337, 704
- . 1990, *ApJ*, 356, 195
- Longmore, S. N., Bally, J., Testi, L., et al. 2012, *MNRAS*, 429, 987
- Mangum, J. G., & Wootten, A. 1993, *ApJS*, 89, 123
- Martin, C. L., Walsh, W. M., Xiao, K., et al. 2004, *ApJS*, 150, 239
- Martín-Pintado, J., de Vicente, P., Fuente, A., & Planesas, P. 1997, *ApJL*, 482, L45
- Mills, E. A. C., & Battersby, C. 2017, *ApJ*, 835, 76
- Molinari, S., Bally, J., Noriega-Crespo, a., et al. 2011, *ApJ*, 735, L33
- Morris, M. R., & Serabyn, E. 1996, *ARA&A*, 34, 645
- Nagai, M., Tanaka, K., Kamegai, K., & Oka, T. 2007, *PASJ*, 59, 25
- Nagata, T., Woodward, Charles, E., Shure, M., & Kobayashi, N. 1995, *AJ*, 109, 1676
- Nagayama, T., Omodaka, T., Handa, T., et al. 2007, *PASJ*, 59, 869
- Nordlund, Å., & Padoan, P. 1999, *Interstellar Turbulence*, 218
- Oka, T., Nagai, M., Kamegai, K., & Tanaka, K. 2011, *ApJ*, 732, 120
- Oka, T., Nagai, M., Kamegai, K., Tanaka, K., & Kuboi, N. 2007, *PASJ*, 59, 15
- Oka, T., Onodera, Y., Nagai, M., et al. 2012, *ApJS*, 201, 14
- Oka, T., White, G. J., Hasegawa, T., et al. 1999, *ApJ*, 515, 249
- Ott, J., Weiß, A., Staveley-Smith, L., Henkel, C., & Meier, D. S. 2014, *ApJ*, 785, 55
- Papadopoulos, P. P. 2007, *ApJ*, 656, 792
- Pierce-Price, D., Richer, J. S., Greaves, J. S., et al. 2000, *ApJL*, 545, L121
- Pineda, J. L., Goldsmith, P. F., Chapman, N., et al. 2010, *ApJ*, 721, 686
- Rathborne, J., Longmore, S. N., Jackson, J. M., et al. 2014, *ApJ*, 786, 140
- Requena-Torres, M. A., Martín-Pintado, J., Rodríguez-Franco, N. J., et al. 2006, *A&A*, 455, 971
- Riquelme, D., Amo-Baladrón, M. a., Martín-Pintado, J., et al. 2013, *A&A*, 549, 36
- Rodríguez-Fernández, N. J., Martín-Pintado, J., Fuente, A., & T. L., et. a. 2000, *A&A*, 427, 217
- Roueff, E., Loison, J. C., & Hickson, K. M. 2015, *A&A*, 576, 18
- Sawada, T., Ikeda, N., Sunada, K., et al. 2008, *PASJ*, 60, 445
- Schöier, F. L., Tak, F. F. S. V. D., Dishoeck, E. F. V., & Black, J. H. 2005, *A&A*, 432, 369
- Shirley, Y. L. 2015, *Publications of the Astronomical Society of the Pacific*, 127, 299
- Sunada, K., Yamaguchi, C., Nakai, N., et al. 2000, *Proc. SPIE*, 4015, 237
- Tafalla, M., Santiago-Garcia, J., Hacar, A., & Bachiller, R. 2010, *A&A*, 522, A91
- Takekawa, S., Oka, T., Tanaka, K., et al. 2014, *ApJS*, 214, 2
- Tanaka, K., Nagai, M., Kamegai, K., & Oka, T. 2015, *ApJ*, 806, 130
- Tanaka, K., Oka, T., Matsumura, S., Nagai, M., & Kamegai, K. 2011, *ApJL*, 743, L39
- . 2014, *ApJ*, 783, 62
- Tanaka, K., Oka, T., Nagai, M., & Kamegai, K. 2009, *PASJ*, 61, 461
- Tsuboi, M., Handa, T., & Ukita, N. 1999, *ApJS*, 120, 1
- Tsuboi, M., Miyazaki, A., & Uehara, K. 2015, *PASJ*, 67, 1
- Tsuboi, M., & Tadaki, K.-i. 2011, *PASJ*, 63, 763
- Wang, Y.-S., Jaffe, D. T., Graf, U. U., & Evans II, N. J. 1994, *ApJ*, 95, 503
- Yusef-Zadeh, F., Cotton, W., Viti, S., Wardle, M., & Royster, M. 2013, *ApJL*, 764, L19

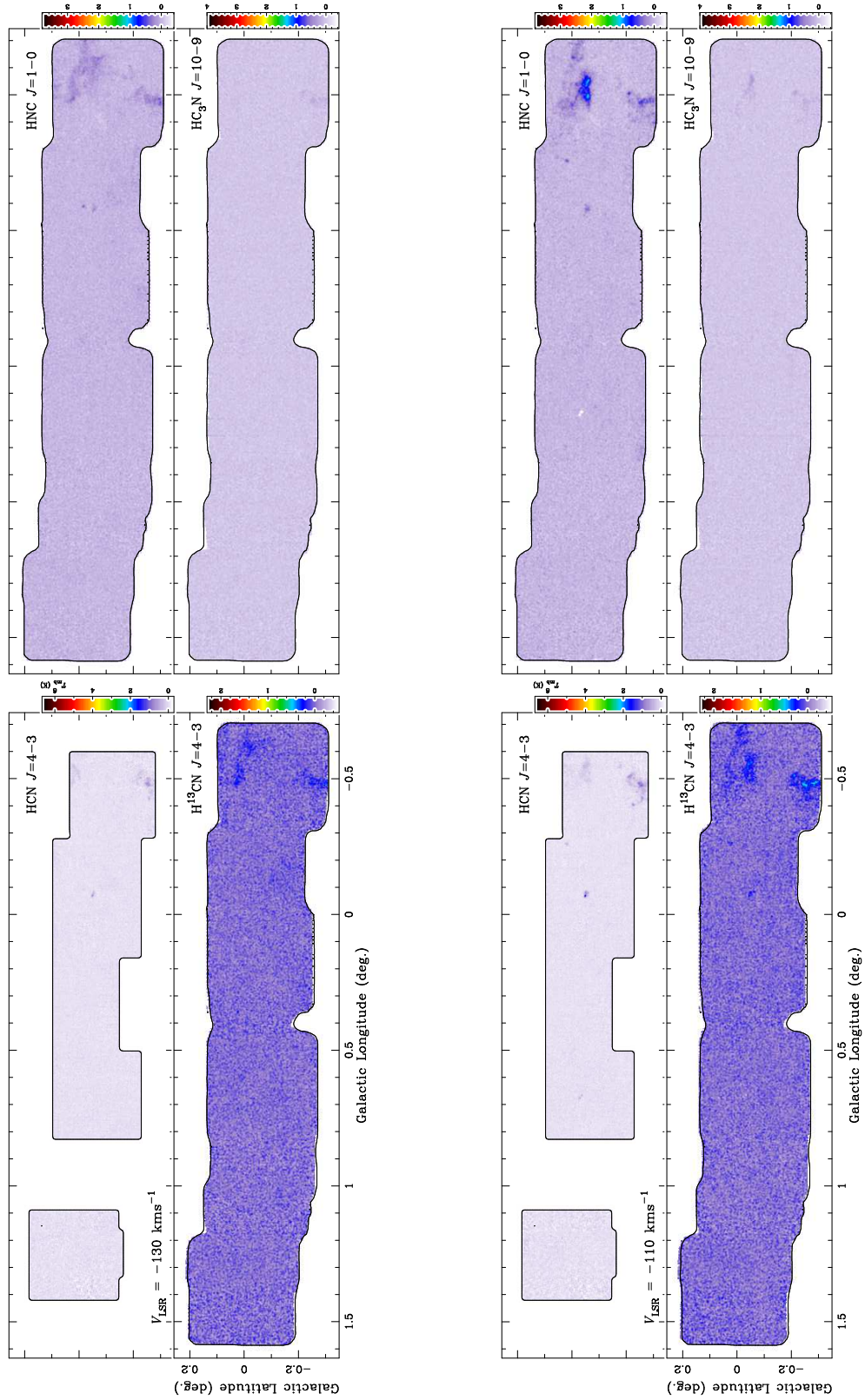
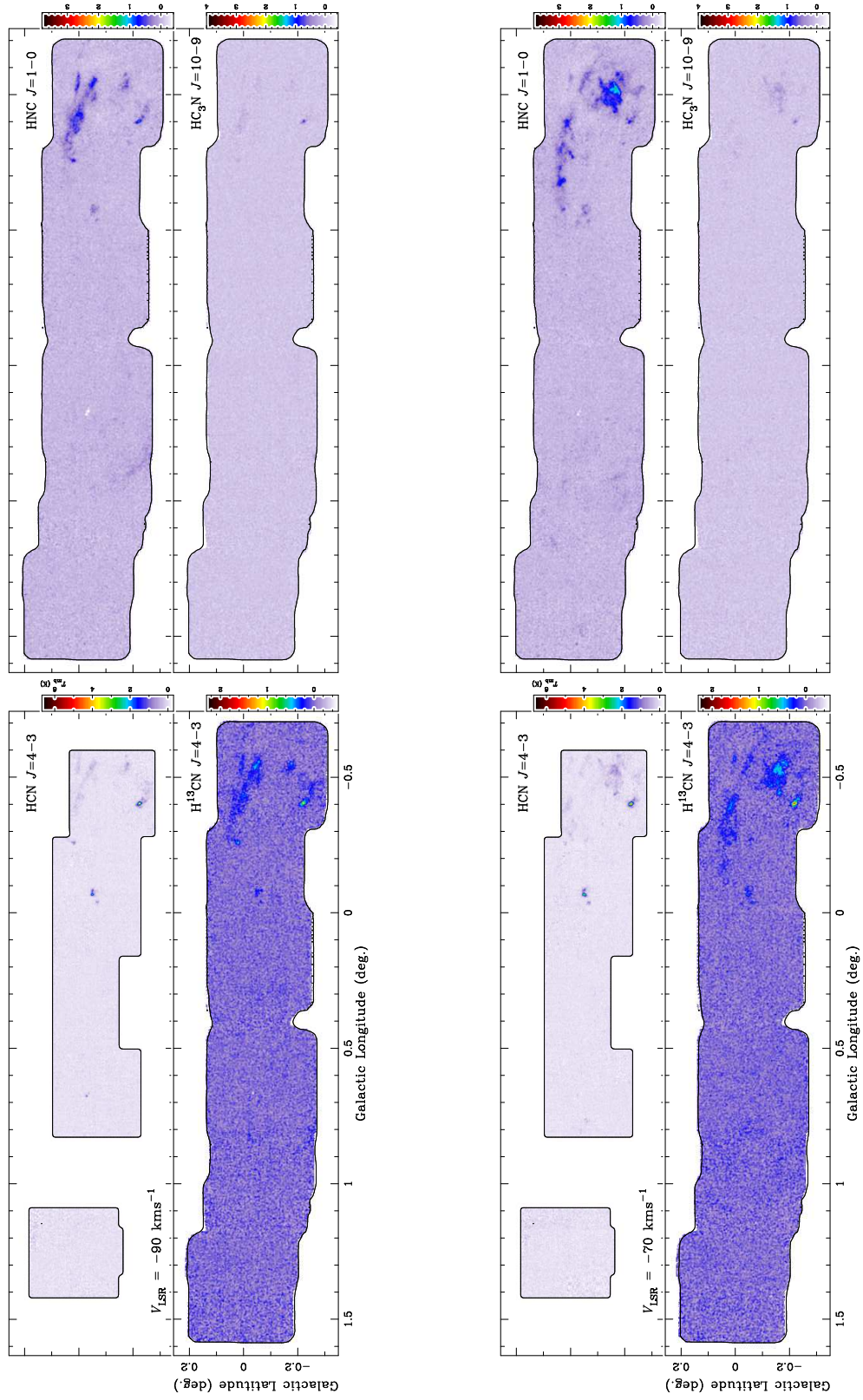


Figure 5. Velocity channel maps of HCN $J=4-3$ (top left), HNC $J=1-0$ (top right), H^{13}CN $J=1-0$ (bottom left), and HC_3N $J=10-9$ (bottom right) for a v_{LSR} range of -190 km s^{-1} to $+190 \text{ km s}^{-1}$ at an interval of 20 km s^{-1} . The channel center velocity is given on the HCN $J=4-3$ panel for each channel.

HCN $J=4-3$, HNC $J=1-0$, H¹³CN $J=1-0$, AND HC₃N $J=10-9$ MAPS OF THE GALACTIC CENTER REGION I37



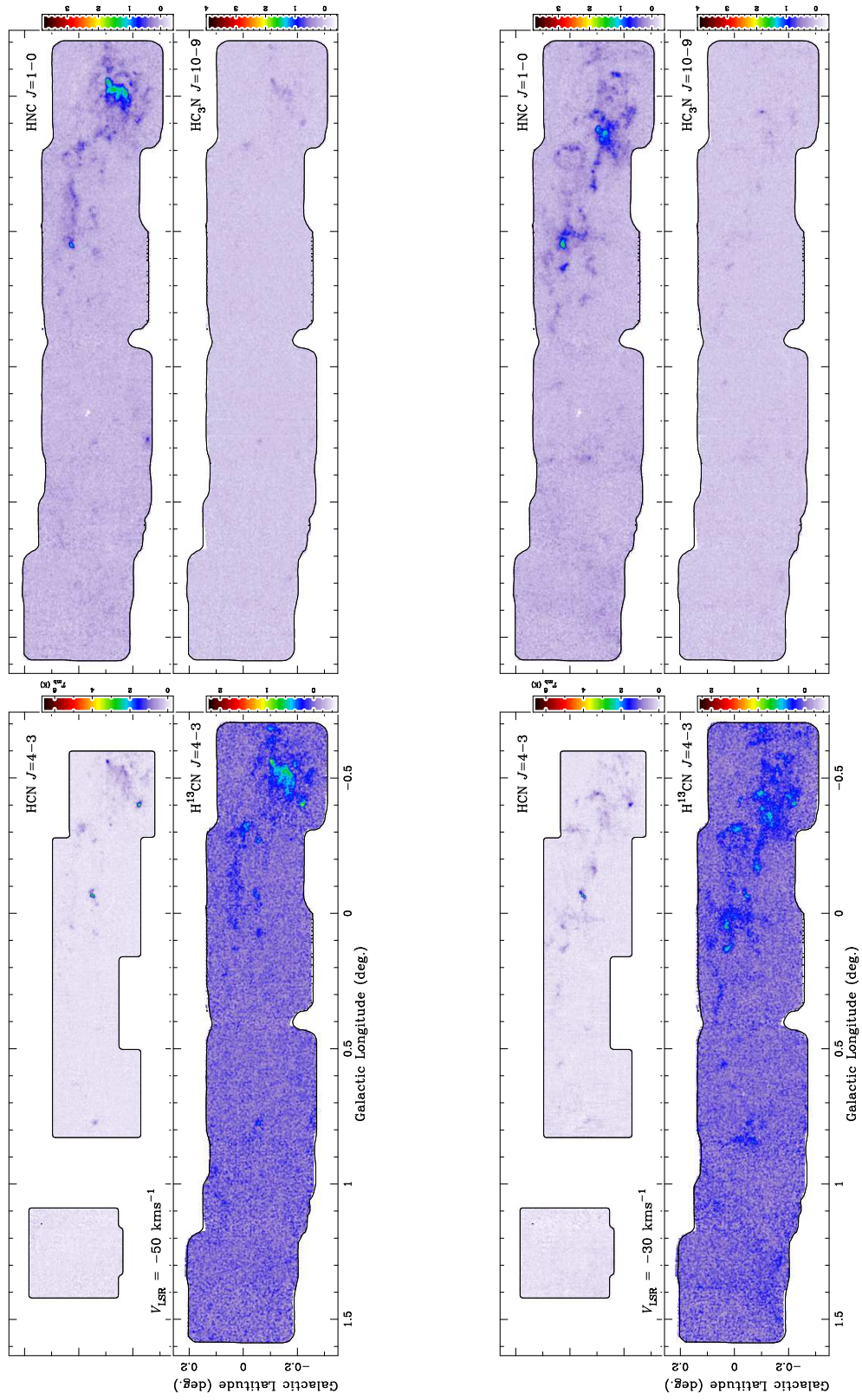


Figure 5 (Continued).

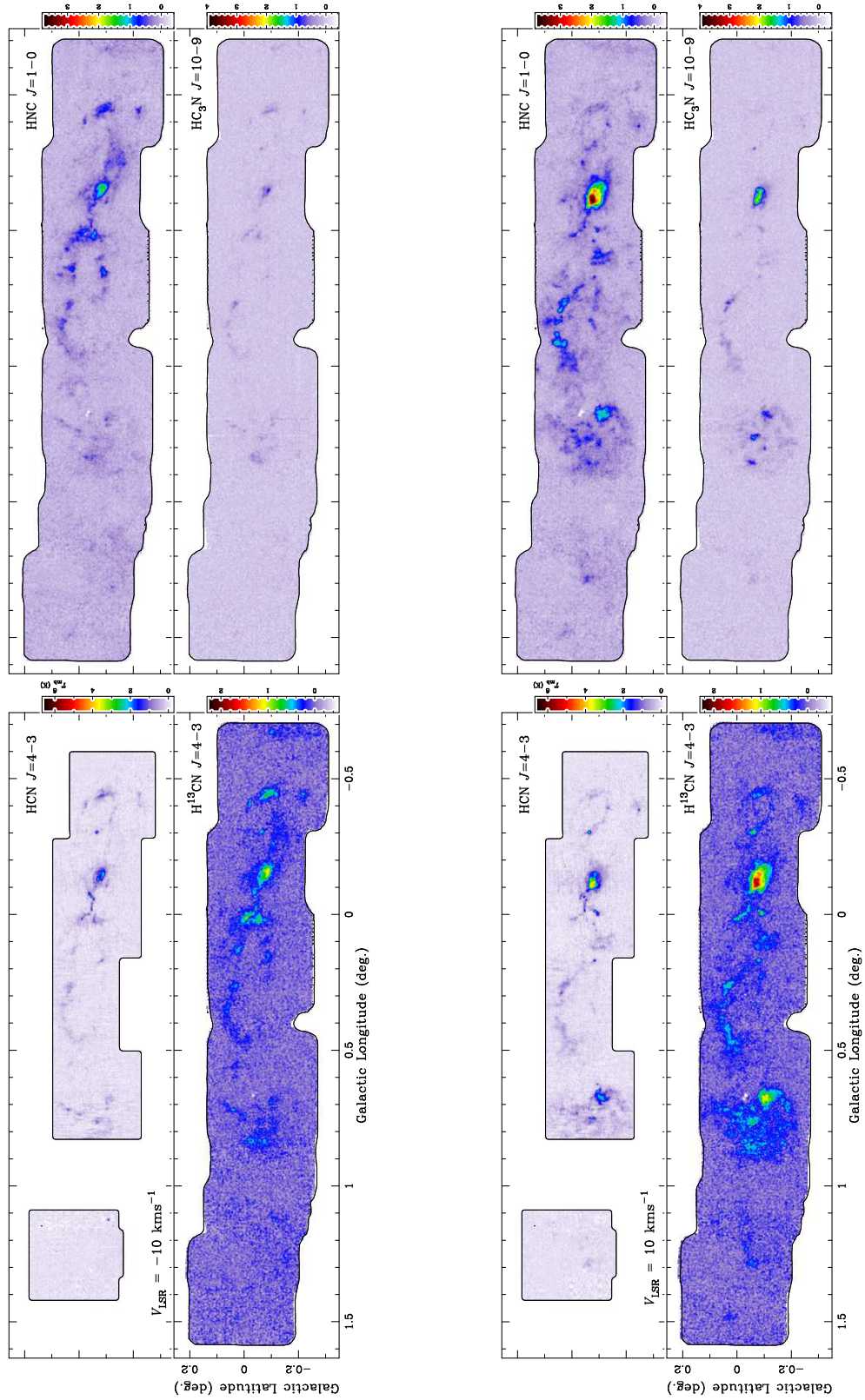


Figure 5 (Continued).

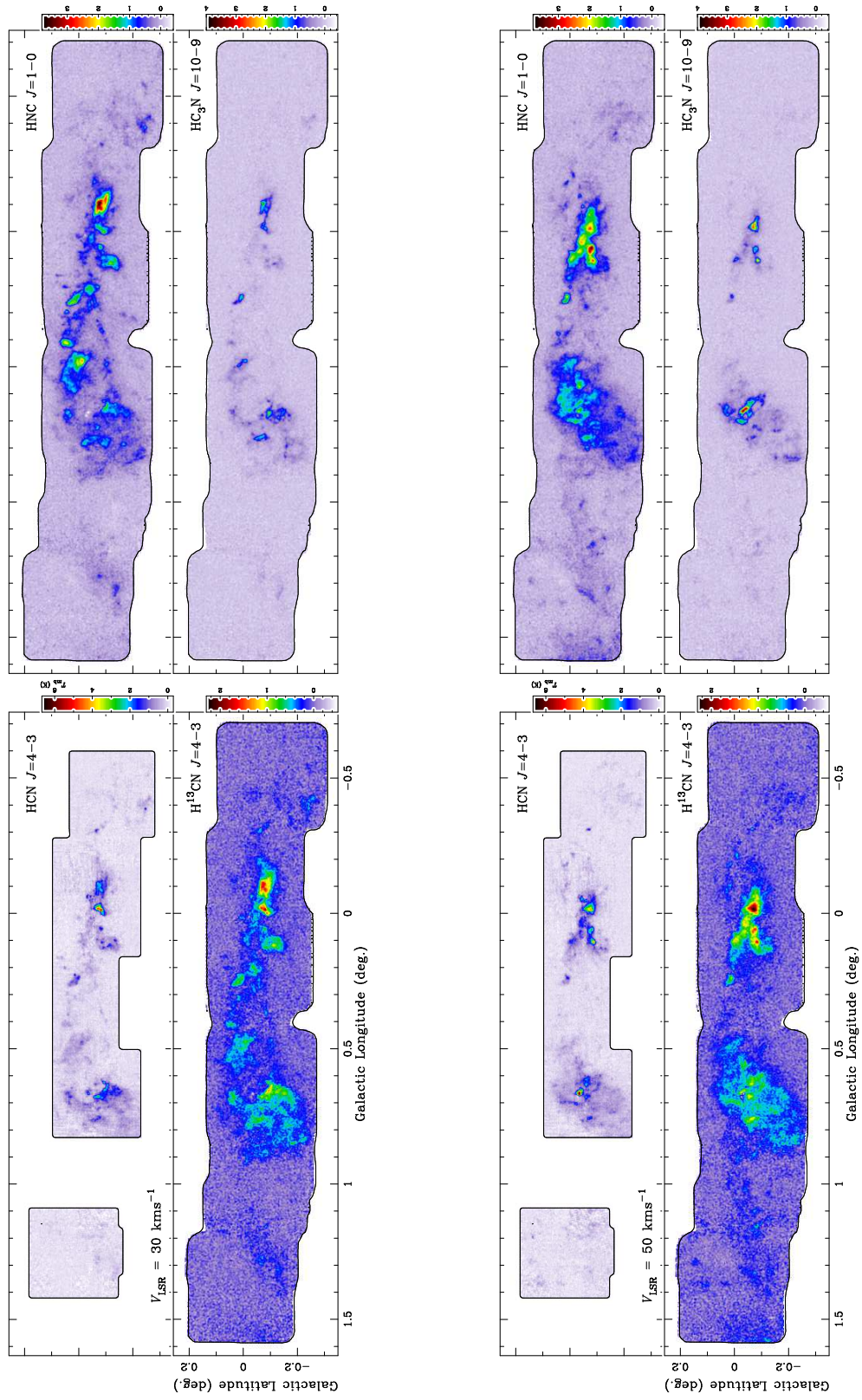


Figure 5 (Continued).

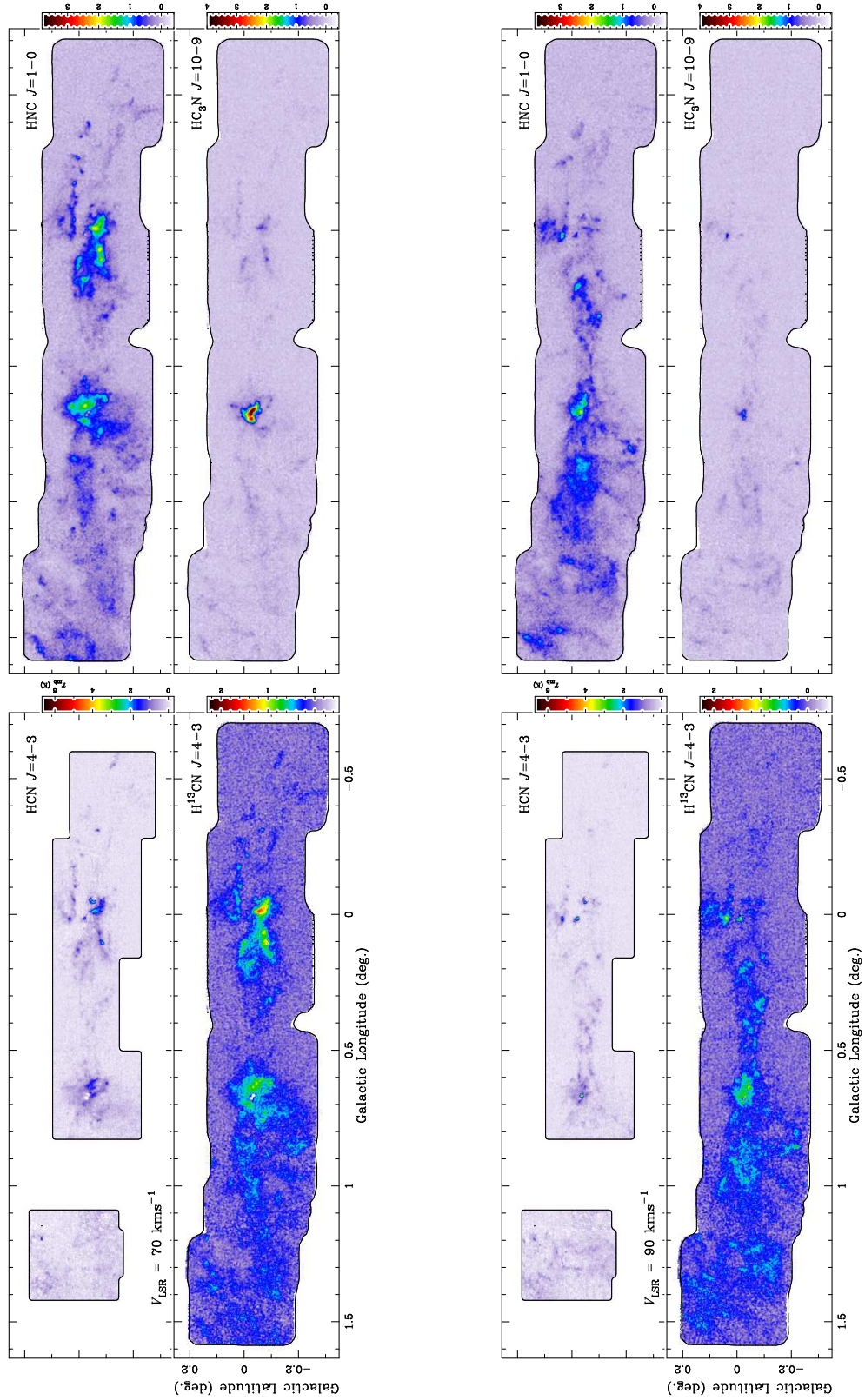


Figure 5 (Continued).

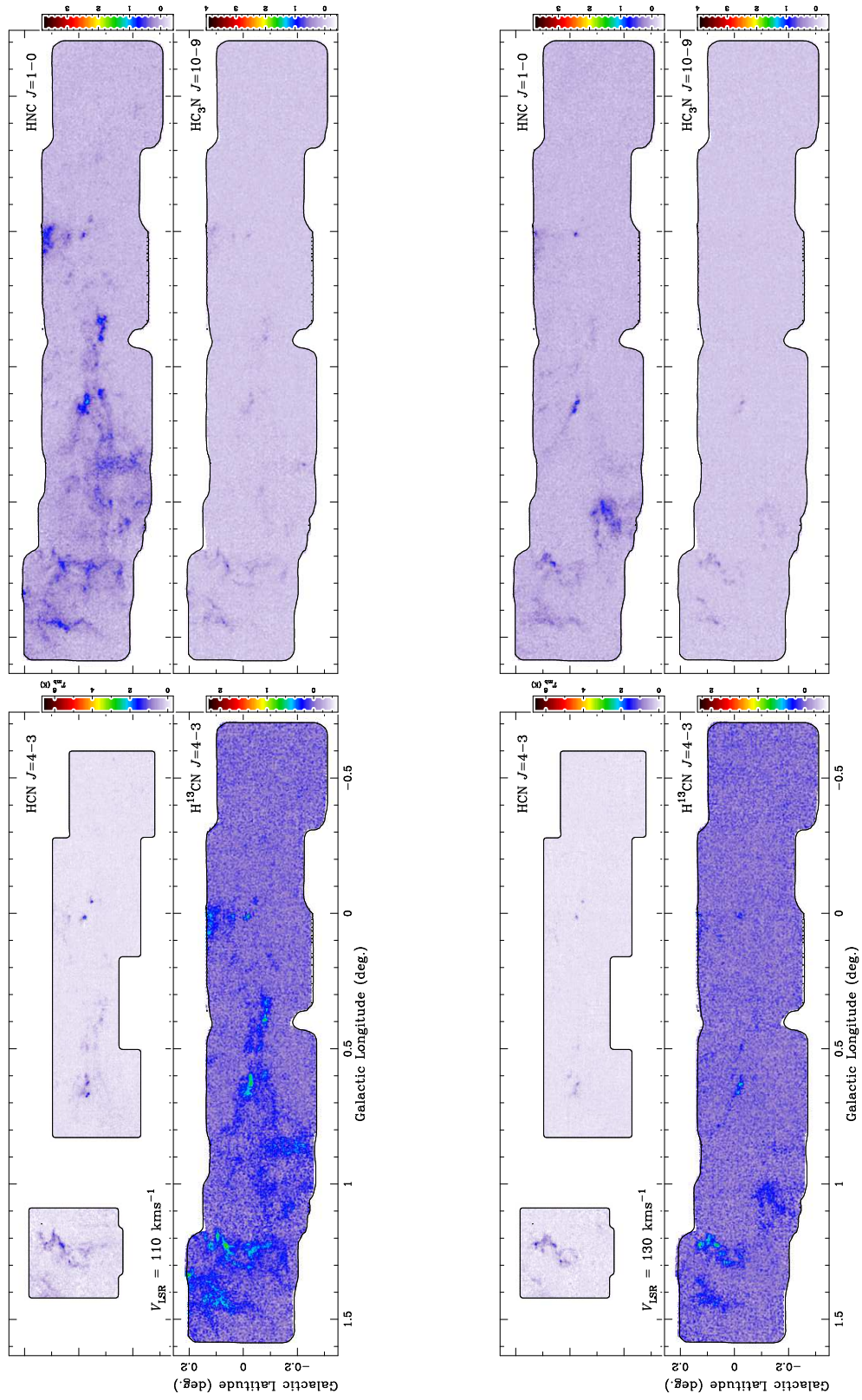


Figure 5 (Continued).

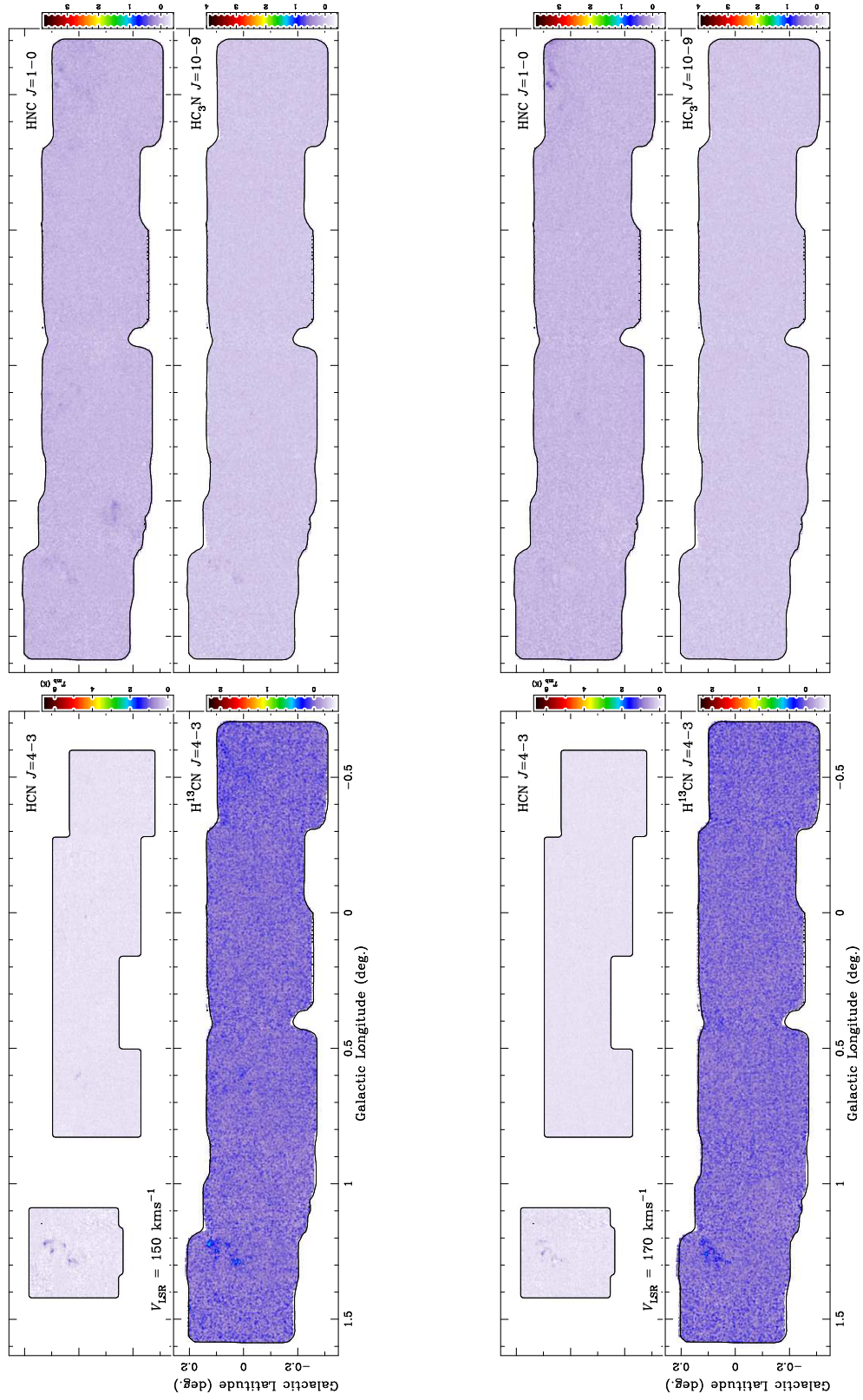


Figure 5 (Continued).

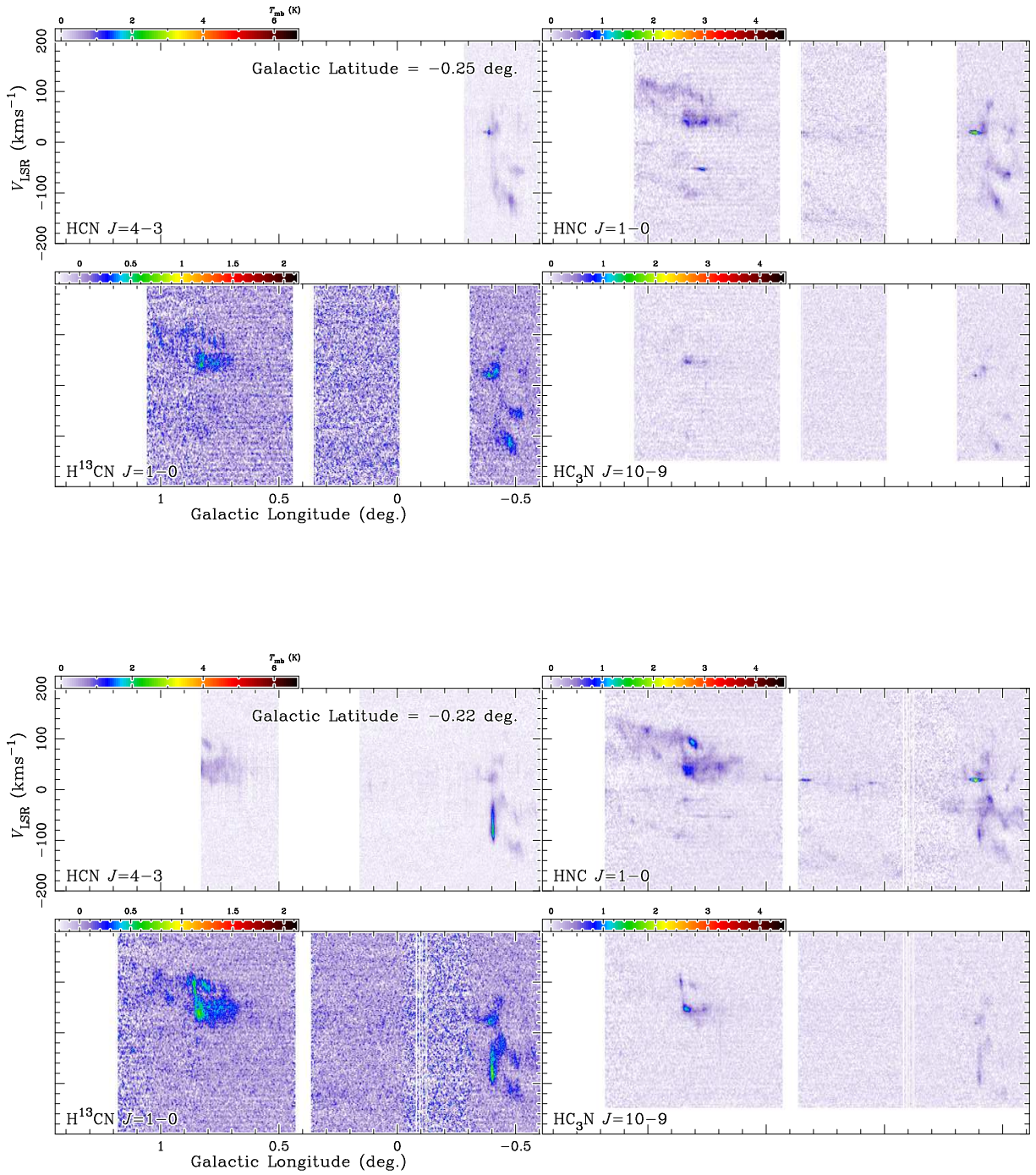


Figure 6. Galactic longitude- v_{LSR} maps of HCN $J=4-3$ (top left), HNC $J=1-0$ (top right), $\text{H}^{13}\text{CN } J=1-0$ (bottom left), and $\text{HC}_3\text{N } J=10-9$ (bottom right) for a latitude range of $-0^\circ.25$ to $+0^\circ.12$ at an interval of $90''$. The channel center latitude is given on the HCN $J=4-3$ panel for each latitude channel.

HCN $J=4-3$, HNC $J=1-0$, $H^{13}CN$ $J=1-0$, AND HC_3N $J=10-9$ MAPS OF THE GALACTIC CENTER REGION I45

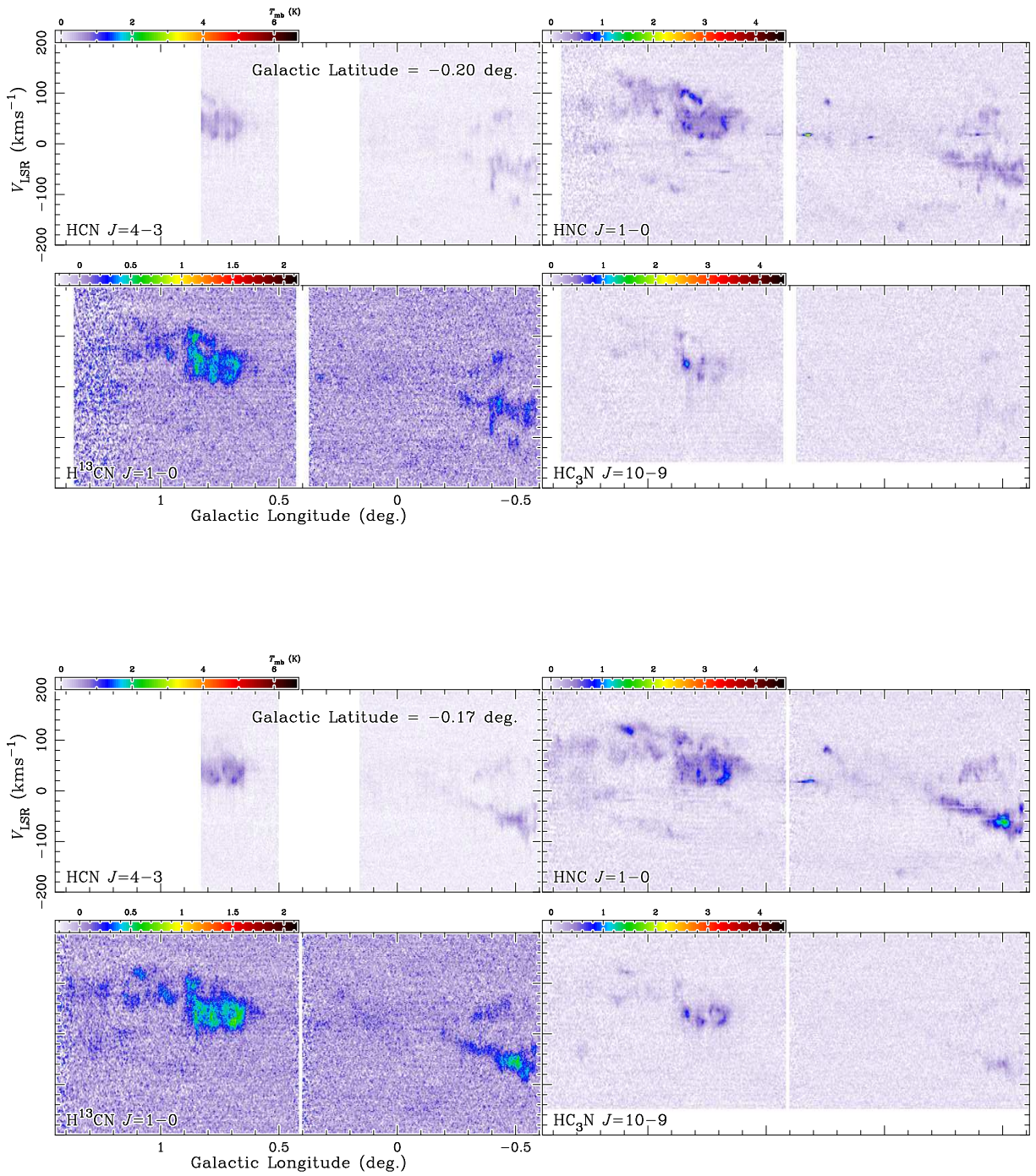


Figure 6 (Continued).

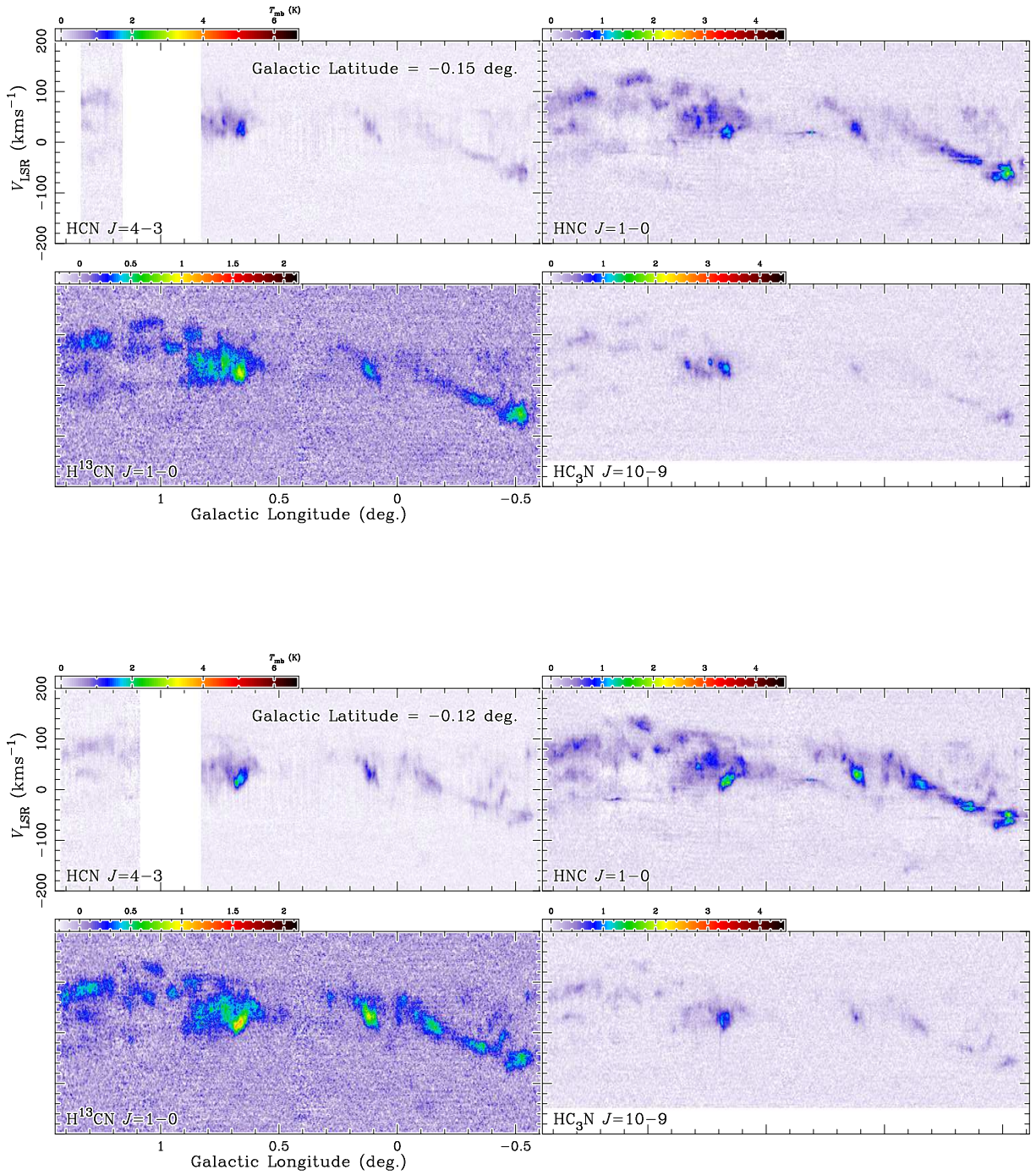


Figure 6 (Continued).

HCN $J=4-3$, HNC $J=1-0$, $H^{13}CN$ $J=1-0$, AND HC_3N $J=10-9$ MAPS OF THE GALACTIC CENTER REGION I47

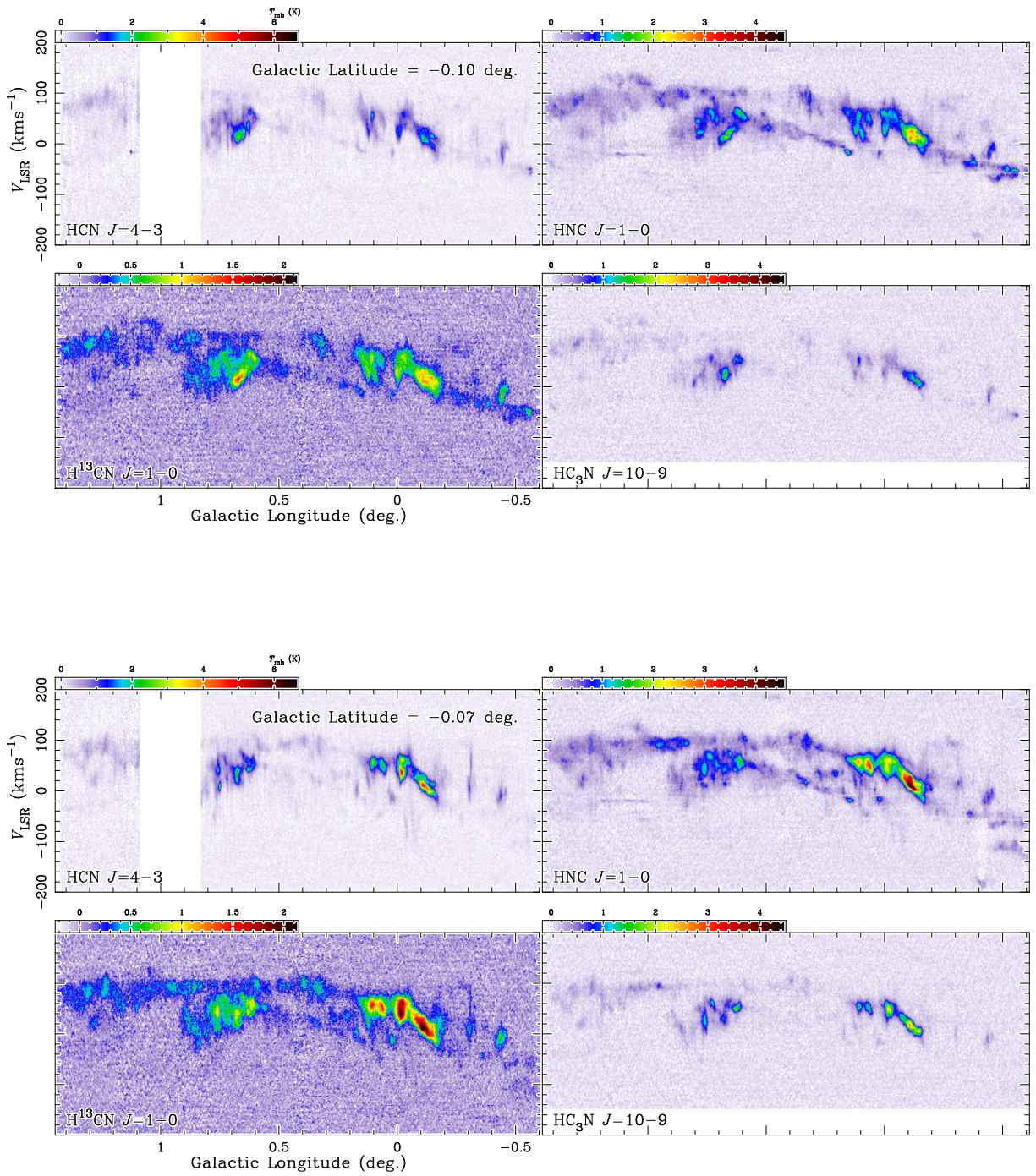


Figure 6 (Continued).

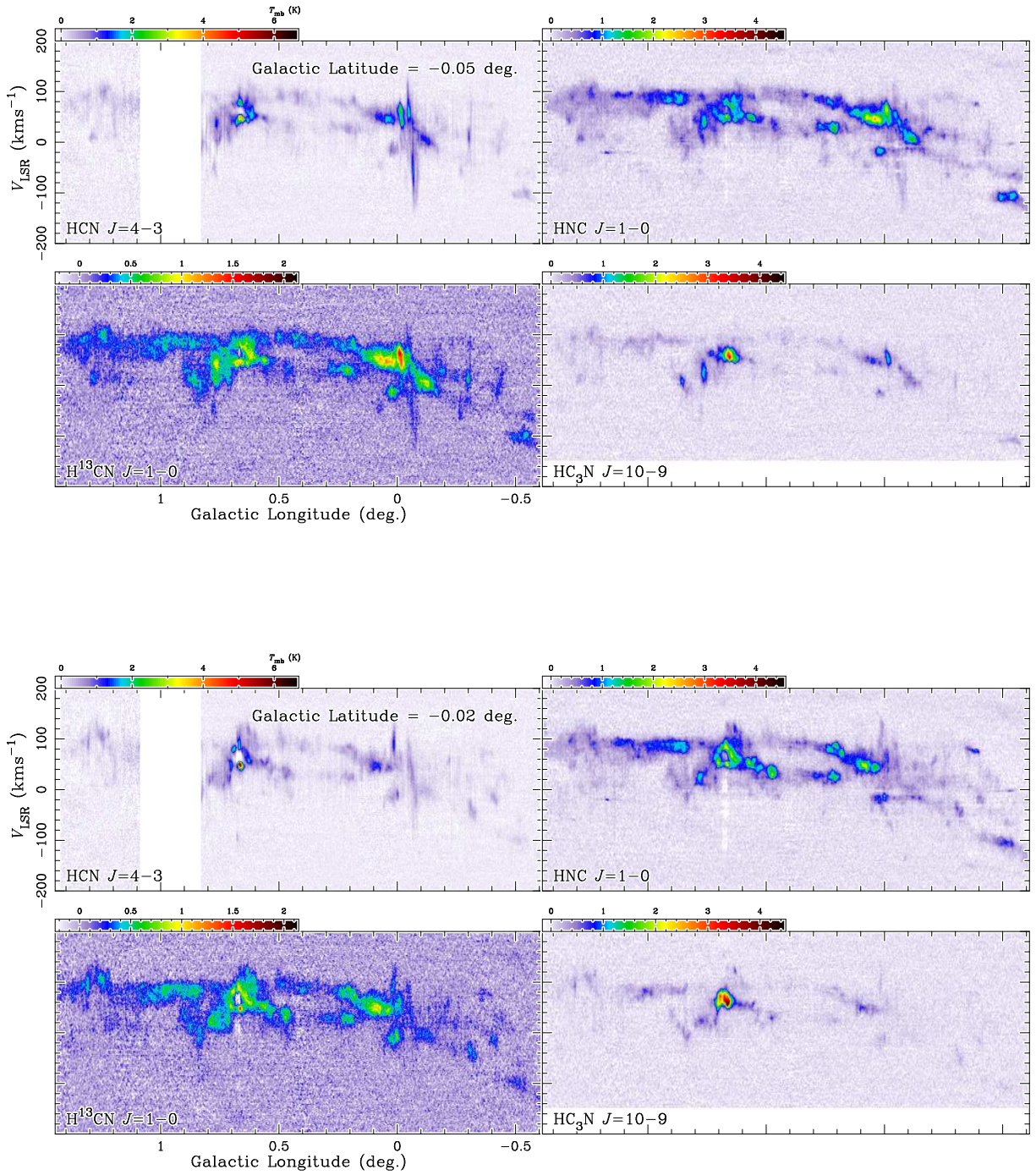


Figure 6 (Continued).

HCN $J=4-3$, HNC $J=1-0$, $H^{13}CN$ $J=1-0$, AND HC_3N $J=10-9$ MAPS OF THE GALACTIC CENTER REGION I49

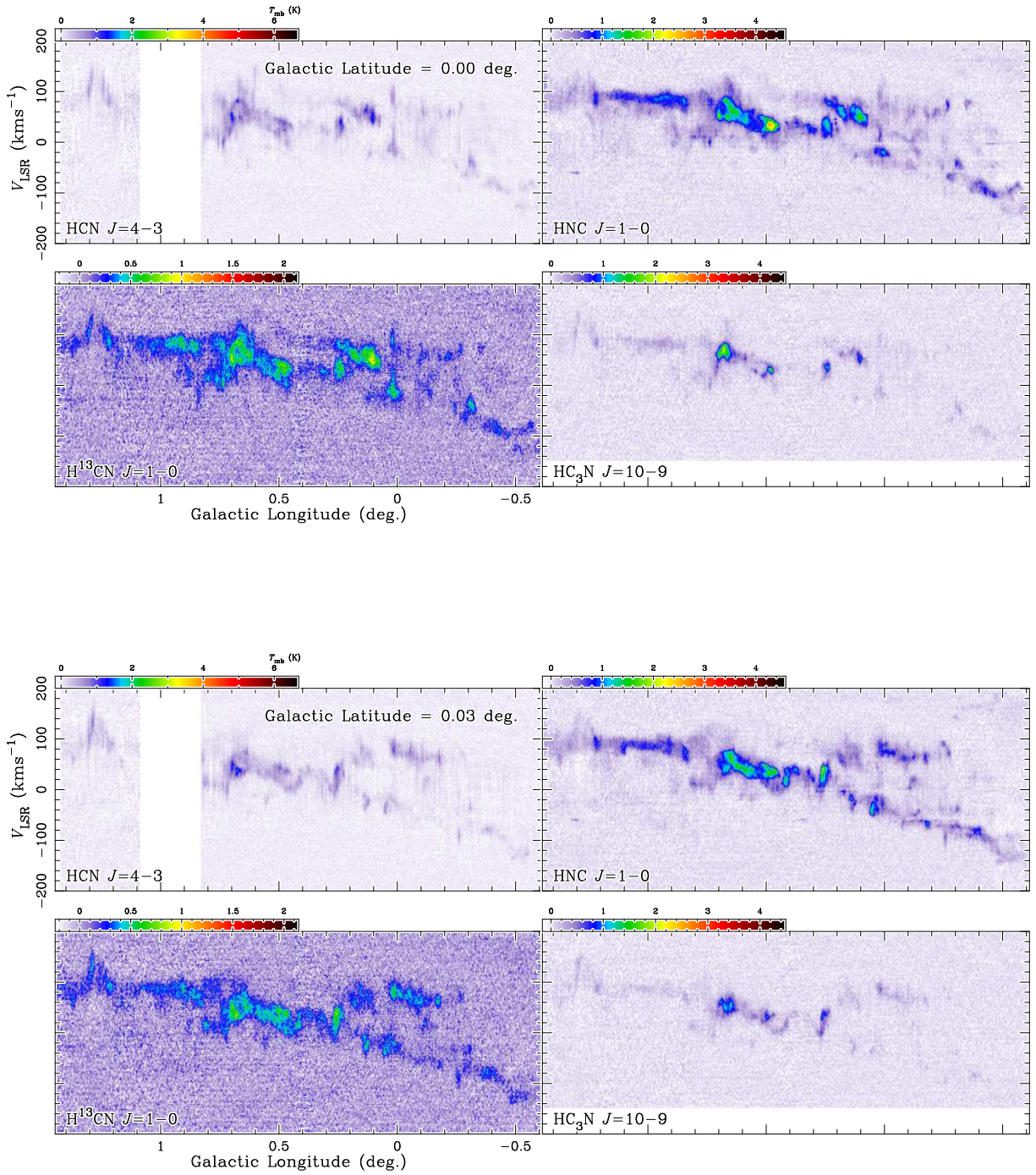


Figure 6 (Continued).

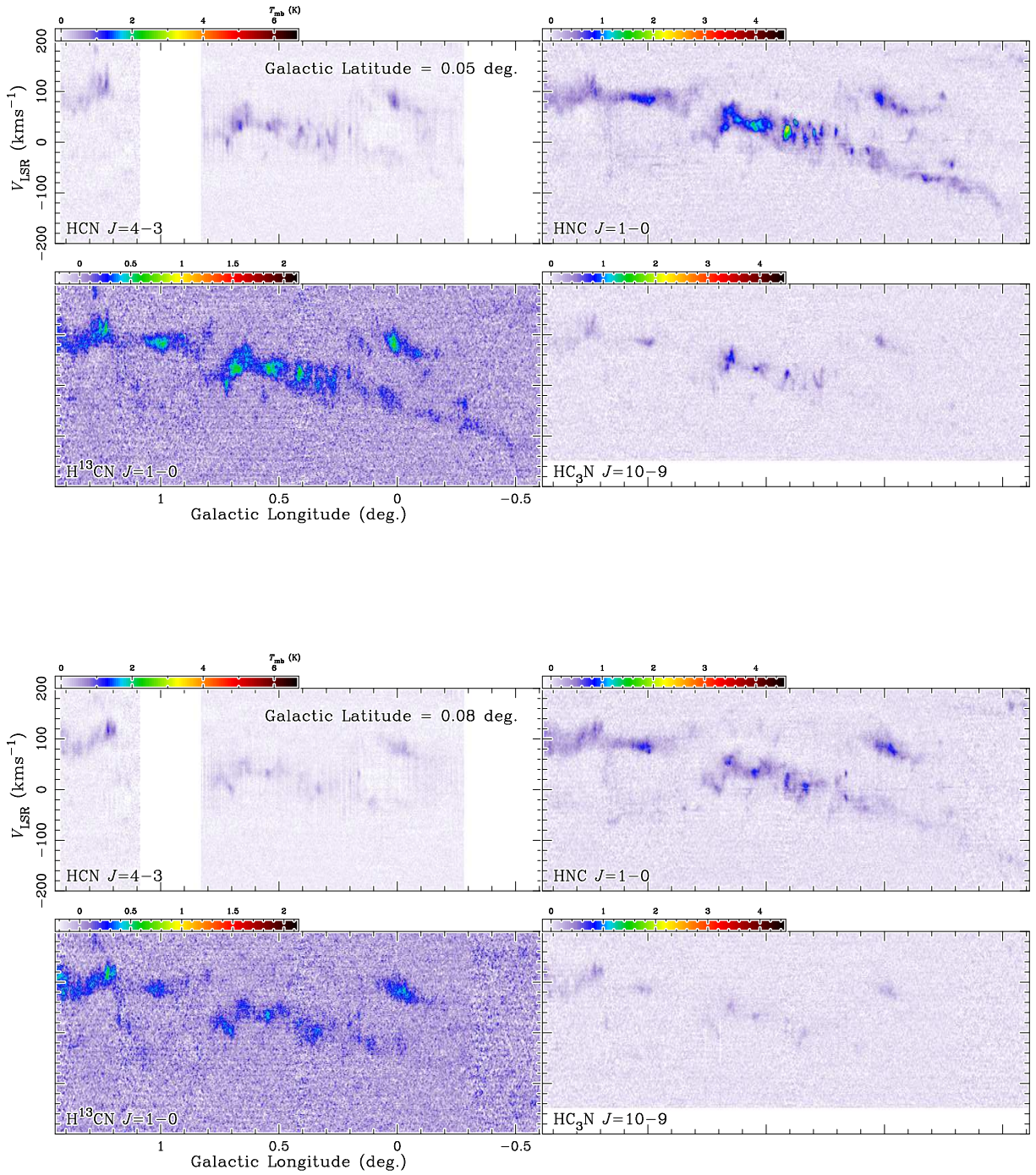


Figure 6 (Continued).

HCN $J=4-3$, HNC $J=1-0$, $H^{13}CN$ $J=1-0$, AND HC_3N $J=10-9$ MAPS OF THE GALACTIC CENTER REGION I51

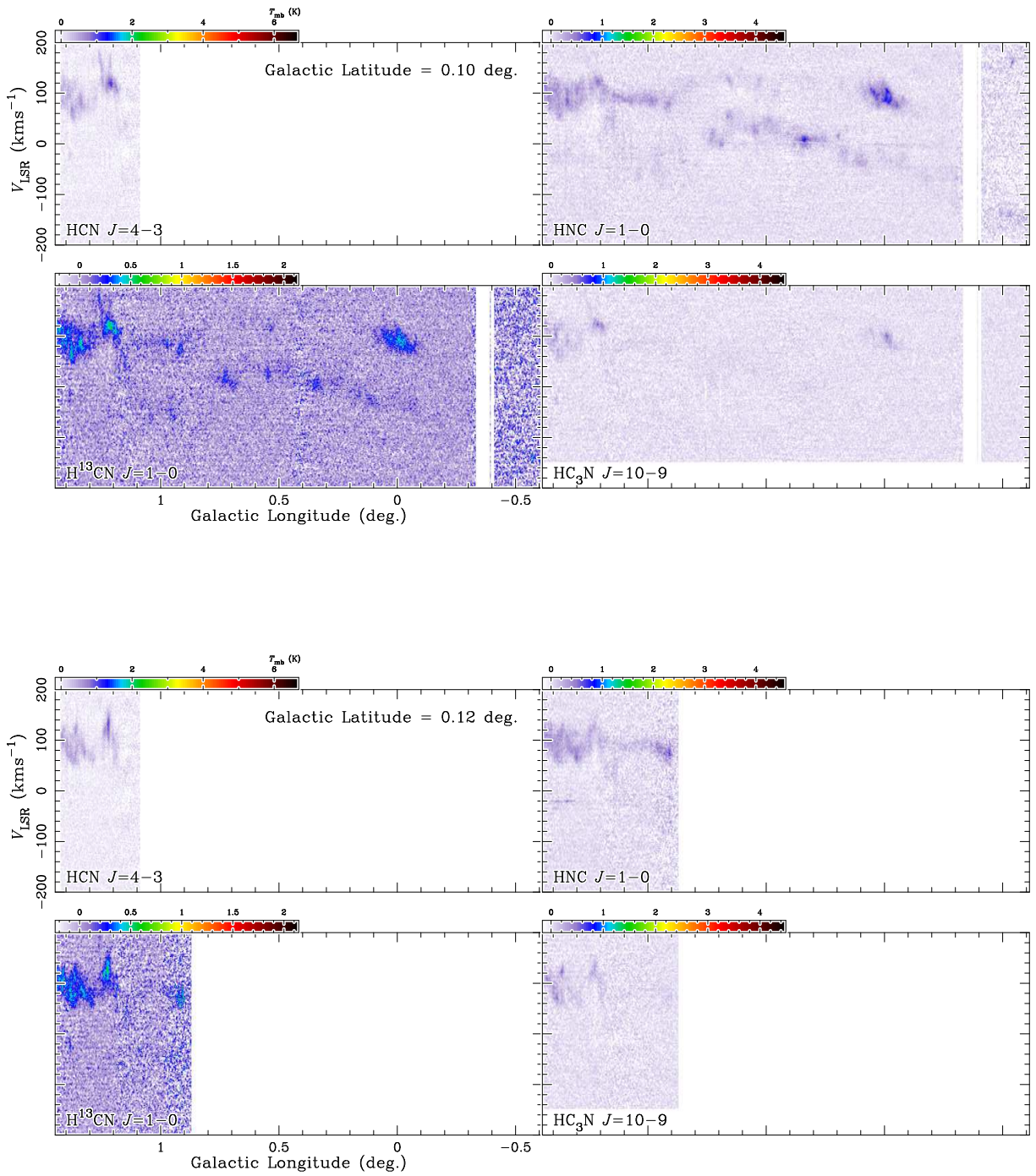


Figure 6 (Continued).